Soil Structure Interaction of Integral Abutment Bridges

by

Ahmed Abdullah

Submitted in partial fulfilment of the requirements
for the degree of Master of Applied Science

at

Dalhousie University
Halifax, Nova Scotia
March 2022

TABLE OF CONTENTS

LIST OF TABLES

LIST OF FIGURES

ABSTRACT

Integral abutment bridges (IABs) are monolithically rigid structures distinguished by eliminating the use of expansion and bearing joints. This leads to enhanced structural performance and reduced maintenance costs. However, the complex soil-structure interactions (SSI) of IABs in response to seasonal variations in ambient temperatures are not yet fully understood. This research aims to use comprehensive numerical models to expand the understanding related to the intricate SSIs of these structures in response to various conditions. The Middlesex bridge in Vermont, USA, was selected as a case study for this research. The thermal response of the bridge was monitored over a period of two years, in which the acting pressures, internal forces, and deformations were measured. The numerical research conducted in this study first involved the development of two- and three-dimensional finite element (FE) models using the software PLAXIS, where the corresponding findings were verified against field acquired measurements for a single case-study bridge. Parametric studies were then conducted to investigate the effects of varying the constitutive soil model, thermal loading, backfill stiffness, abutment stiffness, pile size and orientation, and span length on the resultant earth pressure distributions and pile bending moments. It was found that using a linear constitutive soil model resulted in significant inaccuracies in the results. It was also found that theoretically approximated abutment displacements obtained using the measured temperatures yielded similar results to the field measured deformations. They hence can be used for future performance predictions for climate change studies. The study also revealed that increasing the backfill stiffness was found to increase backfill stresses and decrease pile bending moments. It also showed that varying the abutment stiffness had no impact on the earth pressures and pile bending moments. Smaller pile sections oriented for weak-axis bending yielded smaller pile bending moments and larger earth pressures. Increasing the span length increased backfill stresses and pile bending moments.

Keywords: Integral abutment bridge, thermal loading, piles, earth pressure, pile moment, soil-structure interaction, hardening soil model, Finite element modelling

LIST OF ABBREVIATIONS AND SYMBOLS USED

Abbreviations

AASHTO	*American Association of State Highway and Transportation Officials*
CFT	*Concrete Filled Tube*
CHBDC	*Canadian Highway Bridge Design Code*
CLSM	*Controlled Low Strength Material*
CPT	*Cone Penetration Test*
CSA	*Canadian Standards Association*
DOT	*Department of Transportation*
FE	*Finite Element*
HSM	*Hardening Soil Model*
HST	*Hollow Steel Tube*
IAB	*Integral Abutment Bridge*
LRFD	*Load and Resistance Factor Design*
MC	*Mohr-Coulomb*
MTO	*Ministry of Ontario of Transportation*
OW	*Orange - Wendell*
PC	*Pressure Cell*
PCP	*Prestressed Concrete Pile*
RC	*Reinforced Concrete*
SPT	*Standard Penetration Test*
SSI	*Soil-Structure Interaction*
UK	*United Kingdom*
UPRR	*Union Pacific RailRoad*
USA	*United States of America*
US	*United States*
VL	*Vertical Load*
VTrans	*Vermont Agency of Transportation*
VW	*Vibrating Wire*

Symbols

A_b	*Cross-sectional area of RC deck*
A_c	*Cross-sectional area*
B	*Width of pile group*
b_f	*Pile flange width*
C_c	*Compression index*
C_i	*Inelastic rotation capacity reduction factor*
C_m	*Moment gradient factor*
C_r	*Recompression index*
c'	*Cohesion*
$D^{'}$	*2/3 of pile embedment length*
D_1	*First constant for fixed or pinned pile head conditions*
D_2	*Second constant for fixed or pinned pile head conditions*
D_3	*Third constant for fixed or pinned pile head conditions*
d	*Middlesex bridge deck thickness*
E	*Elastic modulus*
E_b	*Elastic modulus of RC deck*
E_c	*Elastic modulus of concrete*
E_{50}^{ref}	*Secant stiffness in standard drained triaxial test*
E_{oed}^{ref}	*Tangent stiffness for primary oedometer*
E_{ur}^{ref}	*Unloading/reloading stiffness*
E_i	*Initial Modulus of Elasticity of concrete*
e_o	*Initial void ratio*
EA	*Axial rigidity*
EI	*Bending rigidity*
F_a	*Allowable axial stress*
F_b	*Allowable bending stress*
F_e	*Elastic buckling stress*
FS	*Factor of safety*
F_y	*Yield strength of the pile*

f-z	*Axial skin stress – strain relationship*
f_a	*Total applied axial stress on the pile*
f_b	*Total applied bending stress on the pile*
f_c	*Induced compressive stress due to pavement growth*
H	*Depth of calculated pressure below the approach slab*
H_o	*Initial height of soil layer*
I	*Moment of inertia of the pile*
I_c	*Moment of inertia of cross-section*
I_f	*Group embedment influence factor*
I_1	*Strong-axis moment of inertia*
I_2	*Weak axis moment of inertia*
K_o	*At-rest earth pressure coefficient*
k_e	*Equivalent soil stiffness*
k_h	*Horizontal stiffness parameter of the subgrade soil*
L	*Length of bridge*
L_{eM}	*Equivalent cantilever length for bending*
L_s	*Length of pavement section between two construction joints*
L'	*Total length of equivalent beam-column*
l	*Pile length embedded in the subgrade soil*
l_c	*Nondimensionlized length*
l_e	*Equivalent pile length*
l_o	*Active length of pile in bending*
l_u	*Length of pile head above ground level*
M	*Flexural deformation*
M_r	*Total positive moment*
M_s	*Induced second order moment*
M_T	*Applied moment due to thermally induced displacements*
M_W	*Applied moment due to the pile head rotation under superstructure dead load*
M_{yy}	*Yield moment*
M_{Max}^{+ve}	*Maximum positive moment*

M_{Max}^{-ve}	*Maximum negative moment*
m	*Power of stress-level dependency of stiffness*
$N_{1(60)}$	*Corrected average SPT value*
n	*Number of discrete increments along the beam element*
P_B	*Base wind pressure*
P_D	*Design wind pressure*
P_{Pu}	*Ultimate passive pressure*
P_T	*Applied axial force due to thermal contractions and expansions*
P_W	*Applied axial stress on the pile due to superstructure dead load*
p-y	*Lateral soil stress – strain relationship*
p_f	*Design pressure on foundation*
p_{ref}	*Reference confining pressure*
q-z	*Base soil stress – strain relationship*
R_{int}	*Interface strength reduction factor*
R_R	*Factored pile group uplift resistance*
R_s	*Axial skin resistance of an individual pile*
R_{ug}	*Pile group nominal uplift resistance*
S	*Vertical settlement*
S_c	*Settlement due to primary consolidation*
$\bar{S}_u$	*Undrained shear strength of soil*
S'	*Section modulus*
T	*Time*
T_G	*Temperature gradient*
T_{Max}	*Maximum temperature*
T_{Min}	*Minimum temperature*
T_{UG}	*Average temperature across the cross-section*
T_U	*Uniform specified temperature*
T_1	*Design temperature gradient in zone 1*
T_2	*Design temperature gradient in zone 2*
T_3	*Design temperature gradient in zone 3*
t	*thickness of RC deck*

t_f	*Pile flange thickness*
V_B	*Base wind velocity equal to 100 mph*
V_{DZ}	*Design wind velocity at the design elevation*
V_o	*Friction velocity*
V_{30}	*Wind velocity at 30 ft above the design water table elevation*
W_g	*Combined weight of soil, piles, and pile cap*
X	*Width of pile group*
Y	*Length of pile group*
Y_c	*Restraint moment due to creep under presstress forces*
Y_{DL}	*Restraint moment due to dead loads and creep*
Y_{LL}	*Moment due to live and impact load*
Y_S	*Restraint moment due to shrinkage*
y	*Displacement shape function of pile*
Z	*Depth of pile group*
Z_o	*Upstream fetch friction length*
Z'	*Height of the bridge subjected to wind above 30 ft of the design water table elevation*
z	*Depth*
z_1	*Depth of soil below the abutment*
2D	*Two-Dimensional*
3D	*Three-Dimensional*
α	*Coefficient of thermal expansion*
γ	*Unit weight*
γ_{dry}	*Dry unit weight*
γ_{sat}	*Saturated unit weight*
ν	*Poisson's ratio*
Δ	*Induced lateral displacement at pile head*
Δ_b	*Pile head lateral displacement at which the actual extreme fiber bending stress equals the allowable bending stress of the pile*
Δ_g	*Lateral displacement at the base of the abutment*

Δ_i	*Pile lateral displacement capacity*
Δ_T	*Design range of thermal expansions and contractions*
ΔT	*Change in ambient temperatures*
$\Delta\delta$	*Thermally induced abutment displacement*
ϵ_{creep}	*Creep strain*
ϵ_{cu}	*Degree of ultimate creep strain*
$\epsilon_{elastic}$	*Elastic strain*
ϵ_s	*Strain due to differential shrinkage*
ϵ_{su}	*Ultimate shrinkage strain*
ε	*Strain*
ε_u	*Uniform axial strain*
^{o}	*Degree*
rad	*Radians*
σ_E	*Internal stress*
σ_p	*Preconsolidation stress*
σ'_{vo}	*Vertical effective stress at mid point of each soil layer*
$\Delta\sigma$	*Additional pressure due to superstructure*
ϕ	*Ratio of creep strain to elastic strain*
ϕ'	*Curvature*
φ'	*Internal friction angle of the soil*
φ_{ug}	*Resistance factor*
φ_{up}	*Resistance factor for uplift*
θ_w	*Pile rotation*
ψ	*Dilatancy*
ΔF_j^{i+1}	*Applied load vector at step i + 1*
$\left[K_j^i\right]_T$	*Tangential stiffness matrix comprised of conventional and geometric matrices during the previous step i*
ΔD_j^{i+1}	*Nodal displacement at step i + 1*

ACKNOWLEDGEMENTS

First and foremost, I would like to express my sincere gratitude to my supervisor Dr. Hany El Naggar for his endless support and guidance, and for believing in me and my abilities. You have always been there for me in my times of need. This research would not have been possible without your expertise and support. I thank you from the bottom of my heart.

I would also like to extend my appreciation to Dr. Scott Civjan (Professor at the University of Massachusetts Amherst) and Mr. Faseel Khan (Global Technical Support Engineer at Bently) for their assistance and additional guidance throughout my research.

To my family members Mohamed, Amal, Mai, Lamis, and Yousef, I can not express my endless appreciation and gratefulness for having you in my life. All of you managed to lift me up when I was down, and pushed me past my own limits. You were what motivated me to continue and fight till the end, and I would not be where I am today if it were not for your support. And to my niece, Talia, I am sorry I was not there to welcome you with warm arms during your birth. I love you all and I hope to see you soon.

I also want to thank all my friends who were there for me during my ups and downs and the wonderful times and laughs that we had together. Finally, I would like to express my gratefulness to Jyeah Nelle Serrano for having someone like you in my life. You made this journey possible for me with your endless support and motivation, and all the spontaneous outings we had together with Jyvy Nhell Serrano. I will forever cherish those memories. I can not express how thankful I am for having met you both. I wish you both good luck in your lives and endless happiness in your future.

CHAPTER 1 INTRODUCTION

1.1 Research Background

Bridges constructed prior to the 1930s utilized expansion and bearing joints, typically situated above bridge piers and between neighboring spans, to accommodate induced bridge movements and deformations, as indicated in Figure (1.1a) (Chang and Lee 2002; Kong et al. 2016). These deformations may be caused due to variations in ambient temperature and humidity levels, creep and shrinkage effects, dead and live induced axial and flexural strains, vehicle impact loads, seismic activities, and overloads. Bridges also resist secondary loads such as tilt and settlement, mining subsistence, and construction loads (Lee 1995). However, full-scale field investigations have indicated the shortcomings associated with the use of expansion and bearing joints. For instance, using expansion and bearing joints require significant maintenance costs, since these joints are susceptible to moisture-induced corrosions. Furthermore, sensitive structural components are prone to significant deterioration due to their exposure to salts and de-icing chemicals, thus compromising their structural performance. Significant unexpected stresses were observed to develop within the superstructure as empty voids within expansion joints were often clogged with frozen water and debris, thus hindering the contraction and expansion mechanisms of structural members (Lawver et al., 2000).

Consequently, the concept of integral abutment bridge (IAB) construction was first introduced during the 1930s, before rapidly becoming widespread after the 1960s (Arsoy et al. 1999; Kong et al. 2016). As shown in Figure (1.1b), IABs are continuous structures

which are distinguished by omitting the use of expansion and bearing joints. This is achieved by integrally casting the deck and abutments, and rigidly embedding the girders into the abutment. As a result, the superstructure and substructure are connected monolithically to act as a one rigid body in response to induced primary and secondary loads (LaFave et al. 2021). Incorporating such a configuration was found to reduce construction and maintenance costs, enhance seismic performances, lessen construction durations, improve vehicle riding quality, and increase the structure's service life (Abdel-Fattah and Abdel-Fattah 2019). IABs constructed in the US and Canada typically utilize a stub-type abutment supported by a single row of vertical steel HP piles oriented for weak-axis bending (Arockiasamy et al. 2004; Breña et al. 2007). Furthermore, common practices in North America involve drilling piles into over-sized holes filled with loose granular soils to reduce the down drag forces acting on the piles and resistance against lateral movements (Yang et al. 1985; Husain and Bagnariol 2000). However, a survey conducted by White II et al. (White II et al. 2010) indicated that IABs constructed in Europe commonly opt for flexible abutments supported by shallow foundations.

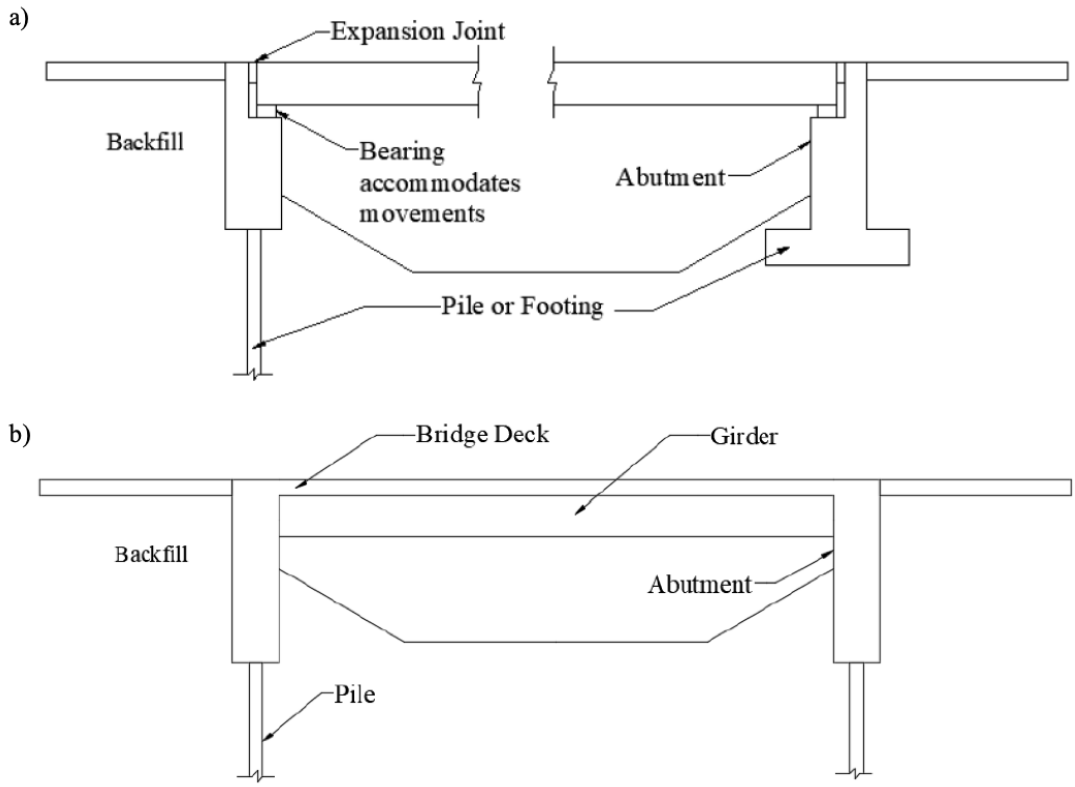

Figure 1.1 Typical bridge designs: **(a)** jointed bridge, **(b)** IAB (Li 2020)

Although IABs have several attributes, their soil-structure interactions (SSIs) under the influence of cyclic thermal loading are extremely complex and yet to be fully understood. Since IABs eliminate the use of expansion and bearing joints, laterally induced thermal loads cause a rigid body translation and rotation of the abutment and piles. Consequently, this mode of deformation may potentially increase the stresses within the piles and backfill soil significantly (Lawver et al., 2000). Furthermore, research conducted by Faraji et al. (Faraji et al. 2001) indicated that one of the challenges related to the use of IABs involves accurately idealizing the SSIs of IABs under induced thermal movements during design and analyses, since the behavior of the soil significantly impacts the corresponding

magnitudes of stresses generated within the backfill and supporting piles. If the induced abutment movements are large enough, the response of the soil, therefore, becomes highly nonlinear and varies as a function of the abutment displacement. Hence, a unified design and analysis approach is yet to be accomplished.

The SSIs of IABs are commonly analyzed via the *p-y* method or the full continuum approach. As part of the *p-y* method, structural members are idealized using finite element (FE) beam elements, divided into *n* intervals, with corresponding node endings. The behavior of the soil is approximated through a series of discrete and unconnected horizontal and vertical spring elements, connected to the structural member at the corresponding node endings (Potts and Zdravkovic 1999). While this is a simple and quick approximation of the complex SSIs related to IABs, this approach neglects and simplifies several geotechnical concepts and interactions such as: the continuous nature of soil in relation to SSIs, drainage, pore-water pressures, torsional soil resistance, and coupled axial and lateral soil resistance (Dhadse et al. 2021; Greimann et al. 1986).

The full continuum approach, however, is capable of realistically modelling complex SSIs that occur as IABs resist induced thermal loads such as changes in geometry, non-homogeneous material conditions, and nonlinear stress-strain behaviors. Unlike the *p-y* method, this approach considers the entirety of the problem as a full continuum discretized into finite elements. Elements are connected via node endings to form a global mesh (Abdel-Fattah and Abdel-Fattah 2019). Since each element incorporates a stiffness matrix, corresponding nodal displacements are thus determined based on the global loading and boundary conditions (Dutta and Roy 2002). In addition, this approach allows for the use of advanced constitutive soil models to simulate the nonlinear stress-strain response of soils

for various stress levels and paths, generation of pore-water pressures, and coupled consolidation analyses. Furthermore, the relative deformation, stress transfer, and slippage between the abutment-soil and pile-soil can be simulated by using zero thickness interface elements, whose properties depend on the parenting soil (Dhadse et al. 2021; Potts and Zdravkovic 1999).

As a stepping stone to better understand the complex response of IABs to thermal loading, several researchers have conducted full-scale investigations to monitor the thermal performance of IABs over a certain period (Huntley and Valsangkar 2013; Huntley and Valsangkar 2014; Kim and Laman 2012; Kong et al. 2015; LaFave et al. 2021). In addition, extensive numerical parametric studies were conducted to investigate the changes in the performance of IABs in response to varying model conditions (Civjan et al., 2007; Huang et al., 2008; Kalayci et al., 2012; Quinn and Civjan, 2017).

However, the numerical studies conducted by previous research utilized the *p-y* approach to simulate the SSIs of IABs under induced thermal contractions and expansions. Hence, this research aims to build upon previous work by analyzing and modelling the SSIs of IABs under thermal loadings within a continuous soil medium, with corresponding interface elements, using the full continuum approach. In accordance with the monitored IAB in Vermont, USA, advanced two- and three-dimensional FE models using the PLAXIS software are developed to mimic the thermal response of the structure, where the corresponding backfill earth pressures and pile bending moments are verified against available field measured data. In addition, comprehensive parametric studies are conducted to investigate the changes in earth pressure distributions and pile bending moments in

response to varying the constitutive soil model, thermal loading, backfill stiffness, abutment stiffness, pile size and orientation, and span length.

1.2 Research Objectives

This research aims to numerically analyze the thermal performance of IABs under induced cyclic thermal loadings within a continuous soil medium. For this thesis, the primary objectives of the conducted research can be stated as follows:

- Investigate the field measured thermal response of an integral abutment bridge in Vermont, USA.
- Develop comprehensive two- and three-dimensional finite element models using the full continuum approach to simulate the thermal response of abutment and verify the lateral earth pressure distributions and pile bending moments against field acquired data.
- Conduct parametric studies using the calibrated models to investigate the changes in earth pressures distributions and pile bending moments under various conditions.

1.3 Thesis Outline

The chapters contained in this thesis are ordered as follows:

- **Chapter 1** introduces the research topic for this thesis and the corresponding objectives.

- **Chapter 2** presents extensive details related to the IAB construction and design concepts. Moreover, this chapter compares current design practices and guidelines employed across various regions worldwide.
- **Chapter 3** presents the results of the conducted two-dimensional modelling of integral abutment bridges. The content of this chapter is currently under consideration to be published as a journal paper in the Transportation Geotechnics Journal.
- **Chapter 4** presents the results of the conducted three-dimensional modelling of integral abutment bridges. The content of this chapter is also under consideration to be published as a journal paper in the Transportation Geotechnics Journal .
- **Chapter 5** summarizes the key findings described in this thesis, along with recommendations for future work.

References

Abdel-Fattah, M.T. and Abdel-Fattah, T.T., (2019). Behavior of Integral Frame Abutment Bridges Due to Cyclic Thermal Loading: Nonlinear Finite-Element Analysis. *Journal of Bridge Engineering*, 24(5). https://doi.org/10.1061/(ASCE)BE.1943-5592.0001394

Arockiasamy, M., Butrieng, N., Sivakumar, M., (2004). State-of-the-Art of Integral Abutment Bridges Design and Practice. *Journal of Bridge Engineering*, 9(5), 497-506. https://doi.org/10.1061/(ASCE)1084-0702(2004)9:5(497)

Arsoy, S., Barker, R. M., and Duncan, J. M., (1999). The behavior of integral abutment bridges. *Rep. No. FHWA/VTRC 00-CR3*, Virginia Transportation Research Council, Charlottesville, Va.

Breña, S.F., Bonczar, C.H., Civjan, S.A., DeJong, J.T., Crovo, D.S., (2007). Evaluation of Seasonal and Yearly Behavior of an Integral Abutment Bridge. *Journal of Bridge Engineering*, 12(3), 296-305. https://doi.org/10.1061/(ASCE)1084-0702(2007)12:3(296)

Chang L.M. and Lee, Y.J., (2002). Evaluation of Performance of Bridge Deck Expansion Joints. *Journal of Performance of Constructed Facilities*, 16(1), 3-9. https://doi.org/10.1061/(ASCE)0887-3828(2002)16:1(3)

Civjan, S.A., Bonczar, C., Breña, S.F., DeJong, J., Crovo, D., (2007). Integral Abutment Bridge Behavior: Parametric Analysis of a Massachusetts Bridge. *Journal of Bridge Engineering*, 12(1), 64-71. https://doi.org/10.1061/(ASCE)1084-0702(2007)12:1(64)

Dhadse, G.D., Ramtekkar, G.D., Bhatt, G., (2021). Finite Element Modeling of Soil Structure Interaction System with Interface: A Review. *Archives of Computational Methods in Engineering*, 28, 3415-3432. https://doi.org/10.1007/s11831-020-09505-2

Dutta, S.C. and Roy, R., (2002). A critical review on idealization and modeling for interaction among soil-foundation-structure system. *Computers and Structures*, 80(20-21), 1579-1594. https://doi.org/10.1016/S0045-7949(02)00115-3

Faraji, S., Ting, J.M., Crovo, D.S., Ernst, H., (2001). Nonlinear Analysis of Integral Bridges: Finite-Element Model. *Journal of Geotechnical and Geoenvironmental Engineering*, 127(5), 454-461. https://doi.org/10.1061/(ASCE)1090-0241(2001)127:5(454)

Greimann, L.F., Yang, P.S., Wolde-Tinsae, A.M., (1986). Nonlinear analysis of Integral Abutment Bridges. *Journal of Structural Engineering*, 112(10), 2263-2280. https://doi.org/10.1061/(ASCE)0733-9445(1986)112:10(2263)

Huang, J., Shield, C.K., French, C.E.W., (2008). Parametric Study of Concrete Integral Abutment Bridges. *Journal of Bridge Engineering*, 13(5), 511-526. https://doi.org/10.1061/(ASCE)1084-0702(2008)13:5(511)

Huntley, S.A. and Valsangkar, A.J., (2013). Field monitoring of earth pressures on integral bridge abutments. *Canadian Geotechnical Journal*, 50(8), 841-857. https://doi.org/10.1139/cgj-2012-0440

Huntley, S.A. and Valsangkar, A.J., (2014). Behavior of H-piles supporting an integral abutment bridge. *Canadian Geotechnical Journal*, 51(7), 713-734. https://doi.org/10.1139/cgj-2013-0254

Husain, I. and Bagnariol, D., (2000). Design and Performance of Jointless Bridges in Ontario: New Technical and Material Concepts. *Transportation Research Record*, 1696(1), 109-121. https://doi.org/10.3141%2F1696-14

Kalayci, E., Civjan, S.A., Breña, S.F., (2012). Parametric study on the thermal response of curved integral abutment bridges. *Engineering Structures*, 43, 129-138. https://doi.org/10.1016/j.engstruct.2012.05.007

Kim, W.S., Laman, J.A., (2012). Seven-Year Field Monitoring of Four Integral Abutment Bridges. *Journal of Performance of Constructed Facilities*, 26(1), 54-64. https://doi.org/10.1061/(ASCE)CF.1943-5509.0000250

Kong, B., Cai, C.S., Kong, X., (2015). Field monitoring study of an integral abutment bridge supported by precast concrete piles on soft soils. *Engineering Structures*, 104, 18-31. https://doi.org/10.1016/j.engstruct.2015.09.004

Kong, B., Cai, C.S., Zhang, Y., (2016). Parametric study of an integral abutment bridge supported by prestressed precast concrete piles. *Engineering Structures*, 120, 37-48. https://doi.org/10.1016/j.engstruct.2016.04.034

LaFave, J.M., Brambila, G., Kode, U., Liu, G., Fahnestock, L.A., (2021). Field Behavior of Integral Abutment Bridges under Thermal Loading. *Journal of Bridge Engineering*, 26(4). https://doi.org/10.1061/(ASCE)BE.1943-5592.0001677

Lawver, A., French, C., Shield, C.K., (2000). Field Performance of Integral Abutment Bridge. *Transportation Research Record*, 1740(1), 108-117. https://doi.org/10.3141%2F1740-14

Lee, D. J. (1994). *Bridge bearing and expansion joints*. 2nd Ed., E & FN Spon, London.

Li, B. (2020). *Geo-structural Analysis of Integral Abutment Bridges*. Electronic Thesis and Dissertation Repository. 7540. https://ir.lib.uwo.ca/etd/7540/

Potts, D. M., and Zdravkovic, L., (2001). *Finite element analysis in geotechnical engineering. Application*, Thomas Telford, London.

Quinn, B.H. and Civjan, S.A., (2017). Parametric Study on Effects of Pile Orientation in Integral Abutment Bridges. *Journal of Bridge Engineering*, 22(4). https://doi.org/10.1061/(ASCE)BE.1943-5592.0000952

White II, H., Pétursson, H., Collin, P., (2010). Integral Abutment Bridges: The European Way. *Practice Periodical on Structural Design and Construction*, 15(3), 201-208. https://doi.org/10.1061/(ASCE)SC.1943-5576.0000053

Yang, P.S., Wolde-Tinsae, A.M., Greimann, L.F., (1985). Effects of Predrilling and Layered Soils on Piles. *Journal of Geotechnical Engineering*, 111(1), 18-31. https://doi.org/10.1061/(ASCE)0733-9410(1985)111:1(18)

CHAPTER 2 LITERATURE REVIEW

Jointed bridges have been commonly constructed by transportation networks worldwide to provide alternative traffic routes over a variety of crossings (Zhao and Tonias 2014). However, according to statics gathered by the U.S. Department of Transportation, it was found that the number of structurally deficient bridges exceeded 27% by the year 2003. Thus, bridge engineers have begun to realize the numerous shortcomings associated with the use of deck and bearing joints. During the early 1930s, engineering practitioners began to transition towards constructed joint-less bridges by eliminating expansion and bearing joints. Such structures are categorized as integral abutment bridges (IABs). Approaching the late 1960s, IAB construction significantly grew in popularity becoming widespread in North America and Europe. It was soon realized however, that opting for such structures would lead to significantly larger secondary stresses within the superstructure. Nevertheless, the shortcomings related with jointed bridges considerably outweighed those associated with joint-less bridges (Burke 2009).

The structural and economical performances of jointed bridges were seen to be inferior to IABs since these structures require constant maintenance and operate for short periods of time. According to Burke (Burke 2009), jointed bridges are associated with two major shortcomings. Firstly, under thermally induced contractions and expansions, corresponding pavement growths lead to the closure of the deck joints. This induces substantial compressive pavement pressures on the abutment, girders, and deck components, thus potentially invoking severe structural ruptures. In some instances, these stresses were seen to exceed approximately 7000 kPa. Moreover, induced compressive stresses because of pavement growth were seen to cause wing-walls and piers to fracture

and crack, respectively. Secondly, by utilizing expansion and bearing joints, structural elements are susceptible to corrosion and deterioration due to the leaking of de-icing chemicals used to dry pavements in areas with extreme snow and rain falls. This led to closure of several bridges for repair and maintenance, and in some instances, bridges were seen to collapse due to loss in durability and structural failures (Burke 2009).

With departments of transportation (DOTs) gradually transitioning to the construction of IABs, existing jointed bridges were retrofitted into continuous spans. This was first seen in the 1960s by DOTs in the states of Massachusetts and Wisconsin (Burke 2009). A survey conducted by Burke (Burke 2009) saw that approximately 30% of the DOTs have successfully retrofitted at least one bridge. Furthermore, as indicated by Hassiotis et al. (Hassiotis et al. 2006), a conducted survey showed that 20 DOTs transitioned to the construction of IABs over jointed bridges. This was strongly influenced by the high rehabilitation costs required to maintain such structures. For example, a study conducted in New York in 1992 concluded that the transformation of existing bridges to encompass continuous spans resulted in the annual saving of $0.5 – $1.25 million associated with maintenance. In addition, research conducted by Tabrizi et al. (Tabrizi et al. 2016) saw that the required costs to replace a deteriorated bridge joint ranged between $188,000 – $285,000. Research conducted by Weyers et al. (Weyers et al. 1988) in which the cost-effective bridge maintenance and rehabilitation procedures were discussed indicated that the minimum cost required to restore 22,500 bridges in Pennsylvania was $2.5 billion.

As defined by Burke (Burke 2009), IABs are single or multi spanned bridges in which the superstructure and abutments/piers are constructed monolithically, deprived of expansion and bearing joints. This results in a continuously rigid assembly between the superstructure

and substructure components as shown in Figure (2.1). A survey conducted by Arockiasamy et al. (Arockiasamy et al. 2004) indicated that most of DOTs across Canada and the United States do not follow special considerations when designing the bridge girders and deck. However, during the design of the superstructure, a fixed condition between the superstructure and abutment is assumed. Furthermore, IAB girders and deck are designed to induce equal displacements at each abutment and resist induced secondary stresses under time-dependent effects. IABs commonly utilize pre-stressed concrete and steel webbed girders to support a reinforced concrete (RC) deck. Typically, pre-stressed concrete girders are rigidly connected to the abutments via dowels, while steel webbed girders usually rest on a base cap plate rigidly connected to the pile cap (Arockiasamy et al. 2004).

Arockiasamy et al. (Arockiasamy et al. 2004) indicated that the foundations of most IABs utilize a stub-type abutment. Depending on the geographical area, abutments are either constructed as shallow or deep foundations. A study conducted by Caristo et al. (Caristo et al. 2018) to numerically investigate the thermal response of IABs under cyclic loading specified that European regions utilize either full-height or slide-on-backfill shallow foundations. Thus, under lateral loading, induced contractions and expansions are accommodated via the flexural flexibility of the reinforced abutments. Accordingly, the abutments distribute the corresponding stresses amongst the backfill soil, pavements, and foundations (Arockiasamy et al. 2004). A survey conducted by Soltani and Kukreti (Soltani and Kukreti 1992) found that the design of IAB abutments is closely related to the magnitude of backfill passive stresses, since inadequately designed abutments are susceptible to cracking under considerable passive stresses.

However, within North America, it was stated that abutments are commonly supported by piles, where induced lateral loadings due to temperature and shrinkage effects are accommodated via the flexibility and fatigue resistance of the piles. LaFave et al. (LaFave et al. 2016) also stated that some IAB piles are designed to exceed the material's yield strength under thermally induced cyclic loadings by forming plastic hinges. As part of the design process, the pile and soil response to lateral loading are analyzed simultaneously, since the deflection of the pile depends on the resistance provided by the soil and vice versa. Thus, the lateral response of the soil is a nonlinear function of the pile deflection (Arockiasamy et al. 2004). A report prepared for the Indiana Department of Transportation in 2011 by Frosch and Lovell (Frosch and Lovell 2011) indicated that IABs constructed in Indiana can only be supported by using steel H-piles oriented about the weak axis of bending or concrete filled steel pipe piles.

Multi-spanned IABs are either constructed using rigid piers with movable bearings or flexible piers rigidly connected with the girder and deck components (Burke 2009). However, according to the New Jersey DOT, pier bearings are only to be fixed when the induced expansions from the bearings to the bridge abutments or neighboring piers are equal. IAB piers are designed to resist and distribute considerable lateral and longitudinal induced movements from the superstructure to the foundations, respectively. Thus, the magnitudes of such stresses must be considered during the design phase to adopt appropriate pier and foundation sizes (Arockiasamy et al. 2004).

Poured separately from the abutment and superstructure, RC approach slabs are designed to provide a smooth transition to the bridge in the event of backfill settlement. Furthermore, these slabs aid in the distribution of vehicle stresses over a greater area, thus reducing

abutment damages corresponding to impact stresses. RC approach slabs also enhance roadway drainage, and therefore mitigating erosion and freezing/thawing effects in saturated backfills (Arockiasamy et al. 2004).

Cantilevered wing-walls are designed to retain soils beyond the width of the abutment back-wall. Canadian and American practices typically utilize parallel, flared, and U-type wing-walls. Kunin and Alampalli (Kunin and Alampalli 2000) indicated that these components are designed independently of the abutments to minimize their relative movement with the abutment under induced contractions and expansions. The orientation of the wing-walls significantly impact the corresponding passive pressures behind the abutment wall during induced expansions. It was seen that compared to transverse wing-walls, U-type wing walls resulted in greater passive earth distributions. However, flared and U-type wing-walls are commonly adopted to prevent scouring effects owing to stream velocities and alignments (Arockiasamy et al. 2004).

Piles accommodate induced superstructure expansions and contractions by laterally displacing within the subgrade soil. However, the extent of lateral pile movements under induced displacements is dependent on the resistance provided by the surrounding soil. Thus, in stiffer soils, the corresponding pile stresses under induced lateral contractions and expansions increase. However, research conducted by Arsoy et al. (Arsoy et al. 1999) indicated that for IABs, the aim is to minimize the generated stresses within the foundation piles. Therefore, IABs constructed above stiff soil involve driving piles into predrilled holes filled with granular soils such as loose sand or pea stone to reduce corresponding pile stresses (Breña et al. 2007; Husain and Bagnariol 2000). Similarly, research conducted by Yang et al. (Yang et al. 1985) indicated that within the state of Iowa, piles supporting IABs

with a total length exceeding 40 m are to be driven into predrilled holes with a minimum depth of 2.6 m below the base of the abutment. Finally, the use of predrilled holes has also been recommended to reduce the down drag forces acting on the piles (Yang et al. 1985).

The design procedure of IABs comprises of several steps, and can be summarized as the following. Firstly, general bridge dimensions such as width, length, and overhead clearances are specified according to highway engineer requirements. Then, initial designs of girders, deck, and piers are assumed according to minimum design requirements based on the AASHTO bridge design manual. This is then following by determining the loads acting on the bridge, with the corresponding load combinations. The structural capacity of the initial superstructure design is compared to the applied stresses to ensure adequate resistance is provided. If the applied stresses exceed the resisting capacity of the superstore, initial designs are revised accordingly. Finally, stresses acting on the foundation are utilized to design the bridge piles, where the number and type of piles, spacing, and embedment lengths are determined (AASHTO 2020).

Due to the relatively recent introduction of IABs, their design guidelines and criteria widely vary across different regions, since they are based on engineering judgements and experience. Thus, precise and uniform design criteria and guidelines are yet to exist. This paper aims to provide a comprehensive review on IABs and the various design considerations and criteria specified in the literature and DOTs worldwide. First, the attributes and shortcomings associated with the use of IABs are highlighted. Then details on the various types of loads acting on IABs are described along with the corresponding state-of-the-art design load determination methods. This is then followed by the description of a rational design and analysis method of IABs piles used in current practices. Finally,

IAB design guidelines and criteria specified by DOTs around the world are compared with the corresponding design limits found in the literature.

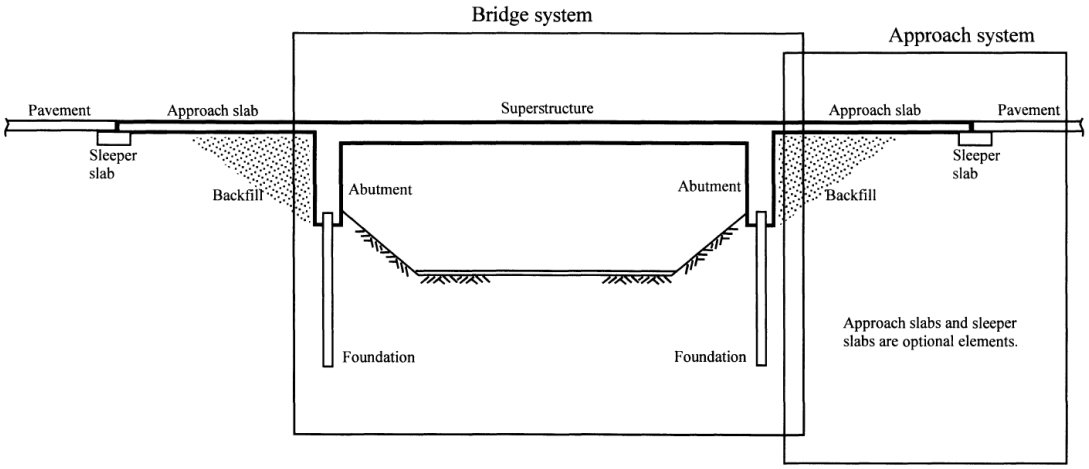

Figure 2.1 Design concept of IAB (Arsoy et al. 1999)

2.1 Advantages and disadvantages of IABs

IAB construction has recently become more widespread, since eliminating expansion and bearing joints resulted in enhanced structural and economical performances (Mourad and Tabsh 1999). However, due to the joint-less nature of these structures, researchers have also indicated the limitations of incorporating continuous spans. Hence, this section highlights the attributes and limitations of using IABs.

2.1.1 Attributes

IAB construction has been associated with lower construction costs owing to the absence of expansion and bearing joints (Soltani and Kukreti 1992). The costs linked to maintaining

IABs have also been seen to decrease, since the absence of bridge joints have prevented the deterioration and damaging of the bridge deck under the operation of snow ploughs. In addition, the continuous nature of IABs have reduced the costs of maintaining corroded superstructure and substructure elements caused by water leakages (Kaufmann and Alvarez 2011). Research conducted by Frosch et al. (Frosch et al. 2009) and Hoppe and Gomez (Hoppe and Gomez 1996) to evaluate the behavior of IABs under seismic activities have indicated that these structures exhibited enhanced seismic performances owing to their continuous and redundant design. IABs encompass simpler foundations since these structures utilize a single row of piles as opposed to the complex battered foundations of conventional bridges (Burke 2009; Mourad and Tabsh 1999; Soltani and Kukreti 1992). Owing to their continuous and monolithic nature, IABs have been associated with rapid construction times and efficient designs (Burke 2009; Chovichien 2004). As described by Burke (Burke 2009), these structures can be designed to encompass larger end span ratios due to the large weights of the bridge diaphragms, approach slabs, and wing-walls. Finally, since IABs deprive the use of expansion joints, this corresponded to smoother riding experiences and comfort (Soltani and Kukreti 1992).

2.1.2 Limitations

Given the many desirable attributes associated with IABs, researchers have also indicated their limitations. First, piles supporting IABs are susceptible to the exceeding the yield strength of the pile material, and in some cases, develop plastic hinges. This owed to considerably high magnitudes of flexural stress induced to the bridge piles during contractive and expansive movements (Burke 2009). Furthermore, induced lateral stresses have resulted in reducing the axial resisting capabilities of the piles under combined

loading (Chovichien 2004). Under cyclic lateral contractions and expansions, significant longitudinal compressive stresses are induced upon the approach slab, abutment, and superstructure of IABs as debris accumulates within pavement segment cracks. Consequently, this leads to the structural failures of the bridge superstructure and approach systems (Hoppe and Gomez 1996). An experimental study conducted by England et al. (England et al. 2000) indicated that under induced abutment contractions and expansions, IABs are susceptible to experience soil ratcheting due to their joint-less nature. This involves the gradual accumulation of permanent strains in settled soil wedges at the backfill-abutment interface, thus significantly increasing the corresponding passive pressures during consecutive expansive cycles (Khodair 2009). The first consequence of this phenomenon is the possible failure of the abutment with considerable structural distress. The second corresponds either to the formation of a bump at the surface of the abutment back wall, or the flexural failure of the approach system (Hovarth 2005). Finally, as IABs are susceptible to differential settlements under induced thermal movements, considerable shear and bending stresses develop within the bridge deck and girders as a result (Chovichien 2004).

2.2 Loads on IABs

Loads subjected on integral abutment bridges (IABs) are categorized into three major groups: **(1)** primary loads; **(2)** secondary loads; and **(3)** seismic loads. Primary loadings acting on IABs comprise of dead loads, live plus impact loads, and wind loads, while secondary loads consist of creep and shrinkage effects, thermal gradients, differential

settlements, buoyancy, pavement growth, and thermal loads (Arockiasamy et al. 2004; Arsoy et al. 1999). Details concerning the types of loads acting on IABs are presented below.

2.2.1 Primary loads

Primary loads acting on IABs comprise of permanent loads (dead loads) sourcing from the self-weight of structural components such as girders, reinforced concrete (RC) deck, diaphragms, approach slabs, steel reinforcements, and RC railings, and temporary loads due to live plus impact loads and wind loads (Zhao and Tonias 2014).

2.2.2 Secondary loads

Effects due to creep are time-dependent effects since their impact on the structural performance of IABs occur over time. Under prolonged loading, concrete components within IABs such as the deck and girders undergo creep induced deformations due to the following. Subsequent to construction, the initial loadings acting on concrete components induce instantaneous strains. As these loads are sustained over time, creep strains which are approximately three times the magnitude of those applied initially are induced to the deck and girder components (Zhao and Tonias 2014). This effect generates additional stresses which magnify the curvatures and deflections within the superstructure (Arockiasamy et al. 2004; Munuswamy 2004). However, it was seen that the degree of creep induced deformations primarily depends on the age of the concrete (Zhao and Tonias 2014). As the maturity of the concrete increases, under the influence of sustained loading,

induced creep strains were seen to decrease. In addition, it was indicated that factors such as the humidity of the air and the concrete water/cement ratio were seen to limit the extent of creep. As humidity levels decrease, the effects of creep were seen to increase accordingly (Munuswamy 2004). Ultimately, creep induced deformations were seen to correspond to positive moments within the superstructure of IABs (Freyermuth 1969).

Shrinkage, another time-dependent effect, occurs as the volume of the concrete girders and deck decrease due to moisture losses during drying periods. Thus, factors such as humidity levels and concrete water/cement ratio significantly influence the degree of shrinkage (Zhao and Tonias 2014). As opposed to positive moments induced due to creep, shrinkage induces negative moments within the superstructure (Freyermuth 1969).

Thermal gradients within IABs are nonlinear temperature variations which occur over the depth of the bridge girders. These thermal variations are caused by the combined effects of ambient temperature fluctuations and the low thermal conductivity of concrete. This induces secondary stresses and moments within the superstructure, which may result in concrete cracking and serviceability failures if not accounted for. The magnitudes of these thermal gradients were seen to depend on the geometry of the bridge, site location, orientation, properties of the bridge, thermal conditions, and the presence of asphalt above the deck (Rodriguez et al. 2014).

During the service life of IABs, abutments and piers are susceptible to settlement under induced thermal contractions and expansions. These uneven settlements can compromise the riding quality, bridge aesthetics, structural integrity, load distributing capabilities, and safety of the structure. As a result of differential settlements at the abutment, support reactions and girder stresses and moments were seen to increase (Grover 1978;

Walkinshaw 1978). The mode by which IABs settle are categorized intro three major types: **(1)** uniform; **(2)** tilt; and **(3)** non-uniform. Uniform settlements correspond to the equal settlements of abutment and pier foundations. Based on research conducted by Bozozuk (Bozozuk 1978) and Yokel (Yokel 1990), it was concluded that uniform settlement does not correspond to deck and girder distortions. However, Wahls (Wahls 1990) indicated that uniform bridge settlements give rise to bumps at the approach system of IABs and may affect the drainage within the backfill soil. Tilt or rotation settlements cause abutment and pier foundations to settlement via linear patterns along the length of the bridge. This type of settlement is typically common in single-spanned bridges due to their relatively high stiffness. The impacts corresponding to tilt or rotation settlements are like those caused during uniform settlements. Non-uniform settlements were seen to primarily occur in bridges with three or more spans. In this mode, bridges can follow a regular or irregular settlement pattern, with irregular settlements causing larger superstructure distortions compared to regular settlements. During the event of regular non-uniform settlements, downward movements occur primarily at mid-span. However, during irregular non-uniform settlements, movements vary irregularly with length. Ultimately, non-uniform settlements induce significant secondary girder moments and stresses and increase reactions at the abutments (Barker et al. 1991).

Owing to the continuous nature of IABs, locations with high water levels may induce high uplift forces due to buoyancy when fully submerged. This corresponds to additional stresses and moments within the deck and girders. Given that the self-weight of the bridge counters such forces, additional design provisions to minimize buoyancy effects must be considered (Burke 2009).

IABs are strongly susceptible to pavement growth effects due to the absence of expansion joints. Decreases in ambient temperatures and moisture levels induce contractions within pavement segments at saw-cut locations. During such periods, extremely stiff roadway debris deposit and accumulate beneath the surface of the saw-cuts. Thus, during periods of pavement expansions as ambient temperatures increase, accumulated debris prevent the full closure of the pavement cracks. Under sustained debris accumulation and the cyclic contraction and expansion, pavement segments were seen to significantly elongate, therefore inducing longitudinal compressive stresses to the abutment and girders. These induced compressive stresses may lead to the minor fracturing and violent rupturing of the bridge abutments and girders, respectively (Burke 2009).

As ambient temperatures rise, the corresponding girders and deck composite expand. This induces an axial compressive force on the bridge abutment causing it to displace into the backfill soil. The lateral extent of abutment expansions is dependent on the material of the superstructure, the magnitude of the temperature change, and the backfill stiffness. Research conducted by Arsoy et al. (Arsoy et al. 1999) indicated that under seasonal expansions, IABs rotate and translate. However, research conducted by Huntley and Valsangkar (Huntley and Valsangkar 2013) saw that the primary mode of abutment expansion was abutment translation. Nevertheless, the degree and mode of abutment expansion was seen to influence the corresponding passive earth pressures. Due to the continuous nature of IABs, as the abutment contracts, a void is created where the backfill soil is invited to settle and rearrange behind the abutment wall, since these structures typically retain granular soil (Arockiasamy et al. 2004). This results in a soil wedge at the backfill – abutment interface. During periods of expansion, the backfill soil applies passive

stresses on the bridge abutment. Since the behavior of soil is highly nonlinear, the settled soil wedge prevents the full recovery of the abutment during expansive cycles. With cyclic abutment contractions and expansions, the soil wedge at the abutment wall interface accumulates irreversible strains, which corresponding to the strain response of the granular backfill during loading and unloading stress paths. This phenomenon is known as soil ratcheting. Ultimately, this leads to the gradual increase of passive stresses applied to the bridge abutment with each expansive cycle, which may lead to the formation of abutment cracks (Khodair 2009).

2.3 Load calculations

Following the discussion of the types of loads acting on IABs, this section introduces the state-of-the-art design methods used to determine the response of IABs under induced secondary loadings.

2.3.1 Shrinkage and creep

As the time-dependent effects of shrinkage and creep occur simultaneously, research conducted by Freyermuth (Freyermuth 1969) provided analytical solutions which approximate the total positive restraint moments in IABs bridges corresponding to creep, shrinkage, dead loads, and live plus impact loads. Dead loads, live plus impact loads, and creep effects acting on IABs induced positive restraint moments, which are counteracted by shrinkage induced negative moments. Thus, the total positive moment over piers is expressed via Eq.1:

$$\boldsymbol{M_r = (Y_c - Y_{DL})\left(1 - e^{-\phi}\right) + Y_{LL} - Y_s\left(\frac{1-e^{-\phi}}{\phi}\right)} \quad \textbf{(1)}$$

where M_r is the total positive restraint moment over pier conncections (kN.m), Y_c is the restraint moment due to creep under pre-stress forces (kN.m), Y_{DL} is the restraint moment due to dead loads and creep (kN.m), Y_s is the restraint moment due to shrinkage (kN.m), Y_{LL} is the moment due to live and impact loads (kN.m), ϕ is the ratio of creep strain to elastic strain.

The effects due to creep $\left(1 - e^{-\phi}\right)$ can be determined via a five-step procedure for a given elastic strain. **(1)** For a concrete girder section with an initial modulus of elasticity E_i, the corresponding initial creep strain is acquired from Figure (2.2); **(2)** the creep strain from step 1 is then adjusted via a correction factor obtained from Figure (2.3) which considers the age of the concrete at loading; **(3)** given the volume to surface ratio of the girder, the value from step 2 is then multiplied by a size coefficient factor for creep as shown in Figure (2.4); **(4)** Using Figure (2.5), the degree to which the ultimate creep strain ($\epsilon_{cu}\%$) has occurred when the girder and abutment form a fixed connection is determined. Accordingly, the creep strain (ϵ_{creep}) is the product of the value obtained in step 3 and ($1 - \epsilon_{cu}\%$). Therefore, the ratio of creep strain to elastic strain (ϕ) is then determined via $\left(\frac{\epsilon_{creep}}{\epsilon_{elastic}}\right)$; **(5)** Finally, using ϕ, the restraint moment creep factor correspond to the curves $\left(1 - e^{-\phi}\right)$ or $\left(\frac{1-e^{-\phi}}{\emptyset}\right)$ is then determined via Figure (2.6) accordingly.

Assuming that girders behave elastically under induced negative moments due to shrinkage along the length of the superstructure, the shrinkage moment (Y_s) is given by Eq.2:

$$\boldsymbol{Y_s = \epsilon_s E_b A_b \left(e_2' + \frac{t}{2}\right)} \quad \textbf{(2)}$$

where E_b is modulus of elasticity of the RC deck (kPa), A_b is the cross-sectional area of the RC deck (m^2), $\left(e_2' + \frac{t}{2}\right)$ is the distance between the RC deck midpoint and the centroid of the composite superstructure (m), t is the thickness of the RC deck (m), and ϵ_s is the strain due to differential shrinkage. By conducting tests on a specimen obtained from the material mix utilized during the construction of the superstructure, the strain due to differential shrinkage (ϵ_s) is approximated via Eq.3:

$$\boldsymbol{\epsilon_s = \frac{\epsilon_{su} T}{N_s + T}} \quad \textbf{(3)}$$

where T is the time (days), ϵ_{su} is the ultimate shrinkage strain at time T equal to infinity, N_s is equal to $26e^{\frac{0.36V}{S}}$, and $\frac{V}{S}$ is the volume to surface ratio of the specimen. However, in the absence of measured data, Freyermuth (Freyermuth 1969) first suggested to assume an ultimate shrinkage strain (ϵ_{su}) at a relative humidity of 50% (correct for high or low humidity levels). The differential shrinkage (ϵ_s) is therefore the product of the assumed ultimate shrinkage strain (ϵ_{su}) and the corresponding shrinkage strain at time T from Figure (2.5).

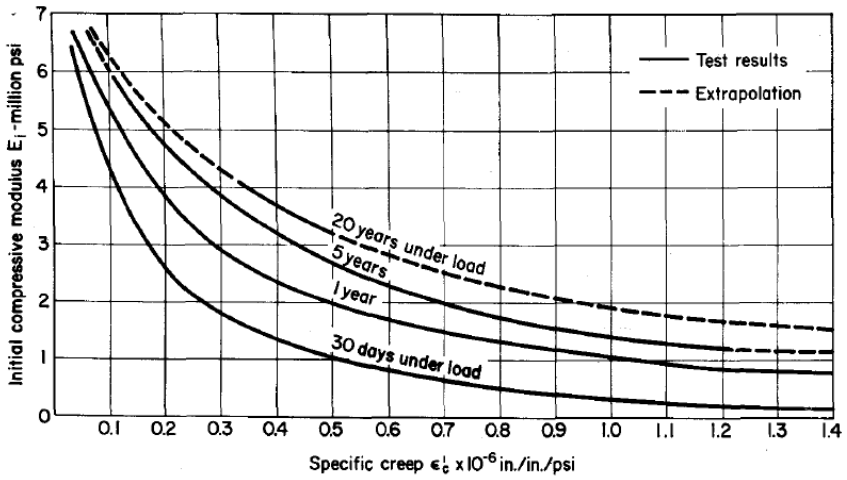

Figure 2.2 Approximation of initial creep as a function of the elastic modulus (Freyermuth 1969)

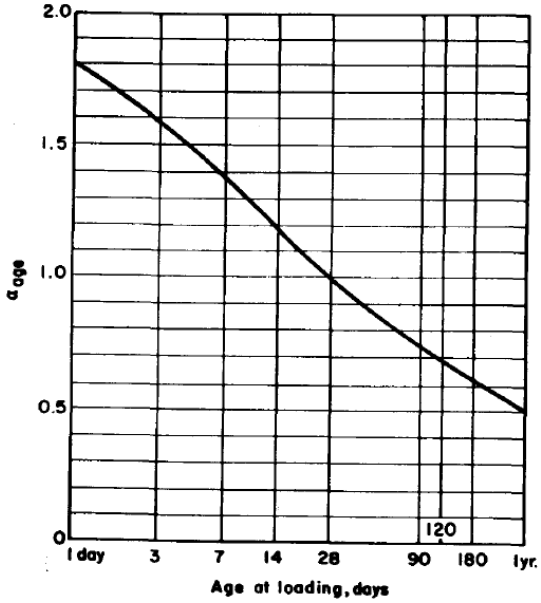

Figure 2.3 Age correction factor for creep (Freyermuth 1969)

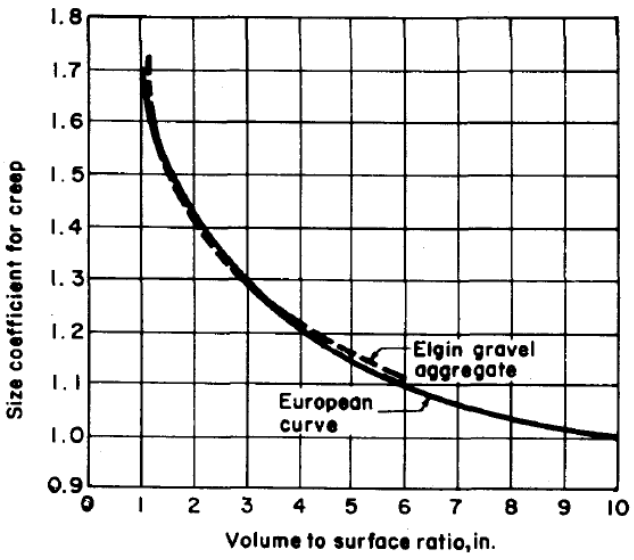

Figure 2.4 Size correction factor for creep as a function of volume-to-surface ratio (Freyermuth 1969)

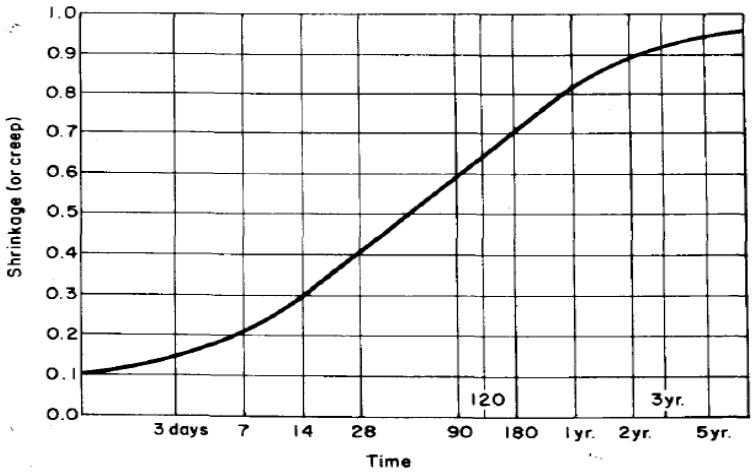

Figure 2.5 Degree of shrinkage/creep as a function of time (Freyermuth 1969)

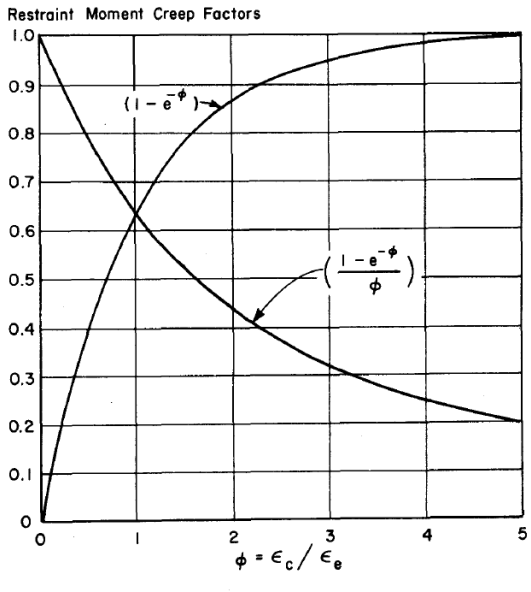

Figure 2.6 Creep restraint moment factor for shrinkage and creep (Freyermuth 1969)

2.3.2 Differential settlement

The settlement of abutment and pier foundations in cohesionless and cohesive soils can be estimated via several methods. Like shrinkage, the settlement of the abutments was seen to induce negative moments within continuous bridges. However, similar to the effects of creep, pier settlements induce positive moments within the superstructure (Burke 2009).

2.3.2.1 Cohesionless soils

A report prepared by Hannigan et al. (Hannigan et al. 2016) indicated that the approximation of elastic settlement via methods presented by Hough (1959) were conservative by a scale factor of 2. Thus, one of recommended techniques to predict vertical foundation settlement of IABs in cohesionless soil involved utilizing SPT test data.

Accordingly, the vertical settlement of a pile group in a homogenous cohesionless soil profile is given via Eq.4:

$$\boldsymbol{S = \frac{4 p_f I_f \sqrt{B}}{N_{1(60)}}} \quad \textbf{(4)}$$

and for silty sands, the vertical settlement can be estimated by Eq.5:

$$\boldsymbol{S = \frac{8 p_f I_f \sqrt{B}}{N_{1(60)}}} \quad \textbf{(5)}$$

where S is the predicted vertical settlement (in), p_f is the acting design pressure on the foundation (ksf), B is the width of the pile group (ft), $N_{1(60)}$ is the corrected average SPT value at depth equal to B below the pile toe, and I_f is the group embedment influence factor. I_f can be determined through Eq.6:

$$\boldsymbol{I_f = 1 - \frac{D'}{8B} \geq 0.5} \quad \textbf{(6)}$$

where $D^{'}$ is 2/3 the embedded length of the pile (ft).

2.3.2.2 Cohesive soils

When predicting pile settlement in cohesive soils, different equations have been provided for normally consolidated and overly consolidated soils. For normally consolidated soils where $\sigma^{'}_{vo} = \sigma_p$, the settlement is given by Eq.7:

$$S_c = \sum_i^n \frac{C_c}{1+e_o} H_o \, log \left(\frac{\sigma'_{vo}+\Delta\sigma}{\sigma'_{vo}} \right) \quad (7)$$

where S_c is the settlement due to primary consolidation (ft), e_o is the initial void ratio, H_o is the initial height of the soil layer (ft), σ_p is the preconsolidation stress (psf), σ'_{vo} is the vertical effective stress at the midpoint of each soil before loading (psf), $\Delta\sigma$ is the additional pressure due to the superstructure (psf), and C_c is the compression index obtained from a consolidation test.

For an overly consolidated soil where $\sigma'_{vo} + \Delta\sigma \leq \sigma_p$, the corresponding consolidation settlement is given by Eq.8:

$$S_c = \sum_i^n \frac{C_r}{1+e_o} H_o \, log \left(\frac{\sigma'_{vo}+\Delta\sigma}{\sigma'_{vo}} \right) \quad (8)$$

where S_c is the settlement due to primary consolidation (ft), e_o is the initial void ratio, H_o is the initial height of the soil layer (ft), σ_p is the preconsolidation stress (psf), σ'_{vo} is the vertical effective stress at the midpoint of each soil before loading (psf), $\Delta\sigma$ is the acting pressure due to the superstructure (psf), and C_r is the recompression index obtained from a consolidation test.

For an overly consolidated soil where $\sigma'_{vo} + \Delta\sigma > \sigma_p$, the consolidation settlement is expressed estimated through Eq.9:

$$S_c = \sum_i^n \frac{C_r}{1+e_o} H_o \, log \left(\frac{\sigma'_{vo}+\Delta\sigma}{\sigma'_{vo}} \right) + \frac{C_c}{1+e_o} H_o \, log \left(\frac{\sigma'_{vo}+\Delta\sigma}{\sigma'_{vo}} \right) \quad (9)$$

where S_c is the settlement due to primary consolidation (ft), e_o is the initial void ratio, H_o is the initial height of the soil layer (ft), σ_p is the preconsolidation stress (psf), σ'_{vo} is the vertical effective stress at the midpoint of each soil before loading (psf), $\Delta\sigma$ is the additional pressure due to the bridge superstructure (psf), C_r is the recompression index obtained from a consolidation test, and C_c is the compression index obtained from a consolidation test (Hannigan et al. 2016).

2.3.3 Passive earth pressures

As ambient temperatures increase, the deck and girders components induce lateral displacements onto the abutments, causing them to expand into the backfill soil. A method was proposed by Burke (Burke 2009) to predict the ultimate design passive pressure at the backfill-abutment wall interface via Eq.10:

$$P_{pu} = \gamma \tan\left(\frac{45+\varphi}{2}\right)^2 H + 2c \tan\left(\frac{45+\varphi}{2}\right)^2 \quad (10)$$

where P_{pu} is the ultimate passive stress (kPa), γ is the unit weight of the backfill soil (kN/m^3), φ is the internal angle of friction (degrees), H is the depth of the calculated pressure beneath the RC approach slab (m), and c is the soil cohesion (kPa). However, it was seen that only 2/3 of the ultimate passive pressure is consider in design for multi-span IABs.

2.3.4 Pavement growth

Induced compressive stresses at the abutment because of pavement growth can be approximated via a method described by Burke (Burke 2009). The induced compressive stress is proportional to the concrete strain via Eq.11:

$$\boldsymbol{f_c = E_c \varepsilon} \quad \textbf{(11)}$$

where f_c is the induced compressive stress due to pavement growth (kPa), E_c is the modulus of elasticity of concrete (kPa), and ε is the compressive stain. The strain ε is assumed to be equal to $0.0003L_s$, where L_s is the length of the pavement section between two contraction joints. Thus, by utilizing a unit strain, Eq.11 can be expressed via Eq.12:

$$\boldsymbol{f_c = 0.0003 E_c} \quad \textbf{(12)}$$

2.3.5 Buoyancy

In geographical areas where vertical uplift forces on IABs due to buoyancy are significant, the AASHTO LRFD bridge design specification manual (AASHTO 2020) considers uplift effects as the following.

Firstly, the total uplift force acting on an IAB is taken as the summation of the vertical components of the acting static pressures. Static pressures acting on the bridge is taken as the product of the specific weight of water and the height of water above the point of interest.

Secondly, during the design of the foundation piles, the uplift resisting capabilities of the pile group are evaluated. The resistance provided by the pile group against uplift is given by Eq.13:

$$\boldsymbol{R_R = \varphi_{ug} R_{ug}} \tag{13}$$

where R_R is the factored pile group uplift resistance (kN), φ_{ug} is the resistance factor equal to 0.5 for sand and clay subgrade soils, and R_{ug} is the pile group nominal uplift resistance (kN). The factor R_{ug} is taken as the lesser of the summation of the uplift resistance of a single pile or the uplift resistance of a block pile group.

For a single pile, the uplift resistance R_{ug} is given by Eq.14:

$$\boldsymbol{\sum_{i=1}^{n} R_R = \varphi_{up} R_s} \tag{14}$$

where φ_{up} is the uplift resistance factor equal to 0.35 for the Nordlund method, 0.25 for the α-method, 0.2 for the β-method, 0.3 for the λ-method, 0.25 for the SPT-method, 0.4 for the CPT-method, and 0.6 based on a load test. The term R_s is the axial skin resistance of an individual pile (kN).

The nominal uplift resistance of a pile group block in cohesive soils as shown in Figure (2.7a) is expressed via Eq.15:

$$\boldsymbol{R_{ug} = (2XZ + 2YZ)\bar{S}_u + W_g} \tag{15}$$

where X is the width of the pile group (m), Y is the length of the pile group (m), Z is the soil block depth (m), $\bar{S}_u$ is the undrained shear strength of the soil (kPa), and W_g is the combined weight of the soil, piles, and pile cap (kN).

For a pile group block in cohesionless soils as shown in Figure (2.7b), the weight of the block subjected to uplift forces is found by extrapolating a spread load beneath the base of the pile cap with a slope of 1H:4V, using the submerged unit weights of soil below the water table.

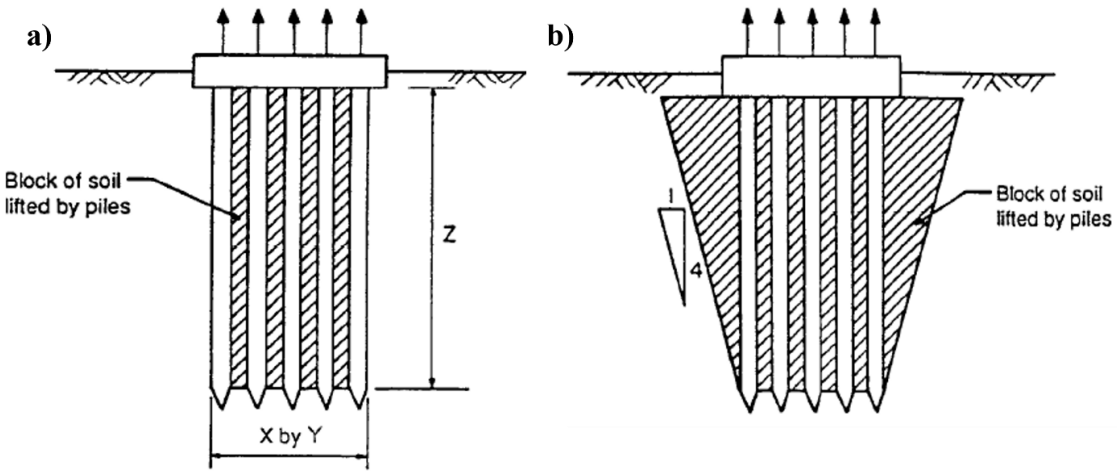

Figure 2.7 Buoyancy loads on pile groups in: **(a)** cohesive soils; and **(b)** cohesionless soils (AASHTO 2020)

2.3.6 Thermal gradient

When analyzing the effects of thermal gradients, the AASHTO LRFD bridge design specification manual (AASHTO 2020) considers the axial expansion, flexural deformation, and internal stresses within the superstructure as the following.

The axial expansion of the superstructure is the uniform component of the thermal distribution along the superstructure depth, where the corresponding uniform axial strain ε_u is given by Eq.16:

$$\boldsymbol{\varepsilon_u = \alpha(T_{UG} + T_u)} \tag{16}$$

where α is the coefficient of thermal expansion (m/m/°C), T_{UG} is the average temperature across the cross-section (°C), and T_u is the uniform specified temperature (°C). The average temperature across the cross-section is calculated via Eq.17:

$$\boldsymbol{T_{UG} = \frac{1}{A_c} \iint T_G \, dw \, dz} \tag{17}$$

where A_c is the cross-sectional area (transformed for steel beams) (m^2) and T_G is the temperature gradient (Δ°C).

The flexural deformation within the superstructure corresponding to thermal gradients is given by Eq.18:

$$\boldsymbol{M = EI_c \phi'} \tag{18}$$

where ϕ' is the curvature (1/m), E is the modulus of elasticity (kPa), and I_c is the moment of inertia of the cross-section (transformed for steel beams) (m^4). The curvature is therefore calculated using Eq.19:

$$\boldsymbol{\phi = \frac{\alpha}{I_c} \iint T_G z \, dw \, dz} \tag{19}$$

where α is the coefficient of thermal expansion (m/m/ºC), I_c is the moment of inertia of the cross-section (transformed for steel beams) (m^4), T_G is the temperature gradient (ΔºC), and z is the depth from the center of gravity of the cross-section (m).

Given that compressive stresses correspond to a positive value, the internal stress within the superstructure is given by Eq.20:

$$\boldsymbol{\sigma_E = E[\alpha T_G - \alpha T_{UG} - \phi z]} \quad \textbf{(20)}$$

where E is the modulus of elasticity (kPa), α is the coefficient of thermal expansion (m/m/ºC), T_G is the temperature gradient (ΔºC), T_{UG} is the average temperature across the cross-section (ºC), ϕ is the curvature (1/m), and z is the depth from the center of gravity of the cross-section (m).

As specified in clause 3.12.3 of the AASHTO LRFD bridge design specification manual, the positive temperature gradients along the depth of concrete and steel girders are presented via Figure (2.8). For negative distributions in concrete and steel superstructures, positive gradients are to be multiplied by -0.3 and -0.2, respectively.

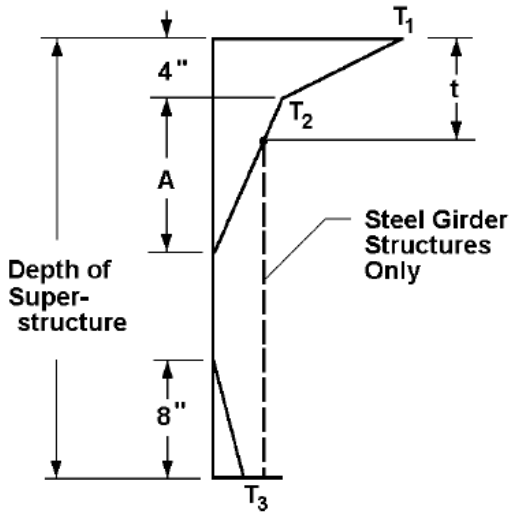

Figure 2.8 Positive thermal gradients in concrete and steel superstructures (AASHTO 2020)

T_1 and T_2 values vary depending on the zone of construction within the United States as shown in Figure (2.9) and highlighted in Table (2.1). For all zones within the US, T_3 is taken as 0^oF in the case a site-specific value is not provided, however, must not exceed 5^oF.

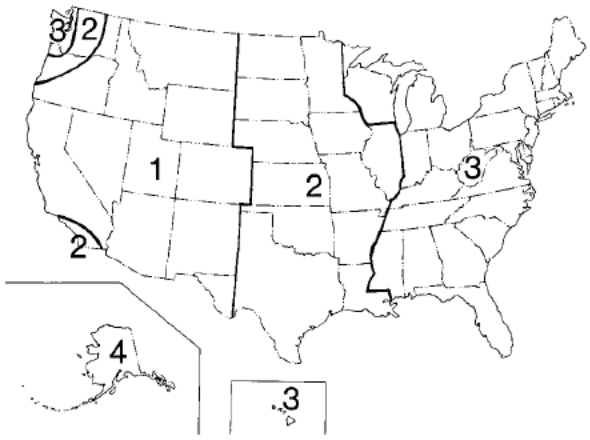

Figure 2.9 Thermal zones in the United States (AASHTO 2020)

Table 2.1 Temperature gradient values (AASHTO 2020)

Zone	T_1 (°F)	T_2 (°F)
1	54	14
2	46	12
3	41	11
4	38	9

For concrete IABs where the depth of the superstructure is greater than or equal to 407 mm (16 in), the dimension *A* in Figure (2.8) is taken as 305 mm (12 in). For concrete superstructures with depths less than 407 mm (16 in), the depth *A* is equal to 102 mm (4 in) less than the actual depth of the superstructure. Finally, IABs utilizing steel girders, the dimension *A* is taken as 305 mm (12 in) and *t* is equal to the depth of the RC deck (AASHTO 2020).

2.3.7 Wind loads

The AASHTO LRFD bridge design manual assumes that winds act on IABs about the horizontal plane, unless otherwise stated. In the absence of measured wind data, the design wind pressure acting on IABs at a wind velocity of 100 mph is expressed via Eq.21:

$$\boldsymbol{P_D = P_B \frac{V_{DZ}^2}{10{,}000}} \quad \textbf{(21)}$$

where P_D is the design wind pressure (ksf), P_B is the base wind pressure acquired from Table (2.2) (ksf), and V_{DZ} is the design wind velocity (mph) at the design elevation given by Eq.22:

$$V_{DZ} = 2.5V_o\left(\frac{V_{30}}{V_B}\right) ln\left(\frac{Z'}{Z_o}\right) \quad (22)$$

where V_{30} is the wind velocity (mph) at 30 ft above the design water table elevation, V_B is the base wind velocity equal to 100 mph, Z' is the height of the bridge subjected to wind above 30 ft of the design water table elevation (ft), V_o is the friction velocity acquired via Table (2.3) (mph), and Z_o is the upstream fetch friction length based on Table (2.3) (ft) (AASHTO 2020).

Table 2.2 Base pressures for various superstructures at base wind velocity equal to 100 mph (AASHTO 2020)

Superstructure component	Windward Load (ksf)	Leeward Load (ksf)
Trusses, Columns, and Arches	0.05	0.025
Beams	0.05	N/A
Large Flat Surfaces	0.04	N/A

Table 2.3 Friction velocity and length values for different upstream surface conditions (AASHTO 2020)

Condition	Open country	Suburban	City
V_o **(mph)**	8.20	10.90	12.00
Z_o **(ft)**	0.23	3.28	8.20

2.3.8 Thermal loads

Under temperature fluctuations, the design thermal movement range for IABs is determined via Eq.23:

$$\Delta_T = \alpha L(T_{Max\ Design} - T_{Min\ Design}) \quad (23)$$

where Δ_T is the design range of thermal expansions and contractions (in), L is the length of the bridge (in), α is the coefficient of thermal expansion depending on the superstructure material (in/in/^{o}F), and $T_{Max/Min}$ are the design maximum and minimum temperatures obtained from Table (2.4) (^{o}F) (AASHTO 2020).

Table 2.4 Design temperature ranges depending on the superstructure material (AASHTO 2020)

Climate	Steel	Concrete	Wood
Moderate	0^o – 120^{o}F	10^o – 80^{o}F	10^o – 75^{o}F
Cold	-30^o – 120^{o}F	0^o – 80^{o}F	0^o – 75^{o}F

2.4 Design and analysis of IAB piles

A uniform design procedure for IAB piles does not currently exist across DOTs within the US. Thus, pile design has been commonly based on engineering intuition and experience. Since longer spanned bridges correspond to larger lateral expansions and contractions, the total lengths of such structures are limited by the lateral capacities of the piles, since applied axial loads further reduce the lateral resisting capabilities of the piles. Thus, efficiently designing piles under combined axial and lateral loads could allow for the construction of longer spanned IABs. The design of IAB piles consists of satisfying three design conditions. First, the structural capacity of the piles to resist axial and flexural stresses under combined axial and lateral effects are checked (Case A). Then, the piles are designed to ensure that the structural member adequately transfers the induced loads onto the surrounding soil (Case B). Finally, the capability of the surrounding soil to resist the induced loads from the bridge piles are checked (Case C) (Abendroth and Greimann 1989).

Case A involves designing piles to ensure adequate resistance is provided against applied axial and flexural stresses. A widely-accepted design approach associated with IAB piles involves idealizing the piles as equivalent beam-columns. As shown in Figure (2.10), the actual pile system supporting the abutments comprises of a length l_u and l corresponding to the length of the pile head above ground level and the pile length embedded in the subgrade soil, respectively. As part of the equivalent beam-column approach, the length l is transformed to an equivalent length where the base of the pile is fixed at a depth l_e below ground level, while l_u remains unchanged. $L^{'}$ is the total length of the equivalent beam-column comprising of l_u and l_e. The factor Δ is the induced lateral displacement at the pile head under abutment expansions and contractions. When applying the equivalent beam-column approach, the first step involves determining the horizontal stiffness parameter k_h of the subgrade soil. This is then followed by the calculation of the equivalent cantilever lengths for horizontal stiffness, bending, and buckling l_e (Abendroth and Greimann 1989). For uniform soil profiles, several methods are found in the literature which approximate the horizontal stiffness parameter k_h of the subgrade soil. Using k_h, the length l_c is first calculated prior to the determination of the equivalent length l_e. This describes the degree of flexibility of the equivalent beam column ranging from flexible to rigid. Accordingly, l_c is calculated via Eq.24:

$$\boldsymbol{l_c = 4\sqrt[4]{\frac{EI}{k_h}}} \tag{24}$$

where E is the elastic modulus of the pile (kPa), I is the moment of inertia of the pile oriented in the direction of lateral bending (m^4), and k_h is the horizontal stiffness of the soil

(kN/m). Subsequently, by utilizing Figures (2.11) and (2.12), the equivalent lengths l_e for horizontal stiffness, bending and buckling for fixed and pinned pile head conditions, respectively, are determined (Abendroth and Greimann 1989).

For non-uniform soil profiles, an equivalent soil stiffness k_e corresponding to the existing soil layers is utilized in Eq.24 to determine an appropriate value for l_c. For the same soil displacement, the work done by the existing soil profile and the work done by the equivalent soil system to provide lateral resistance are equated via Eq.25:

$$\int_o^{l_o} \frac{k_h(z)y^2}{2}\,dz = \int_o^{l_o} \frac{k_e y^2}{2}\,dz \tag{25}$$

where $k_h(z)$ is the horizontal soil stiffness (kN/m) at depth z, k_e equivalent soil stiffness (kN/m), l_o is the active length of the pile in bending (m), and y is the displacement shape function of the pile. The active length of pile in bending l_o and displacement shape function y are given by Eq.26 and Eq.27, respectively:

$$l_o = \frac{l_c}{2} \tag{26}$$

$$y = \Delta_g \left(1 - \frac{z_1}{l_o}\right) \tag{27}$$

where Δ_g is the lateral displacement at the base of the abutment (m) and z_1 is the depth of soil below the abutment (m). Thus, by substituting Eq.27 into Eq.25, the equivalent horizontal soil stiffness for a non-uniform soil profile k_e is determined via Eq.28:

$$\boldsymbol{k_e = \frac{3}{l_o^3} \int_o^{l_o} k_h(z)\,(l_o - z_1)^2\,dz} \quad \textbf{(28)}$$

where k_e is the equivalent horizontal soil stiffness for a non-uniform soil profile (kN/m), l_o is the active length of pile in bending (m), $k_h(z)$ is the horizontal soil stiffness (kN/m) at depth z, and z_1 is the depth of soil beneath the base of the abutment (m). Accordingly, after iterating Eqs.24-28, the equivalent cantilever lengths for horizontal stiffness, bending, and buckling l_e are then obtained by via Figures (2.11) and (2.12) for fixed and pinned pile head conditions, respectively (Abendroth and Greimann 1989).

Then, based on methods described in the AASHTO LRFD bridge design specification manual (AASHTO 2020), the allowable axial and bending stresses F_a and F_b, respectively, and the elastic buckling stress F_e of the pile are calculated.

Subsequently, the total applied axial stress on the piles are calculated via Eq.29:

$$\boldsymbol{f_a = \frac{P_w + P_T}{A}} \quad \textbf{(29)}$$

where f_a is the total applied axial stress on the piles (kPa), P_w is the applied axial force due to the superstructure (kN), P_T is the applied axial force due to thermal contractions and expansions (kN), and A is the cross-sectional area of the pile (m^2).

This is then followed by calculating the bending stress acting on the piles due to the combined axial and lateral loadings. Abendroth and Greimann (Abendroth and Greimann 1989) provided two design alternatives to determine the bending stresses acting on the piles supporting IABs. Alternative 1 is an elastic design approach which disregards the pile's capability of internally redistributing induced stresses by forming plastic hinges. Thus,

when utilizing design alternative 1, the bending stress acting on the pile is determined via Eq.30:

$$\boldsymbol{f_b = \frac{M_T + M_w}{S'}} \quad \textbf{(30)}$$

where M_T is the applied moment due to thermally induced displacements (kN.m), M_w is the applied moment due to the pile head rotation under superstructure dead load (kN.m), and S' is the section modulus of the pile (m^3). The factor M_w is calculated via Eq.31:

$$\boldsymbol{M_w = \left[\frac{4EI}{L_{eM}}\right] \theta_w} \quad \textbf{(31)}$$

where E is the elastic modulus of the pile (kPa), I is the moment of inertia about the plane of lateral bending (m^4), L_{eM} is the equivalent cantilever length for bending (m), and θ_w is the pile rotation (rad). For alternative 1, the induced moment under thermal displacements M_T is calculated via Eq.32:

$$\boldsymbol{M_T = \frac{D_1 EI\Delta}{L_{eM}^2}} \quad \textbf{(32)}$$

where D_1 is equal to 6 or 3 for a fixed or pinned head pile condition, respectively, E is the elastic modulus of the pile (kPa), I is the moment of inertia about the plane of lateral bending (m^4), L_{eM} is the equivalent cantilever length for bending (m), and Δ is the design lateral movement (m) under design temperature changes.

After calculating the bending stresses acting on the pile, it is required to satisfy the strength and stability interaction criteria under applied axial and bending stresses. The stability of the pile is checked via the following equation Eq.33:

$$\frac{f_a}{F_a} + \frac{C_m f_b}{\left[1 - \frac{f_a}{F_e}\right] F_b} \leq 1 \quad \textbf{(33)}$$

where f_a is the total applied axial stress (kPa), f_b is the total applied bending stress (kPa), F_a is the allowable axial stress (kPa), F_b is the allowable bending stress (kPa), F_e is the elastic buckling stress (kPa), and C_m is the moment gradient factor. Similarly, the strength of the pile is checked via Eq.34:

$$\frac{f_a}{0.472 F_y FS} + \frac{f_b}{F_b} \leq 1 \quad \textbf{(34)}$$

where f_a is the total applied axial stress (kPa), f_b is the total applied bending stress (kPa), F_y is the yield strength of the pile material (kPa), F_b is the allowable bending stress (kPa), and FS is the factor of safety accounting for an allowable axial stress increase as per the AASHTO design manual (AASHTO 2020; Abendroth and Greimann 1989).

However, unlike alternative 1, alternative 2 is an inelastic design approach which assumes that piles provide adequate ductility such that stresses are redistributed through the formation of plastic hinges. Provided that the pile provides sufficient ductility to accommodate induced lateral strains, the ultimate strength of the pile is unaffected by the lateral expansions and contractions of the abutment. Thus, the total bending stress acting on the pile via alternative 2 is given by Eq.35:

$$\boldsymbol{M = \frac{M_s + M_w}{S}} \quad \textbf{(35)}$$

where M_s is the induced second order moment (kN.m), M_w is the applied moment due to the pile head rotation under superstructure dead load (kN.m), and S is the section modulus of the pile (m^3). The induced second order moment M_s corresponds to the product of the total axial force ($P_w + P_T$) acting on the pile and the lateral displacement due to temperature rises and drops. This is calculated using Eq.36:

$$\boldsymbol{M_s = D_2 P \Delta} \quad \textbf{(36)}$$

where D_2 is equal to 0.5 or 1 for a fixed or pinned pile head condition, respectively, P is the total axial force due to thermal contractions and expansions and superstructure dead load (kN), and Δ is the design lateral movement under temperature fluctuations (m).

The stability and strength interaction criteria associated with alternative 2 are the same as those mentioned when utilizing alternative 1. However, since this alternative is an inelastic based approach, additional ductility criteria are considered. To ensure that the designed piles provide adequate ductility against induced thermal displacements, Eq.37 must be satisfied:

$$\Delta \leq \Delta_i \quad \textbf{(37)}$$

where Δ_i is the allowable lateral displacement at the pile head (m) and Δ is the design lateral movement under design maximum and minimum temperatures (m). The pile's lateral displacement capacity Δ_i is expressed via Eq.38:

$$\Delta_i = \Delta_b(D_3 + 2.25C_i) \tag{38}$$

where Δ_b is the pile head lateral displacement at which the actual extreme fiber bending stress equals the allowable bending stress of the pile (m), D_3 is equal to 0.6 or 1 for fixed or pinned pile head conditions, respectively, and C_i is the inelastic rotation capacity reduction factor. Δ_b is given by Eq.39:

$$\Delta_b = \frac{F_b S L_{eM}^2}{D_1 E I} \tag{39}$$

where F_b is the allowable bending stress (kPa), S is the section modulus of the pile (m^3), L_{eM} is the equivalent cantilever length for bending (m), D_1 is equal to 6 or 3 for a fixed or pinned head pile condition, respectively, E is the elastic modulus of the pile (kPa), and I is the moment of inertia about the plane of lateral bending (m^4). Similarly, C_i is expressed via Eq.40:

$$C_i = \frac{19}{6} - \frac{b_f\sqrt{F_y}}{60t_f} \tag{40}$$

where b_f is the flange width of the pile (m), t_f is the thickness of the pile flange (m), and F_y is the yield strength of the pile material (kPa) (Abendroth and Greimann 1989).

After structurally designing the piles (case A), their capacity to transfer loads onto the surrounding soil must be checked (case B). As seen in Figure (2.10), the length of the pile below the ground surface is divided into two components. l_n is the length of the pile where skin resistance is nonexistent and l' is the remaining effective length of the pile. As indicated by Abendroth et al. (Abendroth et al. 1989), the skin resistance provided by the pile along the length l' is unaffected by the induced lateral displacements, given that the magnitude of y_{max} at a depth l_n does not exceed 2% of pile dimension oriented about the plane of bending. Firstly, given y_{max}, l_u, and l_c, the factor l_n is determined utilizing Figures (2.13) and (2.14) for fixed and pinned pile head conditions, respectively. Then, the corresponding skin resistance provided by the pile along the length l' is calculated. Thus, case B is satisfied given that skin resistance provided by the pile is greater than or equal to the total applied axial force.

The final design step consists of ensuring that the surrounding soil provides adequate resistance against the transferred loads from the piles (case C). According to studies conducted by Abendroth and Greimann (Abendroth and Greimann 1989), the lateral movement of the bridge piles do not influence the resisting capabilities of the surrounding soil. In addition, this criterion is typically satisfied given that pile spacing is greater than the pile dimension by a factor of 3.

Since IAB piles are subjected to combined lateral and axial loads, their design and analysis are based of empirical and finite element (FE) methods. These methods are based upon data acquired from full-scale tests conducted on laterally and axially loaded piles. Research conducted by Greimann et al. (Greimann et al. 1986) provided the specifics associated with the analysis of IABs under induced thermal effects utilized in current state-of-the-art

practices. Using structural FE software packages, the complex soil-structure interactions of IABs under induced cyclic thermal loadings are analyzed via the beam-column concept as shown in Figure (2.15). In these models, structural components such as abutments, piles, approach slabs, deck, and girders are modelled as finite elastic beam elements discretized at *n* intervals. These elements are formulated by the tangent stiffness matrix given by Eq.41:

$$\Delta \boldsymbol{F_j^{i+1}} = \left[\boldsymbol{K_j^i}\right]_{\boldsymbol{T}} \Delta \boldsymbol{D_j^{i+1}} \tag{41}$$

where ΔF_j^{i+1} is the applied load vector at step *i + 1*, $\left[K_j^i\right]_T$ is the tangential stiffness matrix comprised of conventional and geometric matrices during the previous step *i*, and ΔD_j^{i+1} is the nodal displacement at step *i + 1* increments.

In this analysis approach, the soil medium is idealized via discrete one-dimensional linear/non-linear winkler springs. These soil springs are connected horizontally and vertically via node endings at each interval along the length of the beam element. The soil-structure interaction of the soil medium is defined through three stress-strain nodal relationships comprising of *p-y*, *f-z*, and *q-z* curves. The *p-y* stress-strain relationship characterizes the soil pressure acting on the pile about the lateral direction and the corresponding pile displacement. Similarly, the *f-z* stress-strain relationship represents the vertical skin resistance of the soil and the corresponding pile displacements in the vertical direction. The bearing stress at the pile toe and the corresponding settlements is described through *q-z* stress-strain relationships (Greimann et al. 1986).

This FE analysis approach is commonly used by DOTs worldwide to design and analyze IABs due to its simplicity and rapid computational times. However, the assumptions and shortcomings associated with this method must be understood. Firstly, by using the beam-column approach, the generation of torsional stresses during soil-structure interactions are neglected. Moreover, the deformation and stress paths of the defined springs in the horizontal and vertical directions are independent, thus giving rise to discontinuities. Furthermore, about the two orthogonal lateral planes, soil deformations are independent (Greimann et al. 1986). Finally, employing skeletal soil springs prevents the simulation of essential geotechnical properties such as groundwater conditions, drainage, and internal stress paths and histories (Dhadse et al. 2020).

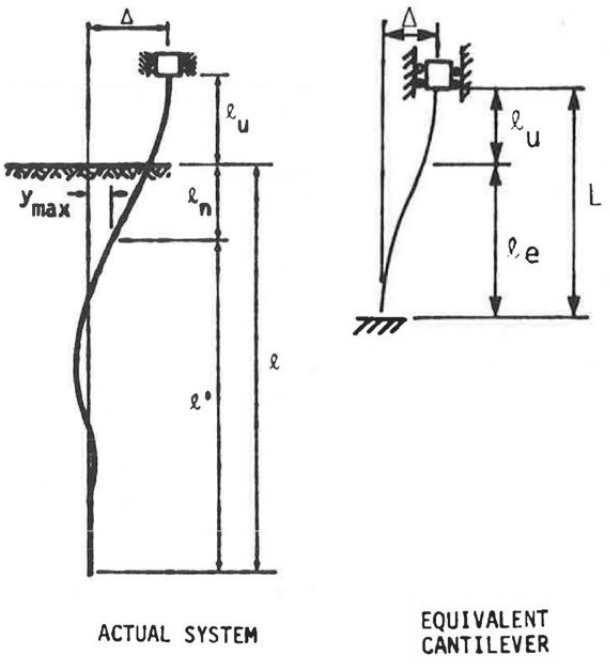

Figure 2.10 Idealized equivalent beam-column cantilever pile system (Abendroth and Greimann 1989)

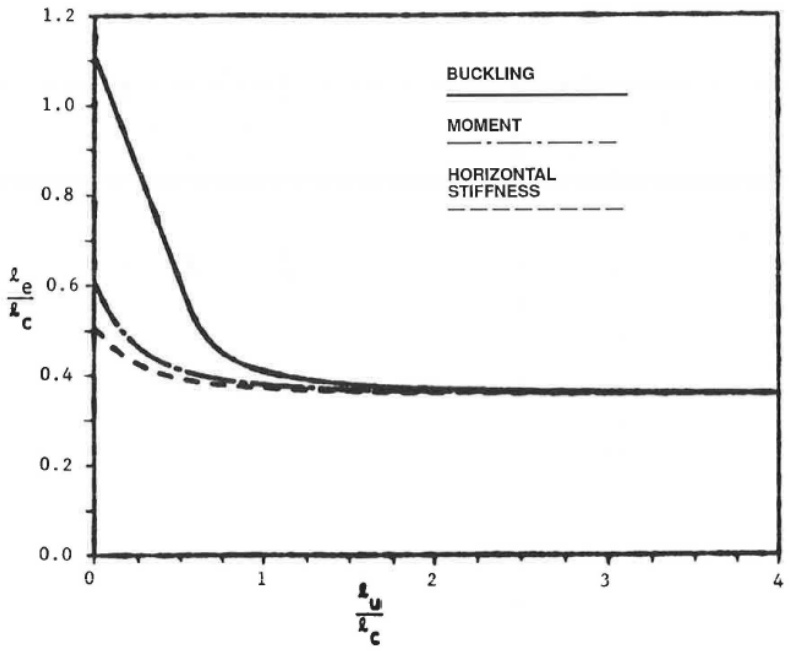

Figure 2.11 Equivalent cantilever lengths for fixed pile head conditions (Abendroth et al. 1989)

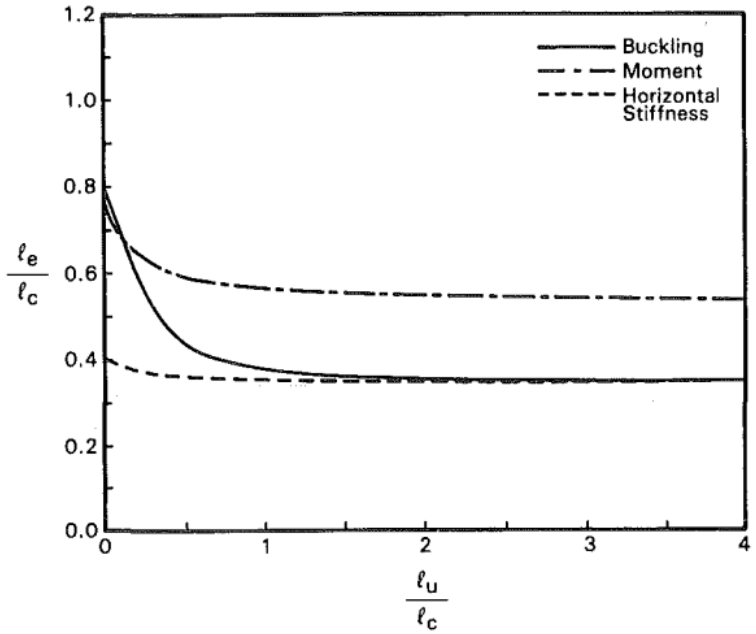

Figure 2.12 Equivalent cantilever lengths for pinned pile head conditions (Abendroth et al. 1989)

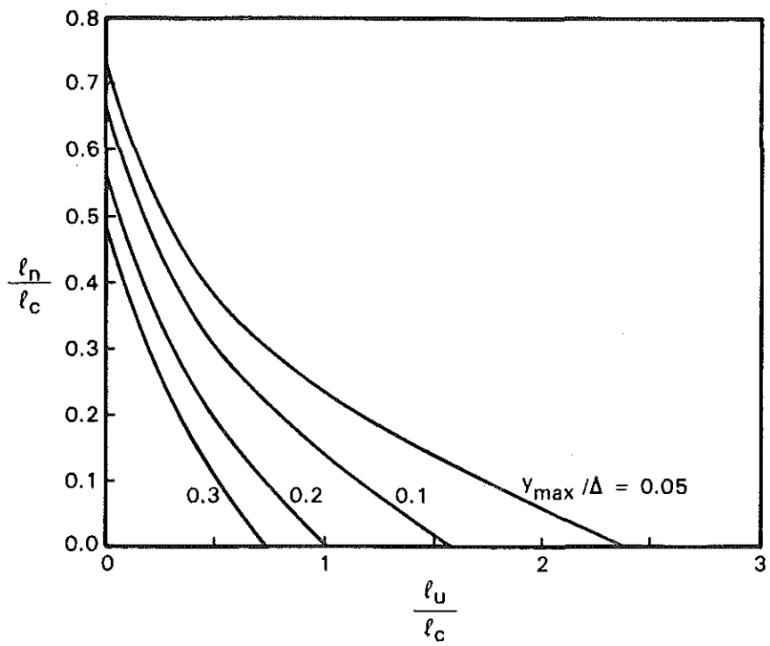

Figure 2.13 Displacement of embedded pile in uniform soil for fixed head conditions (Abendroth et al. 1989)

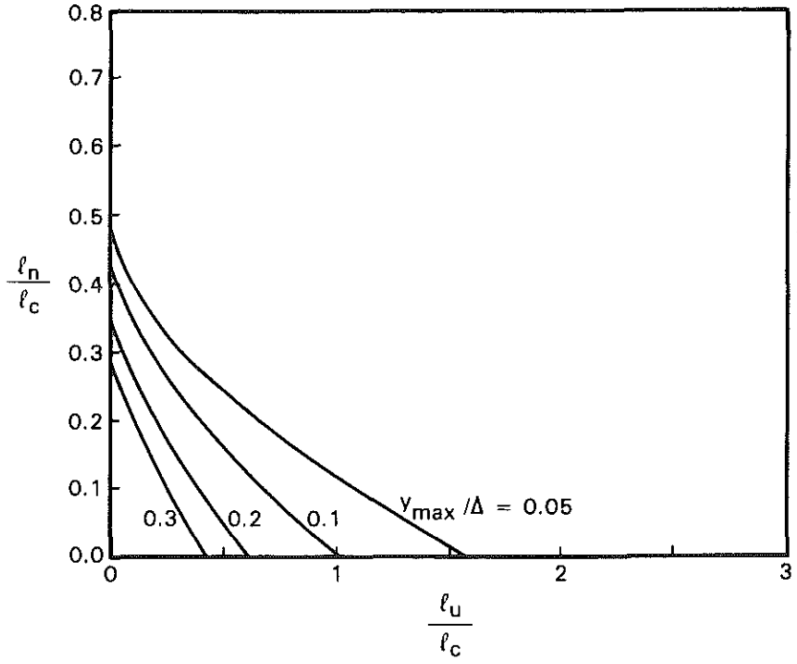

Figure 2.14 Displacement of embedded pile in uniform soil for pinned head conditions (Abendroth et al. 1989)

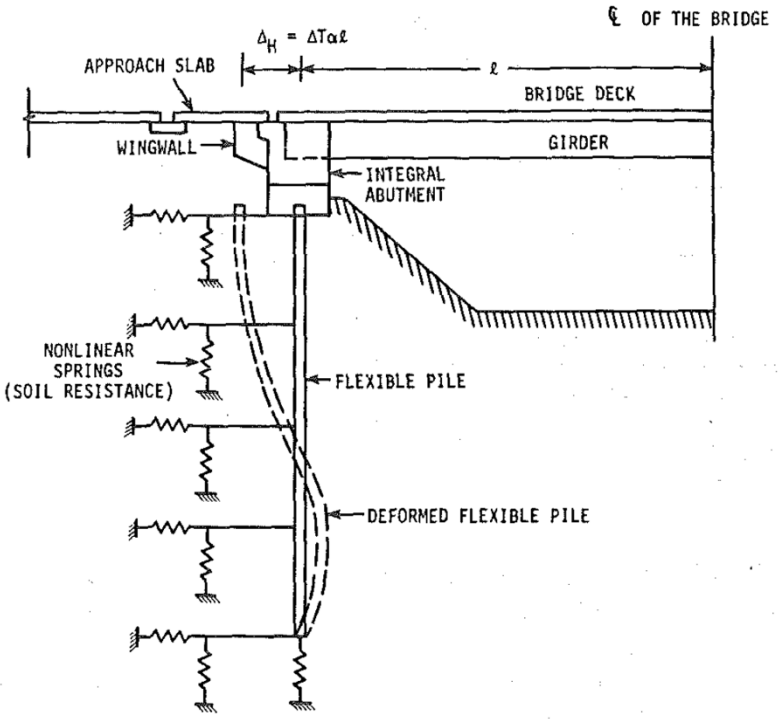

Figure 2.15 Finite element analysis of an IAB (Greimann et al. 1986)

2.5 Design practices and guidelines

Over the years, the use of IABs rapidly grew in popularity due to their desirable economical and structural attributes compared to conventional jointed bridges (Kunin and Alampalli 2000; Sigdel et al. 2021; White II et al. 2010). This was indicated via a survey conducted by Kunin and Alampalli (Kunin and Alampalli 2000), which investigated current practices associated with IABs across Canada and the US. Following the survey, it was found that by the year 1996, over 9,000 IABs were built across Canada and the US as shown in Figure (2.16).

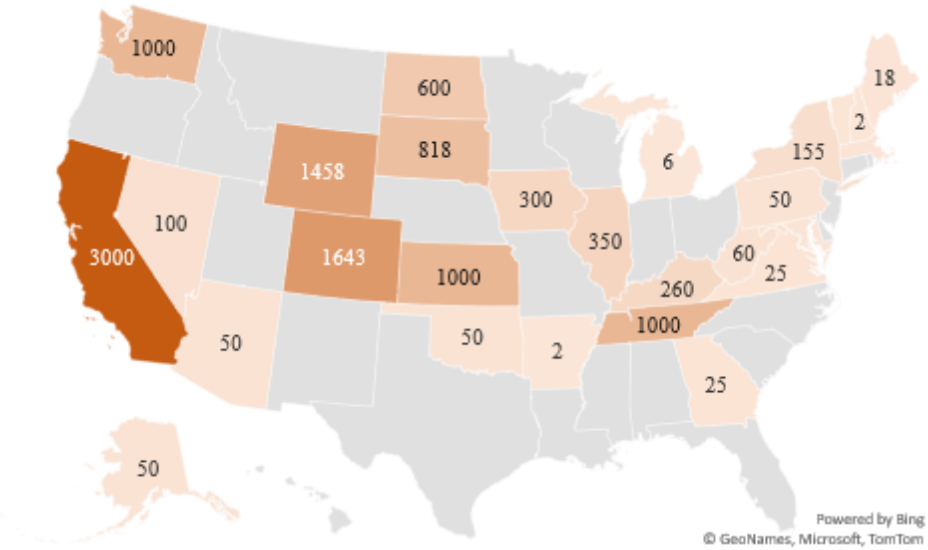

Figure 2.16 IAB construction by numbers within various states in the US by the year 1996 (Kunin and Alampalli 2000)

Thus, due to the recent introduction of IABs, design and construction guidelines related to such structures is not currently addressed. It was seen that design limits and construction recommendations have been specified based on engineering intuition and experience (Frosch and Lovell 2011). By exploring invoked IAB design guidelines worldwide, practices across North America, Europe, Asia, and Australia and New Zealand were seen to vary (Kunin and Alampalli 20005; Sigdel et al. 2021; Tabatabai et al. 2017; White II et al. 2010).

2.5.1 Maximum length limits

Maximum allowable IAB lengths were seen to differ between various states across the US for steel and concrete structures. As indicated by a survey conducted by Tabatabai et al. (Tabatabai et al. 2017), maximum lengths for concrete bridges were seen to be greater than

or equal to steel IABs as shown in Figure (2.17). For concrete and steel structures, the average maximum lengths were seen to be 147 m and 107.5 m, respectively.

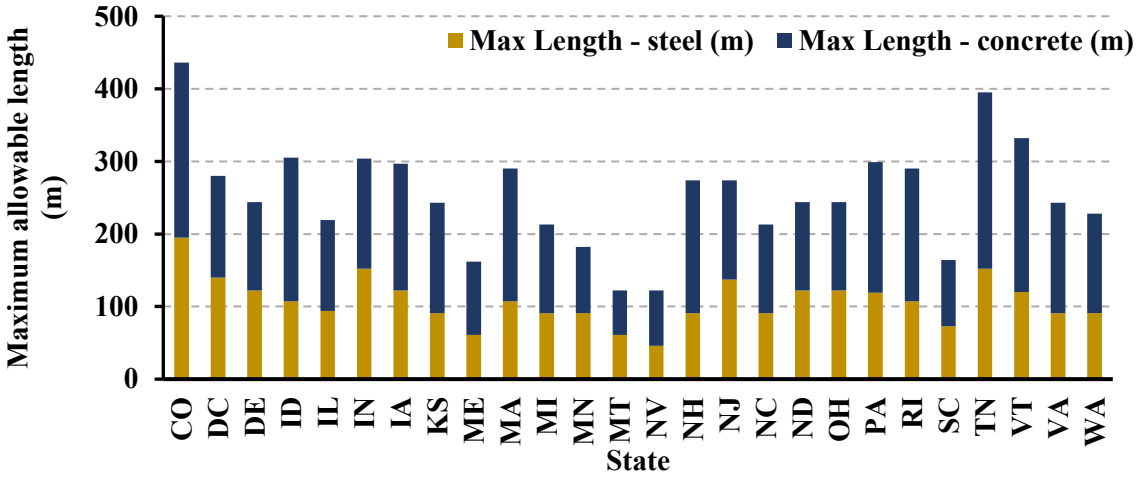

Figure 2.17 Maximum allowable IAB length for concrete and steel structures (Tabatabai et al. 2017)

Figure (2.18) compares the maximum allowable lengths for IABs in various countries worldwide (AASHTO 2020; CSA 2014; Kaufmann and Alvarez 2011; New Zealand Transport Agency 2013; Roads and Traffic Authority 2007; Sigdel et al. 2021; Tabatabai et al. 2017; White II et al. 2010). As shown in the plotted figure, the maximum allowable lengths of IABs across Europe were relatively similar, except for Sweden. The maximum lengths invoked in Canada and the US are considerably larger than those specified in Europe, Asia, and Australia/New Zealand.

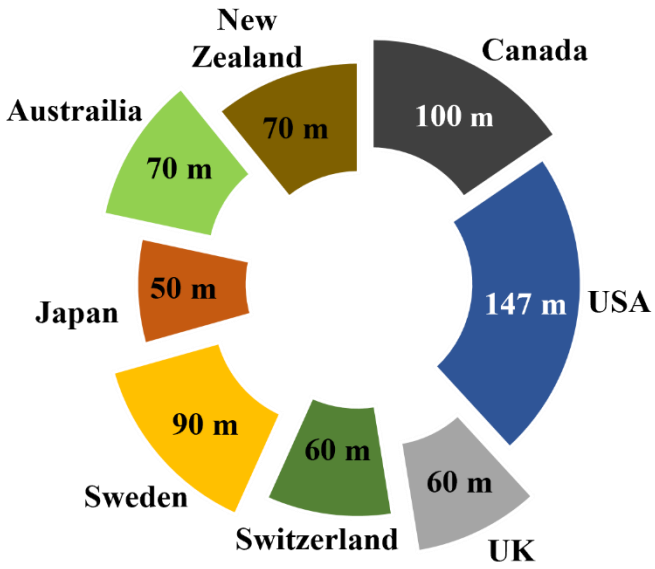

Figure 2.18 Maximum allowable limits on length within various regions worldwide (AASHTO 2020; CSA 2014; Kaufmann and Alvarez 2011; New Zealand Transport Agency 2013; Roads and Traffic Authority 2007; Sigdel et al. 2021; Tabatabai et al. 2017; White II et al. 2010)

2.5.2 Maximum skew limits

Figure (2.19) presents the maximum skew limitations for continuous bridges in the US, based on bridge design manuals across each state and surveys conducted by Tabatabai et al. (Tabatabai et al. 2017) and Sigdel et al. (Sigdel et al. 2021). As shown in the map, most states utilize IABs with skew angles less than or equal to 30°. From the 39 states which limit the degree of skew, 61% have adopted a maximum skew angle of 30° for IABs. In the state of Idaho, the DOT has specified that for IABs with a skew angle exceeding 25°, effects corresponding to skew must be considered during design.

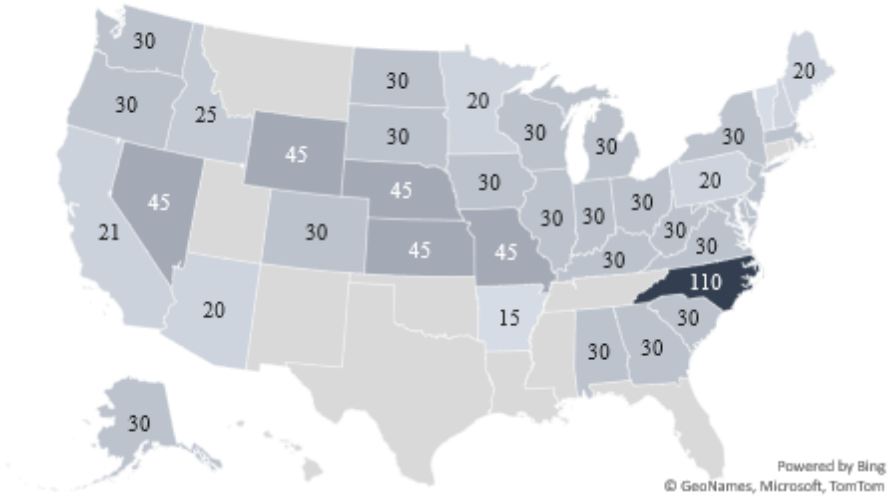

Figure 2.19 Maximum allowable skew angles for IABs within the US (AASHTO 2020 and corresponding state DOT design manuals)

Figure (2.20) compares the maximum allowable skew angles for IABs in various regions worldwide. With most European practices limiting the degree of skew to a maximum value of 30º, countries such as Sweden, Germany, and Switzerland have not specified limits of skew (Kaufmann and Alvarez 2011; White II et al. 2010). Unlike, the US, Canadian DOTs utilize IABs with a maximum skew angle of 20º. According to Australian guidelines, IABs with maximum lengths less than or equal to 50 m are restricted to a maximum skew angle of 30º. However, bridge lengths ranging between 50 m and 70 m are limited to a skew angle of 20º (Roads and Traffic Authority 2007). Similarly, the bridge design manual set by New Zealand specifies that the maximum allowable skew angle is 30º, provided that the maximum lengths of concrete and steel structures do not exceed 70 m and 55 m, respectively (New Zealand Transport Agency 2013). Since IAB construction in Japan is not yet fully adopted, current practices only utilize straight bridges (Sigdel et al. 2021).

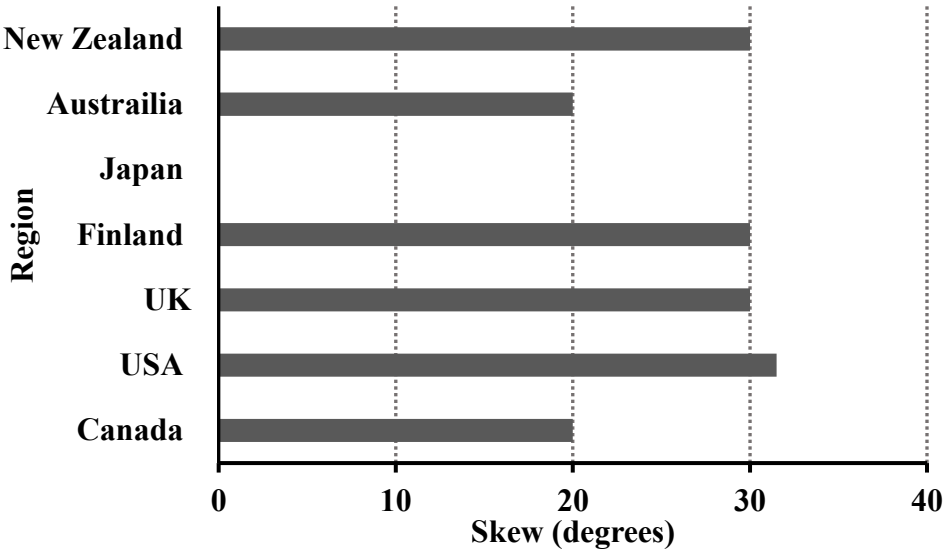

Figure 2.20 Maximum allowable limits on skew angle within various regions worldwide (AASHTO 2020; CSA 2014; New Zealand Transport Agency 2013; Roads and Traffic Authority 2007; Sigdel et al. 2021; Tabatabai et al. 2017; White II et al. 2010)

2.5.3 Maximum and minimum design temperatures

Figure (2.21) presents the various design minimum and maximum temperatures specified by the AASHTO and DOT bridge design manuals across the US for concrete and steel structures (AASHTO 2020 and corresponding state DOT design manuals). By looking at Figure (2.21a), most states specify a maximum temperature of 80°F for concrete structures, except for Illinois and Minnesota, which utilize maximum temperatures of 130°F and 120°F, respectively. Similarly, for concrete structures, the minimum temperatures specified by the DOTs range between 0°F and 10°F, except for Illinois and Minnesota, which utilize minimum temperatures of -30°F as shown in Figure (2.21c). The maximum design temperatures for steel IABs for various states within the US are shown in Figure (2.21b). It can be seen that the average design temperature specified by DOTs is 120°F, which is

larger than the design temperature for concrete structures by 40°F. Figure (2.21d) shows the range of minimum design temperatures utilized for steel structures. By looking at Figure (2.21d), a wider range of minimum design temperatures are associated with steel structures, varying from -30°F to 10°F.

Figure (2.22a) compares the design changes in temperatures corresponding to the contraction and expansion of concrete structures specified by various regions worldwide. It can be seen that the temperature changes specified by New Zealand and Switzerland are identical. The US utilizes the widest range of temperature changes, with a difference of 57°F in magnitude. However, during design, Canada specifies the smallest temperature change for concrete structures with a magnitude of approximately 15°F.

For steel structures, Figure (2.22b) shows the changes in temperatures specified across North America, Europe, and New Zealand. As seen in the plotted figure, Switzerland and New Zealand follow the same range of thermal drops and rises during design. Similar to concrete IABs, the US and Canada utilize the widest and shortest thermal fluctuations, respectively (AASHTO 2020; CSA 2014; Kaufmann and Alvarez 2011; New Zealand Transport Agency 2013).

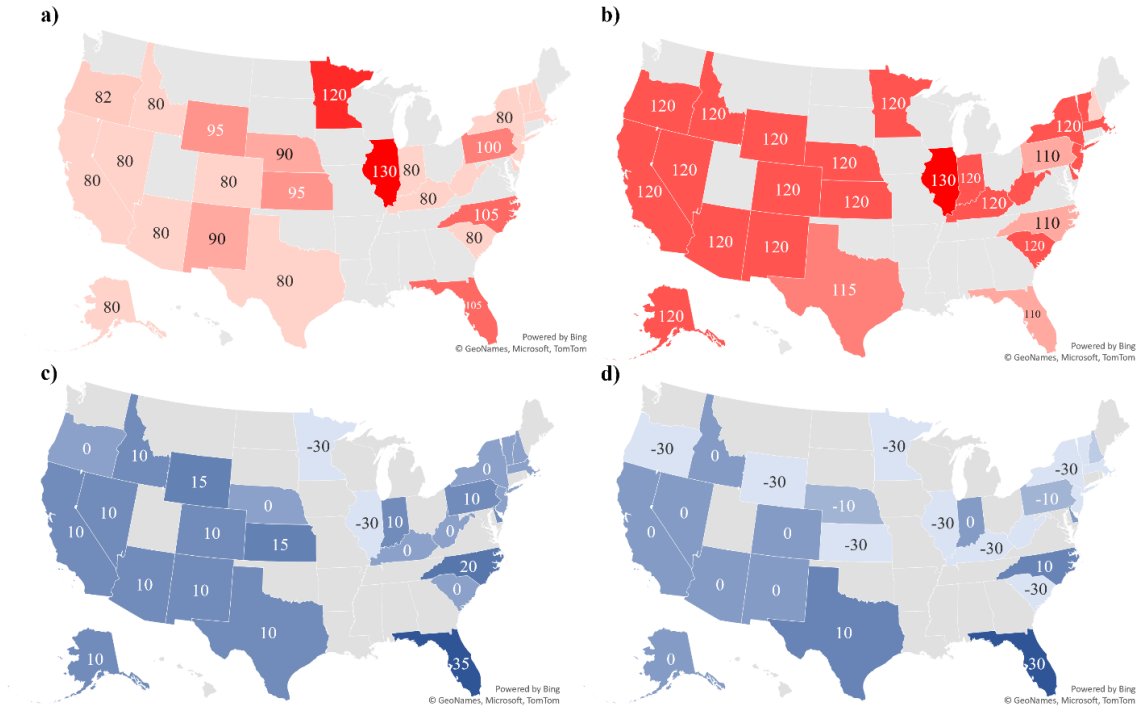

Figure 2.21 Design maximum temperatures for concrete structures; **(b)** Design maximum temperatures for steel structures; **(c)** Design minimum temperatures for concrete structures; and **(d)** Design minimum temperatures for steel structures (AASHTO 2020 and corresponding state DOT design manuals)

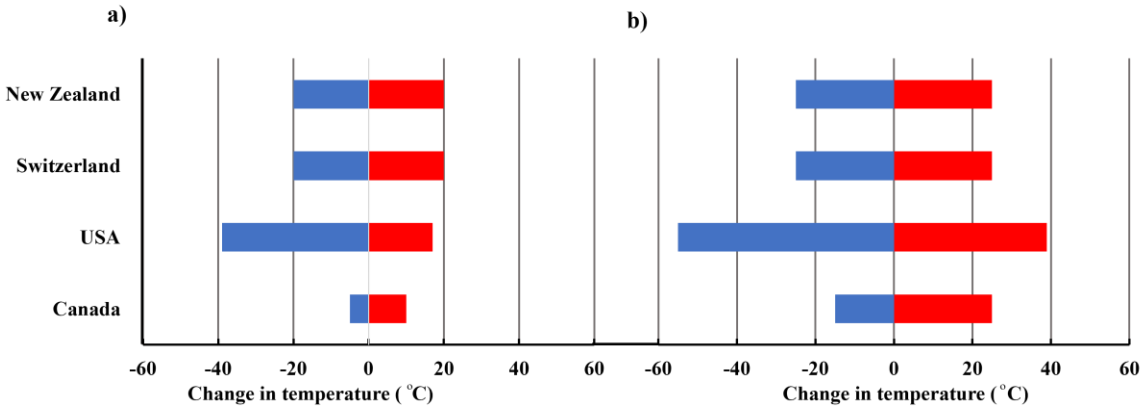

Figure 2.22 Design temperature changes worldwide for: **(a)** concrete structures and **(b)** steel structures (AASHTO 2020; CSA 2014; Kaufmann and Alvarez 2011; New Zealand Transport Agency 2013)

2.5.4 Pile type, orientation, and embedment length

Figure (2.23) plots the various pile types utilized across the US when constructing the substructures of IABs according to a survey conducted by Tabatabi et al. (Tabatabai et al. 2017). As shown in the plotted figure, the four pile types utilized in the US comprise of steel HP piles, hollow steel tubes (HST), concrete filled steel tubes (CFT), and prestressed concrete piles (PCP). Furthermore, it is clear that steel HP piles are the popular option for supporting integral abutments, with 30 states using such piles. However, with only 4 states employing PCPs, this pile type is the least favorable choice to support integral abutments.

Figure (2.24) presents the various pile orientations utilized by DOTs across the US. By looking at the plotted figure, 57% out of the 37 states which consider IAB construction orient piles about the weak axis of bending to reduce the generated internal stresses, which correspond to induced thermal displacements. In addition to the 5 states which recommend strong axis orientation, it was found that the orientation of piles in 14% of the states were based on the designer's judgement and preference (Soltani and Kukreti 1992).

Figure (2.25) plots the various pile embedment lengths for three length ranges of 0.28 m – 0.3 m (low), 0.46 m – 0.61 m (medium), and 0.76 m – 0.91 m (high) across the US. As seen in the plotted figure, the number of states which utilize low, medium, and high embedment lengths are 7, 18, and 3, respectively. Thus, common practices indicate that embedding the piles approximately 0.46 m – 0.61 m into the abutment is recommended (Soltani and Kukreti 1992).

Finally, research conducted by White II et al. (White II et al. 2010) compared the types of piles used to support bridge abutments based on North American and European practices as shown in Figure (2.26). In addition to the common practice within North America to

utilize HP piles, it was found that within Europe, England and Ireland also employ HP piles during IAB construction. Furthermore, similar to North American practices, CFTs were utilized during the construction of IAB substructures in Finland. However, unlike North American guidelines, precast and prestressed concrete (PCP) piles were uncommon within Europe. White II et al. (White II et al. 2010) found that such piles were only used to construct IABs in Sweden. Similar to PCPs, the use of X – piles within Europe and North America is uncommon, with the exception of Swedish IABs. Moreover, it was found that reinforced concrete piles are common practice within Germany, since these piles reduce the moments at the mid-span of the bridge and restraint the abutments against rotation. Finally, as indicated by White II et al. (White II et al. 2010) and Caristo et al. (Caristo et al. 2018), IABs constructed within the UK commonly utilize a spread footing foundation supporting full height RC abutments.

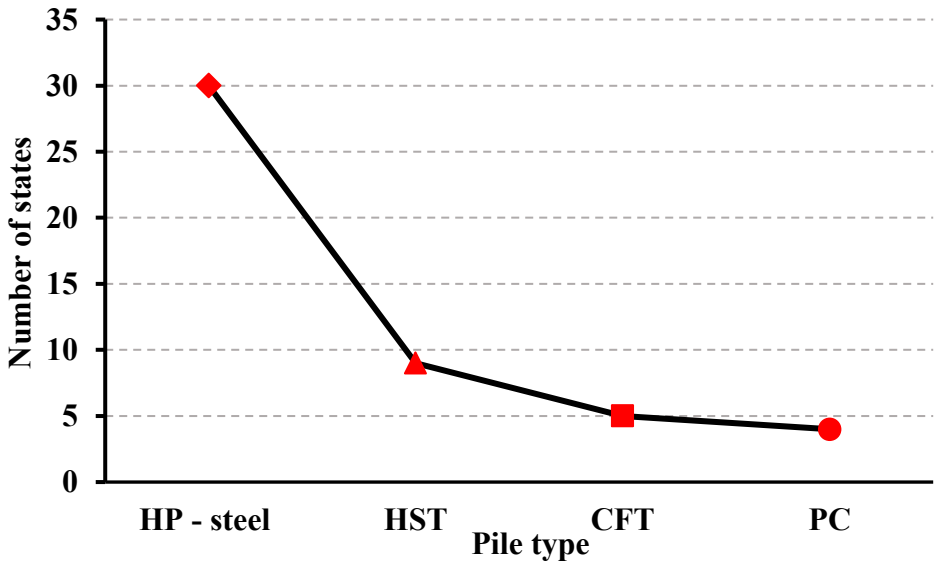

Figure 2.23 Utilization of various pile types within the US (Tabatabai et al. 2017)

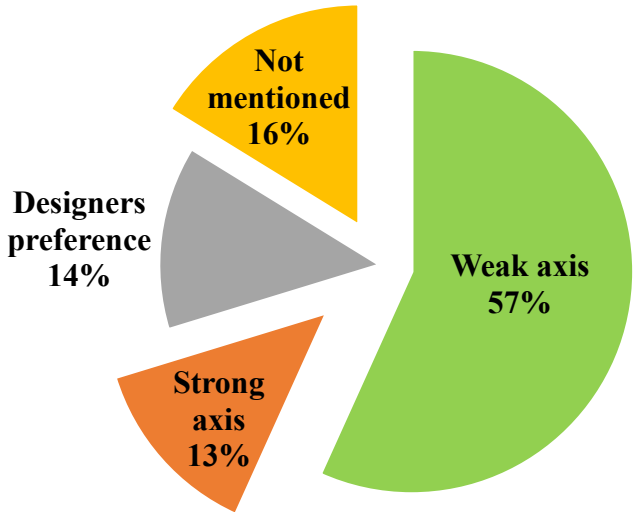

Figure 2.24 IAB pile orientations across the US (Tabatabai et al. 2017)

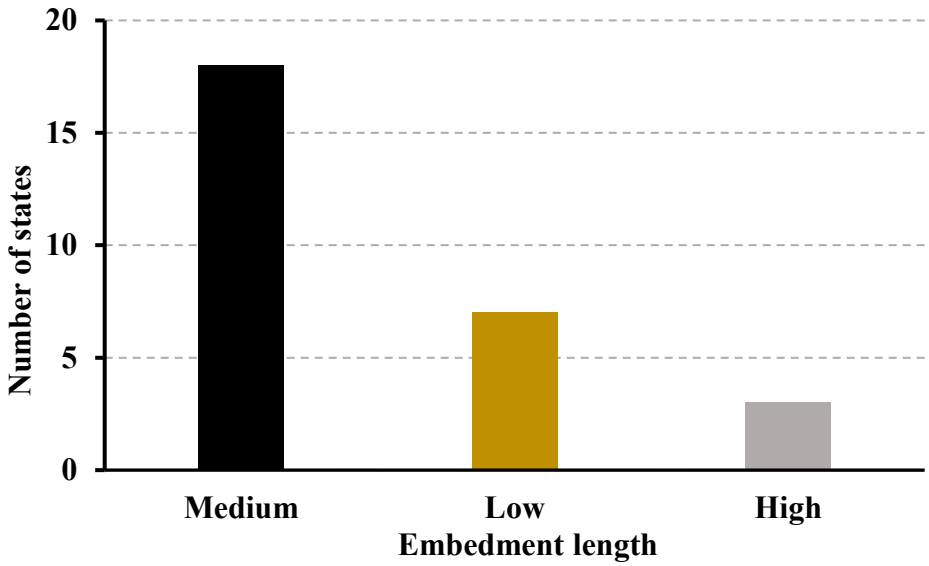

Figure 2.25 IAB pile embedment lengths across the United States (Tabatabai et al. 2017)

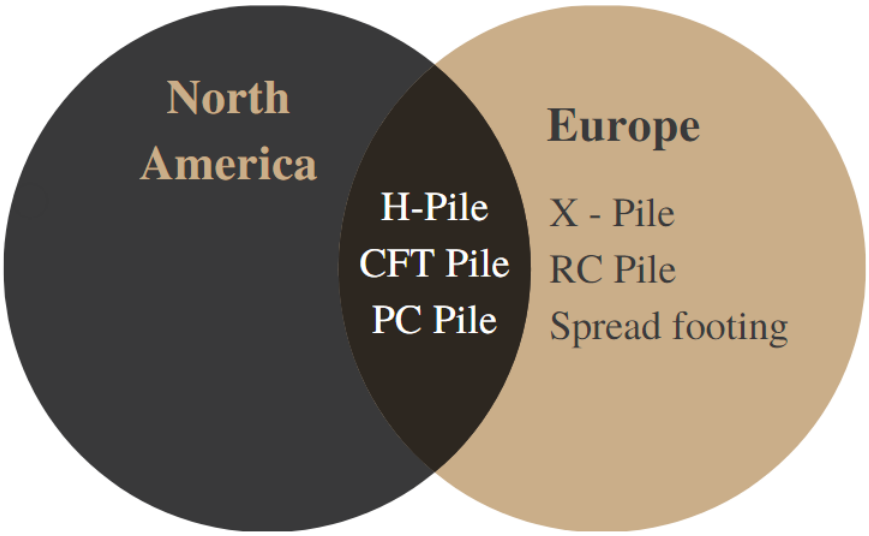

Figure 2.26 Different pile types utilized by North America and European practices (White II et al. 2010)

2.5 Conclusions

This paper first discussed the background of IABs and the corresponding attributes and shortcomings based on research found in the literature. This was then followed by describing the primary and secondary loads which act on IABs, along with various evaluation methods used during the design process. Details on the design and finite element analysis methods of IAB piles based on current practices were then presented and discussed. Then, IAB design guidelines and criteria within North America, Europe, Asia, Australia, New Zealand were compared where limits on length, skew angle, and pile type and orientation were highlighted. Based on the conducted research presented in this paper, the following conclusions can be drawn:

1. IABs significantly reduce maintenance costs related to expansion and bearing joints. Studies have shown that expansion and bearing joint rehabilitation were estimated to

cost around $300,000. Furthermore, costs related to the rehabilitation of deteriorated bridges were seen to exceed $ 2.5 billion.

2. The design of passive earth pressure distributions behind the abutment back wall via theoretical methods could lead to conservative predictions. Thus, numerically analyzing earth pressure distributions using the finite element method correlates to realistic deformations. Hence, bridge components such as abutments and piles can be designed more efficiently.
3. Analyzing IAB piles via the beam-column approach gives rise to discontinuities, and thus unrealistically modelling the complex soil-structure interactions that occur under the applied loads. Furthermore, since the subgrade soil is idealized as skeletal springs, this prevents the simulation of pore water pressures, stress paths and histories, drainage, and the relative deformation between the piles and the surrounding soil. However, modelling the structural and soil elements as a continuum with corresponding interfaces would realistically simulate soil-structure interactions, thus resulting in more efficient designs.
4. A comprehensive and uniform design guideline for IABs does not currently exist since the specified criteria were seen to vary across the US and around the world. Thus, extensive research is required to develop a unified design procedure to enhance the performance and efficiency of IABs.
5. Since most of the DOTs around the world limit the skew angles of IABs to approximately 30^{o}, research is required to further investigate the effects of high skew angles on the performance of the superstructure and substructure components.

6. Knowledge gap exists in understanding the impacts of curved IABs. Thus, by further expanding current knowledge on curved IAB, this will allow engineering practitioners and DOTs worldwide to extend on IAB applications and enhance the efficiency and performance of such structures.

References

AASHTO (2020). *LRFD Bridge Design Specifications*, 9th ed. American Association of State Highway and Transportation Officials, Washington, D.C.

Abendroth, R.E., Greimann, L.F., Ebner, P.B., (1989). Abutment Pile Design for Jointless Bridges. *Journal of Structural Engineering*, 115(11), 2914-2929. https://doi.org/10.1061/(ASCE)0733-9445(1989)115:11(2914)

Abendroth, R.E. and Greimann, L.F., (1989). Rational Design Approach for Integral Abutment Bridge Piles. *Transportation Record 1223*.

Alaska Department of Transportation (2017). *Alaska Bridges and Structures Manual*, Highway Division, Alaska Department of Transportation: Juneau, AK, USA.

Arockiasamy, M., Butrieng, N., Sivakumar, M., (2004). State-of-the-Art of Integral Abutment Bridges: Design and Practice. *Journal of Bridge Engineering*, 9(5), 497-506. https://doi.org/10.1061/(ASCE)1084-0702(2004)9:5(497)

Arsoy, S., Barker, R. M. & Duncan, J. M., 1999. T*he Behavior of Integral Abutment Bridges*, Virginia: Virginia Transportation Research Council.

Barker, R.M., Duncan, J.M., Rojiani, K.B., Ooi, P.S.K., Tan, C.K., Kim, S.G., (1991). Manuals for the design of bridge foundations, National Cooperative Highway Research Program (NCHRP) Report 343, TRB, National Research Council, Washington, D.C.

Bozozuk, M. (1978). Bridge foundation move. *Transportation Research Record 678*, Transportation Research Board, Washington, D.C.

Breña, S.F., Bonczar, C.H., Civjan, S.A., DeJong, J.T., Crovo, D.S., (2007). Evaluation of Seasonal and Yearly Behavior of an Integral Abutment Bridge. *Journal of Bridge Engineering*, 12(3), 296-305. https://doi.org/10.1061/(ASCE)1084-0702(2007)12:3(296)

Burke, M.P. Jr. (2009). *Integral and semi-integral bridges*, Wiley-Blackell, Hoboken, NJ.

Caristo, A., Barnes, J., Mitoulis, S.A., (2018). Numerical modelling of integral abutment bridges under seasonal thermal cycles. *Proceedings of the Institution of Civil Engineers – Bridge Engineering*, 171(3), 179-190. https://doi.org/10.1680/jbren.17.00025

Chovichien, V. (2004). *The Behavior and Design of Piles for Integral Abutment Bridges* (Publication No. 3154604) [Doctoral dissertation, Purdue University]. ProQuest Dissertations Publishing.

Colorado Department of Transportation (2021). *Bridge Design Manual*, Highway Division, Colorado Department of Transportation: Denver, CO, USA.

CSA. (2014). Canadian Highway Bridge Design Code. CSA standard CAN/CSA-S6-14. Canadian Standards Association, Rexdale, Ontario, Canada.

Delaware Department of Transportation (2021). *Bridge Design Manual*, Highway Division, Delaware Department of Transportation: Harrington, DE, USA.

Dhadse, G.D., Ramtekkar, G.D., Bhatt, G., (2021). Finite Element Modeling of Soil Structure Interaction System with Interface: A Review. *Archives of Computational Methods in Engineering, 28*, 3415-3432. https://doi.org/10.1007/s11831-020-09505-2

District of Columbia Department of Transportation (2019). *Design and Engineering Manual*, Highway Division, District of Columbia Department of Transportation: Washington, D.C, USA.

England, G.L., David, B.I., Tsang, N.C.M., (2000). Integral Bridges: A Fundamental Approach to the Time-Temperature Loading Problem. Thomas Telford: London.

Florida Department of Transportation (2022). *Structures Design Guidelines*, Highway Division, Florida Department of Transportation: Tallahassee, FL, USA.

Freyermuth, C.L. (1969). Design of continuous highway bridges with precast, prestressed concrete girders. *Precast/Prestressed Concrete Institute Journal*, 14(2), 14-39. https://doi.org/10.15554/pcij.04011969.14.39

Frosch, R. J. & Lovell, D. M., (2011). *Long-Term Behaviour of Integral Abutment Bridges*, West Lafayette: Federal Highway Administration.

Frosch, R.J., Kreger, M.E., Talbott, A.M., (2009*). Earthquake Resistance of Integral Abutment Bridges*, West Lafayette: Purdue University.

Greimann, L.F., Yang, P.S., Wolde-Tinsae, A.M., (1986). Nonlinear Analysis of Integral Abutment Bridges. *Journal of Structural Engineering*, 112(10), 2263-2280. https://doi.org/10.1061/(ASCE)0733-9445(1986)112:10(2263)

Grover, R.A. (1978). Movements of Bridge Abutments and Settlements of Approach Pavements in Ohio. *Transportation Research Record 679*.

Hannigan, P.J., Rausche, F., Likins, G.E., Robinson, B.R., Becker, M.L., (2016). *Design and Construction of Driven Pile Foundations – Volume I* (No. FHWA-NHI-16-009). United States. Federal Highway Administration. Office of Technology Applications.

Hassiotis, S., Khodair, Y., Roman, E., Dehne, Y., (2006). Evaluation of Integral Abutments (No. FHWA-NJ-2005-025).

Hoppe, E.J. and Gomez, J.P. (1996). *Field study of an integral backwall bridge*, Virginia Transportation Research Council, VTRC 97-R7, October 1996, 47 p.

Hovarth, J.S. (2005). Integral-Abutment Bridges: Geotechnical Problems and Solutions Using Geosynthetics and Ground Improvement. *Proceedings of the 2005 FWHA Conference on Integral Abutment and Jointless Bridges*, Maryland, USA.

Huntley, S.A. and Valsangkar, A.J., (2013). Field monitoring of earth pressures on integral bridge abutments. *Canadian Geotechnical Journal*, 50(8), 841-857. https://doi.org/10.1139/cgj-2012-0440

Husain, I. and Bagnariol, D., (2000). Design and Performance of Jointless Bridges in Ontario: New Technical and Material Concepts. *Transportation Research Record*, 1696(1), 109-121. https://doi.org/10.3141%2F1696-14

Illinois Department of Transportation (2012). *Bridge Manual*, Highway Division, Illinois Department of Transportation: Springfield, IL, USA.

Kansas Department of Transportation (2007). *Design Manual Volume III-Bridge Section*, Highway Division, Kansas Department of Transportation: Topeka, KS, USA.

Kaufmann, W. and Alvarez, M. (2011). Swiss Federal Roads Office Guidelines for Integral Bridges. *Structural Engineering International*, 21(2), 189-194. https://doi.org/10.2749/101686611X12994961034057

Khodair, Y.A. (2009). Lateral earth pressure behind an integral abutment. *Structure and Infrastructure Engineering*, 5(2), 123-136. https://doi.org/10.1080/15732470600924706

Kunin, J. and Alampalli, S. (2000). Integral Abutment Bridges: Current Practice in United States and Canada. *Journal of Performance of Constructed Facilities*, 14(3), 104-111. https://doi.org/10.1061/(ASCE)0887-3828(2000)14:3(104)

LaFave, J.M., Riddle, J.K., Jarrett, M.W., Wright, B.A., Svatora, J.S., An, H., Fahnestock, L.A., (2016). Numerical Simulations of Steel Integral Abutment Bridges under Thermal Loading. *Journal of Bridge Engineering*, 21(10). https://doi.org/10.1061/(ASCE)BE.1943-5592.0000919

Massachusetts Department of Transportation (2020). *LRFD Bridge Manual – Part I*, Highway Division, Massachusetts Department of Transportation: Boston, MA, USA.

Minnesota Department of Transportation (2016). *Design Manual*, Highway Division, Minnesota Department of Transportation: St. Paul, MN, USA.

Mourad, S. and Tabsh, S.W., (1999). Deck slab stresses in Integral Abutment Bridges. *Journal of Bridge Engineering*, 4(2), 125-130. https://doi.org/10.1061/(ASCE)1084-0702(1999)4:2(125)

Munuswamy, S. (2004). Creep and Shrinkage effects on Integral Abutment Bridges (Publication No.3119993) [Doctoral dissertation, Florida Atlantic University]. ProQuest Dissertations Publishing.

Nebraska Department of Roads (2016). *Bridge Office Policies and Procedures*, Nebraska Department of Roads Bridge Division: Lincoln, NE, USA.

New Hampshire Department of Transportation (2015). *Bridge Design Manual*, Highway Division, New Hampshire Department of Transportation: Concrod, NH, USA.

New Mexico Department of Transportation (2018). *Bridge Procedures and Design Guide*, Highway Division, New Mexico Department of Transportation: Santa Fe, NM, USA.

New Zealand Transport Agency (2013). *Bridge Manual*, 3rd ed, SP/M/022. New Zealand Transport Agency: Wellington, New Zealand.

Oregon Department of Transportation (2020). *Bridge Design Manual*, Highway Division, Oregon Department of Transportation: Salem, OR, USA.

Pennsylvania Department of Transportation (2019). *Design Manual*, Highway Division, Pennsylvania Department of Transportation: Harrisburg, PA, USA.

Roads and Traffic Authority (2007). *Policy Circular BPC 2007/05*, Design of Integral Bridges: Sydney, Australia.

Rodriguez, L.E., Barr, P.J., Halling, M.W., (2014). Temperature Effects on a Box-Girder Integral-Abutment Bridge. *Journal of Performance of Constructed Facilities*, 28(3), 583-591. https://doi.org/10.1061/(ASCE)CF.1943-5509.0000437

South Carolina Department of Transportation (2006). *Bridge Design Manual*, Highway Division, South Carolina Department of Transportation: Columbia, CS, USA.

Sigdel, L.D., Al-Qarawi, A., Leo, C.J., Liyanapathirana, S., Hu, P., (2021). Geotechnical Design Practices and Soil–Structure Interaction Effects of an Integral Bridge System: A Review. *Applied Sciences*, 11(15), 7131. https://doi.org/10.3390/app11157131

Soltani, A.A. and Kukreti, A.R., (1992). Performance evaluation of integral abutment bridges. *Transportation Research Record 1371*.

State of North Carolina Department of Transportation (2007). *Design Manual*, Highway Division, State of North Carolina Department of Transportation: Raleigh, NC, USA.

Tabatabai, H., Magbool, H., Bahumdain, A., Fu, C., (2017). Criteria and Practices of Various States for the Design of Jointless and Integral Abutment Bridges. *Proceedings of the 3rd international workshop on Jointless Bridges Conference.* Seattle, USA.

Tabrizi, A., Clarke-Sather, A., Schumacher, T., Healy, R., (2016). Bridge Retrofit or Replacement Decisions: Tools to Assess Sustainability and Aid Decision-Making. (No. CAIT-UTC-NC5), University of Delaware. Newark, Delaware.

Texas Department of Transportation (2020). *Bridge Design Manual-LRFD*, Highway Division, Texas Department of Transportation: Austin, TX, USA.

Vermont Department of Transportation (2019). *VTrans Structures Design Manual*, 5th ed, Highway Division, Vermont Department of Transportation: Montpelier, VT, USA.

Wahls, H.E. (1990). Design and Construction of Bridge Approaches. *National Cooperative Highway Research Program Synthesis of Highway Practice 159*, Transportation Research Board, National Research Council, Washington, D.C.

Walkinshaw, J.L. (1978). Survey of Bridge Movements in the Western United States. *Transportation Research Record 678*, Transportation Research Board, Washington, D.C.

West Virginia Department of Transportation (2004). *Bridge Design Manual*, Highway Division, West Virginia Department of Transportation: Charleston, WV, USA.

Weyers, R.E., Cady, P.D., Hunter, J.M., (1988). Cost-Effective Bridge Maintenance and Rehabilitation Procedures. *Transportation Research Record 1184*, Transportation Research Board, Washington, D.C.

White II, H., Pétursson, H., Collin, P., (2010). Integral Abutment Bridges: The European Way. *Practice Periodical on Structural Design and Construction*, 15(3), 201-208. https://doi.org/10.1061/(ASCE)SC.1943-5576.0000053

Wisconsin Department of Transportation (2021). *Bridge Manual*, Highway Division, Wisconsin Department of Transportation: Madison, WI, USA.

Wyoming Department of Transportation (2013). *Bridge Design Manual*, Highway Division, Wyoming Department of Transportation: Cheyenne, WY, USA.

Yang, P., Wolde-Tinsae, A.M., Greimann, L.F., (1985). Effects of Predrilling and Layered Soils on Piles. *Journal of Geotechnical Engineering*, 111(1), 18-31. https://doi.org/10.1061/(ASCE)0733-9410(1985)111:1(18)

Yokel, F.Y. (1990). Proposed Design Criteria for Shallow Bridge Foundations. National Institute of Standards and Technology Report No. NISTIR 90-4248, 50pp.

Zhao, J.J. and Tonias, D.E., (2014). Bridge Engineering: Design, Rehabilitation and Maintenance of Modern Highway Bridges. 2nd ed. Lulu Press, Inc., Morrisville, NC.

CHAPTER 3 TWO-DIMENSIONAL MODELLING OF INTEGRAL ABUTMENT BRIDGES

Ahmed Abdullah and Hany El Naggar

3.1 Introduction

Bridge construction is one of the oldest geostructural engineering practices. The use of integral abutment bridges (IABs), first introduced in the 1930s, began to become more widespread in the late 1960s. These bridges utilize a continuous rigid build between the superstructure and the substructure (Kong et al. 2016). The monolithic assembly of IABs eliminates the necessity of utilizing expansion joints and bearings (Civjan et al. 2007). In comparison to conventional bridges, IABs have reduced construction and maintenance costs, and can be constructed more quickly due to their simple design. Furthermore, these structures can utilize a single row of straight piles oriented for weak-axis bending to achieve greater end span ratios. Research conducted by Hoppe and Gomez (Hoppe and Gomez 1996) has indicated enhanced seismic performance with the use of IABs. In addition, the smooth, continuous nature of IABs has been found to improve driving comfort (Arsoy et al. 1999). Since the superstructure and substructure components act as a rigid body, at extreme high and low temperatures, the deck and girders undergo thermally induced lateral expansion and contraction, resulting in displacement of the abutments (Kim and Laman 2010). As the abutments move away and towards the backfill soil, resultant active and passive earth pressures occur at the abutment wall-backfill interface. In addition, the lateral response of the abutment to falling and rising temperatures induces positive and

negative bending moments in the foundation piles, since the piles are rigidly embedded in the concrete pile caps.

Due to the relatively recent introduction of IABs, their complex response to cyclic thermal loading and associated soil-structure interactions (SSIs) has yet to be completely understood. However, by using finite element (FE) techniques, researchers can conduct numerical studies to analyze changes in performance under varying conditions. As an aid to understanding the complex SSIs associated with IABs during seasonal changes, researchers have conducted full-scale monitoring and numerical research to study the lateral response of IABs to different site conditions. For example, Huang et al. (Huang et al. 2013) installed more than 150 gages at various locations to monitor the thermal response of the #55555 concrete bridge in Rochester, Minnesota, over a seven-year period. Over the course of the monitoring period, time-dependent effects were observed in the bridge deck and girder components. They became gradually shorter each year, which ultimately induced greater stresses in the piles, causing pile curvatures to increase. Research conducted by LaFave et al. (LaFave et al. 2021) involved monitoring the effects of thermal loading on the Kishwaukee and Union Pacific Railroad (UPRR) bridges in Illinois over a two-year period. A 3D FE system was subsequently calibrated against the field results. Comparisons with data acquired in the field indicated that abutment movements and girder stresses associated with temperature changes were captured reasonably well by the FE system. However, following the first year of monitoring, disagreements between the FE simulations and the measured data were observed in the tensile and compressive stresses at the girder bottom flanges, due to unpredicted field behaviors. Over a period of three years, Huntley and Valsangkar (Huntley and Valsangkar 2013; Huntley and Valsangkar

2014) carried out full-scale monitoring of the route 2 high-speed connector underpass bridge in New Brunswick, Canada. More than 100 instruments were used to monitor earth pressure and pile bending moment variations resulting from thermal contraction and expansion. It was found that in addition to thermal variations in earth pressure, lateral abutment movements associated with temperature changes also impacted earth pressure distributions. Furthermore, the supporting piles exhibited a double curvature, with maximum bending moments occurring at the pile head. In a three-year field study, Breña et al. (Breña et al. 2007) monitored the thermal response of the Orange-Wendell (OW) bridge in Massachusetts, USA. Field data suggested that the bridge abutments deformed as a rigid body through translations and rotations, with the greatest displacements occurring at the top of the abutment. Abutment rotations were seen to reduce the maximum moments occurring at the pile head. Maximum passive earth pressures were observed during periods of extreme abutment displacement due to expansion. In addition, soil settled near the base of the abutment following contraction resulted in increased passive pressures as the abutment transitioned into an expansion position. Civjan et al. (Civjan et al. 2007) continued research investigations of the OW bridge by conducting parametric studies with calibrated 2D and 3D FE models. The results showed that as the stiffness of the backfill increased, earth pressures increased, and pile moments decreased. In addition, lateral restraints provided by the surrounding soil were observed to impact pile bending moments only during periods of contraction.

Most previous research models the SSIs of IABs under cyclic thermal loading by using plate elements and spring elements to represent a discontinuous medium. Linear elastic plate elements are used to model the axial and flexural rigidities of structural components

such as abutments, girders, and piles. Surrounding soils are modelled as spring elements, defined incrementally at points along the plate depth. The stiffness values (k_h) of the defined spring elements are commonly determined by using linear/nonlinear models found in the literature. Thus, the lateral and vertical displacements and stresses generated are simulated only at the corresponding plate-spring nodes under loading. This study aims to build on previous research by modelling the SSIs of IABs under cyclic thermal loading within a continuous soil medium, with corresponding interface elements. This is designed to yield a more realistic representation of the relative deformations of soil and structural elements over their entire depth, thereby mimicking behaviors observed in the field. The mechanical behavior of soils can be defined by using constitutive soil models which relate applied stresses to strains, based on established mathematical models which consider nonlinear effects, the stress-dependency of stiffness, strain-hardening/softening effects, and time-dependent effects (PLAXIS 2D manuals 2018).

First the case study selected for the present research will be described, in accordance with Kalayci et al., including specifics regarding the full-scale monitoring program, the instrumentation plan, the construction sequence, and the data acquired during the monitoring phase (Kalayci 2012). Then details of the development of a calibrated two-dimensional finite-element model using PLAXIS 2D and its verification against data recorded in the field will be presented. Explanations concerning the approximation of contractions and expansions as a function of bridge geometry, temperature changes, and material properties will then be given, with the corresponding findings. Finally, a description will be provided of the parametric studies conducted with the calibrated FE system to investigate the effect of varying the constitutive soil model, backfill stiffness,

abutment concrete stiffness, pile size and orientation, and span length on backfill earth pressure distributions and pile bending moments resulting from cyclic thermal loading.

3.2 Case study review

The Middlesex bridge over Martin's brook is located on route VT12 in Vermont, USA. Construction began in mid-June 2009 and continued for four and a half months. The bridge was opened to traffic in late October 2009. Table (3.1) shows the starting dates of the key construction activities.

The Middlesex bridge is a single span bridge with a length of 43 m between the center lines of abutments 1 and 2. Each abutment has an out-of-plane width of 10.2 m and a thickness of 1 m. Since the abutment diaphragm and pile cap were poured separately, a construction joint was used to ensure a fixed connection between these two components. The bridge has a 0^{o} skew from the axis parallel to the roadway. The superstructure consists of a reinforced concrete (RC) deck 0.22 m thick, with five grade 345W steel plate girders evenly spaced at intervals of 2.05 m and anchor bolted into the bridge abutments. The substructure is comprised of five HP 310 x 125 steel piles (grade 345) evenly spaced at intervals of 2.05 m, to support each abutment. The piles are embedded 1 m into the pile cap to ensure fixed head conditions relative to the abutment during lateral movements. In addition, piles were driven 9 m into the in-situ soil below the base of the abutment. Each abutment is monolithically connected to two rectangular wing walls perpendicular to the orientation of the abutment. Each wing wall has a thickness of 0.45 m and extends 3 m from the back wall of the abutment. A reinforced concrete approach slab with a length of 6 m and a

thickness of 0.38 m was constructed behind the back wall of the abutment. The bridge schematics are shown in Figure (3.1).

According to reports prepared by the Vermont Agency of Transportation (VTrans), the in-situ soils were classified as cohesionless, and the backfill soil was classified as compacted granular medium dense soil. The subgrade soil, with a slope of 1V:1.5H, consisted of two layers: A top layer 1.5 m thick comprised of compacted medium dense sand, above a layer 10 m thick of medium dense sand and silty sands with some gravel, with bedrock below. Groundwater investigations suggested that the groundwater table was encountered at the base of the abutment.

Table 3.1 Middlesex bridge construction sequence (Kalayci 2012)

Construction activity	**Starting date (mm/dd/yyyy)**
Pile driving	06/15/2009
Pouring of pile cap	07/15/2009
Backfilling of pile cap soil	07/22/2009
Girder placement	07/22/2009
Placement of deck	08/27/2009
Pouring of upper abutment	09/21/2009
Backfilling of upper abutment	10/07/2009
Placement of approach slab	10/09/2009

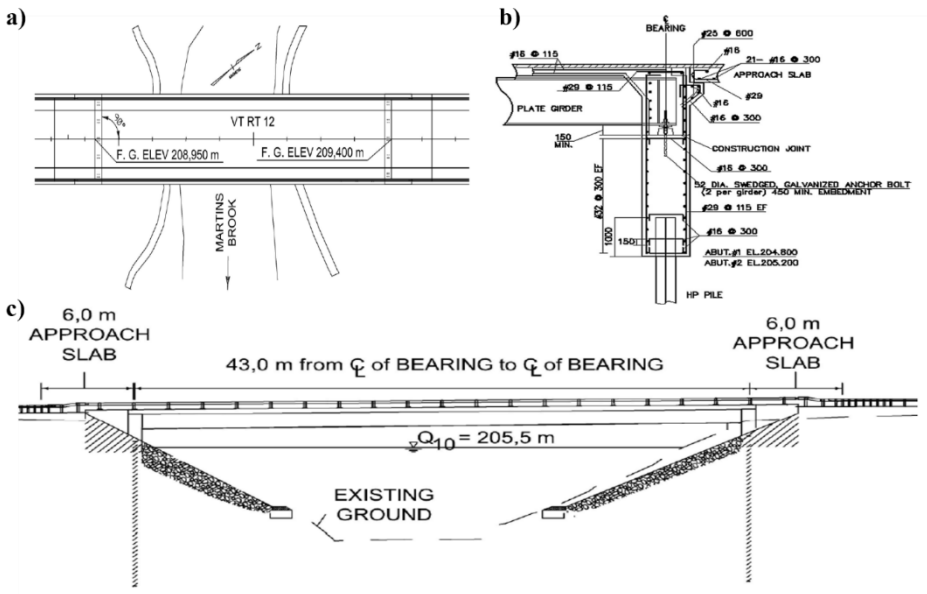

Figure 3.1 Bridge: **(a)** Plan view, **(b)** abutment cross-section, and **(c)** elevation view (Civjan et al. 2013)

3.2.1 Bridge Instrumentation

For abutments 1 and 2, instrumentation was installed to monitor backfill pressure distributions, abutment displacements and rotations, and pile moments. However, this paper focuses primarily on results related to earth pressure distributions and pile bending moments for abutment 1. Further details regarding the instrumentation and data collected can be found in Kalayci (Kalayci 2012). All the instruments mentioned in this section are vibrating wire (VW) gages. Figure (3.2) presents the instrumentation plan of the Middlesex bridge.

Seven Geoken 4815 earth pressure cells were installed at three different heights beneath the construction joint to capture earth pressure variations at the abutment-backfill interface. Each gage was comprised of a transducer housing and a circular pressure cell. Installation was performed by nailing the pressure cells onto the formwork of the pile

cap prior to backfilling. This ensured that the pressure cells were securely attached to the back wall and were in flush contact with the backfill soil. As part of the transducer housing, the VW gages were positioned at a small distance from the back wall surface. To monitor variations in pile strains under cyclic thermal loading, five Geokon 4000 strain gages were placed on the supporting piles. Since maximum moments occur near the base of the abutment, three strain gages spaced 0.5 m apart and two strain gages spaced 1 m apart were installed on the exterior and interior piles, respectively. First the piles were driven 9 m into the in-situ soil, then the top 1.5 m of soil surrounding the piles was excavated. Mounting blocks aligned parallel to the roadway were then attached to the flanges to hold the strain gages in place. Following installation of the gages, the excavated soil was then backfilled and compacted.

Data acquisition was performed by Campbell Scientific CR1000 and CR10X data loggers programmed to gather data from the bridge instrumentation every six hours for a period of two years. Data were not collected between April 20, 2011, and May 13, 2011, due to equipment damage caused by electrical storms.

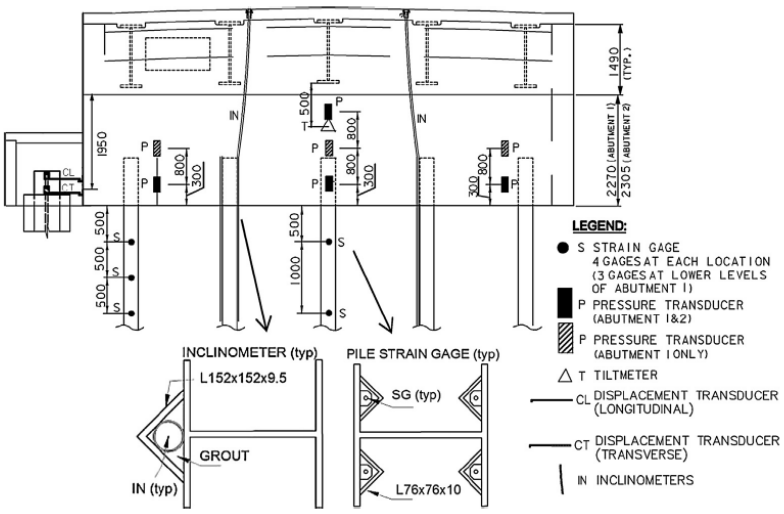

Figure 3.2 Middlesex bridge instrumentation plan (Civjan et al. 2013)

3.3 Finite element model

Abutment-backfill and pile-soil interactions during cyclic thermal loading were analyzed numerically by utilizing the software package PLAXIS 2D 2021. The first part of the analysis involved verification of the 2D model against data obtained from full-scale monitoring in the field. The second part of the analysis used the calibrated system to conduct parametric studies to investigate changes in performance when key parameters were varied. Details concerning the model development, verification, and parametric studies are presented below.

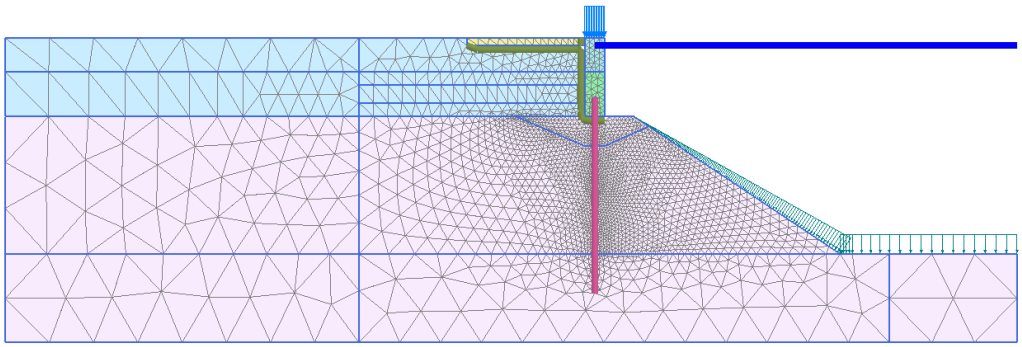

Figure 3.3 Two-dimensional FE model mesh

3.3.1 Mesh

The 2D model developed for verification is illustrated in Figure (3.3). In the model, 15-node triangular volume elements were selected from the element library of PLAXIS 2D to simulate soil layers and concrete clusters. For enhanced compatibility, by default, PLAXIS formulates each embedded beam and plate by using 5-node beam elements, when they are surrounded by 15-node triangular soil elements. After the mesh coarseness was set to fine, the verified model contained approximately 5000 elements. Elements near the abutment and pile deformation zones had an average size of approximately 40 mm. In accordance with the results of a sensitivity analysis, the left boundary of the model illustrated in Figure (3.3) was set to 30 m from the center of the abutment, since it was found that greater distances resulted in insignificant changes to earth pressures and pile moments.

3.3.2 Boundary conditions

Because the Middlesex bridge is straight and is symmetric about both horizontal axes, only half the bridge was modelled. The boundary conditions were set to be fixed in the

horizontal direction and free in the vertical direction. The bottom boundary condition was set to be fully fixed, while the top boundary was permitted to have free displacement in both directions.

3.3.3 Backfill and subgrade soil properties

The backfill soils behind the abutment wall and surrounding the piles were modelled by using the elasto-plastic hardening soil (HS) model extracted from the PLAXIS 2D constitutive soil model library (PLAXIS 2D manuals 2018), with a confining pressure (p_{ref}) of 100 kPa. This double-stiffness constitutive soil model simulates stress-dependent changes in soil stiffness when the soil is subjected to thermal expansions and contractions (Mahgoub and El Naggar 2020). The hyperbolic nature of the hardening soil model developed by Duncan and Chang (Duncan and Chang 1970) is related to double-stiffness hyperbolic models (Zakhem and El Naggar 2019). Furthermore, the HS constitutive soil model yields accurate stiffness variations for small shear strain magnitudes through hysteretic behavior and dilatancy during shearing (El Naggar et al. 2016). The soil properties defined for simulation of the backfill and subgrade soils are summarized in Table (3.2).

Table 3.2 FE model soil properties

Parameter	Backfill soil[1]	Subgrade soil[2]
Dry unit weight, γ_{dry} ($^{kN}/_{m^3}$)	17	19
Saturated unit weight, γ_{sat} ($^{kN}/_{m^3}$)	18.5	20
Secant stiffness in standard drained triaxial test, E_{50}^{ref} (kPa)	20	50
Tangent stiffness for primary oedometer loading, E_{oed}^{ref} (kPa)	16	40
Unloading/reloading stiffness, E_{ur}^{ref} (kPa)	60	150
Cohesion, c' (kPa)	1	2
Internal friction angle, φ' (^{o})	35	35
Dilatancy, ψ (^{o})	5	5
Power for stress-level dependency of stiffness, m	0.5	0.5

[1]For the backfill soil P_{ref} = 100 kPa and R_{int} = 0.3
[2]For the subgrade soil P_{ref} = 100 kPa and R_{int} = 0.6

3.3.4 Abutment and approach slab reinforced concrete properties

The PLAXIS software material model library supports the use of a linear-elastic material to model extremely stiff volumes. In accordance with Hooke's law of isotropic elasticity, the linear-elastic material model requires only the input of an elastic modulus (E) and Poisson's ratio (v) (PLAXIS 2D manuals 2018). Because actual abutment and approach slab dimensions were used to simulate the physical structure, due to the 2D nature of the software, the model illustrated in Figure (3.3) incorporates an out-of-plane width of 1 m. The elastic modulus was set to 23 GPa for the abutment pile cap, and 25 GPa for the abutment diaphragm and approach slab components. All the concrete elements were defined with a unit weight of 24 kN/m^3 and a Poisson's ratio of 0.2. To model the relative movement between the soil and the concrete element nodes, 5-node UDCAM-S interface

elements were defined. A strength reduction factor (R_{int}) of 0.3 was used at the abutment-backfill and approach slab interfaces for lateral contractions and expansions.

3.3.5 Bridge pile and composite deck and girder properties

The steel HP piles were modelled by using elastic embedded beam elements. These 5-node elements with zero thickness utilize Mindlin beam element theory and combine plate and node-to-node anchor characteristics (PLAXIS 2D manuals 2018). These elements also use actual pile dimensions to generate equivalent elastic zones surrounding an embedded beam. This permits relative movement between the pile and soil elements, while formulating axial and flexural rigidities (Sluis et al. 2014). A strength reduction factor (R_{int}) of 0.6 was used to model relative lateral and axial displacements at the pile-soil interfaces. In the FE system, the piles were defined with an area of 0.016 m^2, a weak-axis moment of inertia of 0.09 x 10^{-3} m^4, and an out-of-plane spacing of 2.05 m.

Deck and girder sections were modelled as an equivalent elastic steel plate element, in accordance with methods described by Bonczar et al. (Bonczar et al. 2005). First, the concrete deck was transformed into an equivalent steel section. Axial and bending rigidities of the steel deck, with girders spaced 2.05 m apart, were then incorporated into an equivalent single composite section, with an out-of-plane width of 1 m. The combined axial (EA) and bending (EI) rigidities were set to be equal to 113 x 10^6 kN/m and 37.5 x 10^6 kN.m^2/m. An elastic modulus of 200 GPa was used to model the deck, girder, and pile elements.

3.3.6 Staged construction

The construction sequence defined for the calibrated FE model was based on actual construction records for the Middlesex bridge. The initial step was performed in accordance with the K_0 procedure, where in-situ soil stresses are varied linearly with depth, depending upon the unit weight of the soil. An excavation with a slope of 1V:1.5H was simulated for the top 1.5 m of the in-situ soil. Following the excavation, a steel HP pile element was activated. The simulation then reactivated and compacted the excavated soil cluster. Next, the pile cap cluster was activated, together with the abutment base interface element. The first layer of backfill soil, with a thickness of 2.27 m, was backfilled and compacted behind the pile cap, and the backfill-pile cap interface was activated. This was followed by activation of the abutment diaphragm, deck and girder composite plate, and vertical load. The remaining backfill soil, with a thickness of 1.73 m, was then backfilled and compacted behind the diaphragm wall, and the backfill-diaphragm wall interface was activated. Then the approach slab cluster and remaining interface elements were activated. Finally, the prescribed lateral displacements extracted from the full-scale monitoring inclinometer data were applied cyclically at the top of the abutment, to simulate the two-year contraction and expansion responses to thermal variations.

3.3.7 Parametric studies

Following the development of the proposed 2D FE system, parametric studies were used to investigate the effect of varying the constitutive soil model, backfill stiffness, abutment concrete stiffness, pile size and orientation, and span length on the resultant backfill lateral stress distributions and pile bending moments.

The first parametric study investigated the effects of using the linear-elastic perfectly plastic Mohr-Coulomb (MC) model provided by the PLAXIS 2D model library to model the soil behavior. In this parametric study, instead of using the hardening soil model employed in the calibrated 2D FE system, the MC constitutive soil model was used to simulate the backfill and subgrade soils.

The second parametric study investigated the effect of using backfill soils with varying stiffness, ranging from loose sand (with the least stiffness) to gravel (with the greatest stiffness). The four types of backfill soil utilized in this parametric study were loose sand (E_{50}^{ref} = 7.5 MPa), medium sand (E_{50}^{ref} = 20 MPa), dense sand (E_{50}^{ref} = 60 MPa), and gravel (E_{50}^{ref} = 150 MPa). All of the elastic moduli were determined at a confining pressure (P_{ref}) of 100 kPa.

The third parametric study investigated the impact of varying the stiffness of the concrete used for the abutment. The concrete classes used in this parametric study were class A (E = 23.2 GPa), class B (E = 21.5 GPa), and class C (E = 24.9 GPa).

The fourth parametric study investigated the effect of employing piles of different sizes, oriented for weak- or strong-axis bending. In this study, HP pile sections HP 200 x 53, HP 250 x 85, HP 330 x 149, and HP 360 x 174 were utilized. Table (3.3) presents the area and the strong- and weak-axis moments of inertia for each of the pile sections used.

The fifth parametric study investigated the effect of varying the span length (from 43 m to 8.6 m) and hence the corresponding vertical load (VL). FE models with one span (43 m; VL = 326 kN), two spans (21.5 m; VL = 125 kN), three spans (14.3 m; VL = 89 kN), four spans (10.75 m; VL = 66 kN), and five spans (8.6 m; VL = 53 kN) were considered.

Table 3.3 HP pile sections used in the fourth parametric study

HP pile section	Section area, A (m^2)	Strong-axis moment of inertia, I_1 (m^4)	Weak-axis moment of inertia, I_2 (m^4)
HP 200 x 53	6.84×10^{-3}	49.4×10^{-6}	16.8×10^{-6}
HP 250 x 85	10.8×10^{-3}	123×10^{-6}	42×10^{-6}
HP 330 x 149	19×10^{-3}	370×10^{-6}	123×10^{-6}
HP 360 x174	22.2×10^{-3}	508×10^{-6}	184×10^{-6}

3.4 Results and Discussion

First, the results of full-scale monitoring of the Middlesex bridge will be discussed, together with the verification of the FE model developed to mimic the soil-structure interactions occurring at the abutment-backfill and pile-soil interfaces during cyclic thermal loading. Details concerning alternative methods that can be used to model the thermally induced lateral loading of IABs will then be presented, and findings of the FE model will be compared to the results of full-scale monitoring of the thermal response. The third part of this section will report findings of the parametric studies and will assess the thermal responses indicated by the calibrated FE system when key parameters are varied.

3.4.1 Results of full-scale monitoring

Extensive data were acquired by Kalayci (Kalayci 2012) via full-scale monitoring of the thermal response of the Middlesex bridge. However, the present study focuses primarily on lateral stress distributions in the backfill soil and internal pile bending moments caused by thermally induced abutment displacements. Earth pressure and pile bending moment results obtained from the FE model simulations are plotted together with

values measured during full-scale monitoring to verify the reliability of the proposed system.

3.4.1.1 Lateral earth pressure distribution

Table (3.4) presents the cumulative earth pressure at the end of construction at each sensor location.

Figure (3.4) compares variations in the lateral earth pressure obtained by the FE model via PLAXIS with values measured in the field at three sensor locations. As shown in Figure (3.4), the results obtained from the PLAXIS FE simulations closely adhere to the data collected in the field. The figure indicates that bridge contractions and expansions induced incremental increases and decreases in the cumulative pressures observed at the end of construction. This caused backfill stresses to fluctuate between passive and active states as the ambient temperatures varied with time. In addition, with greater abutment displacements into the backfill soil due to bridge expansion, the induced incremental stresses at the abutment-backfill interface were seen to increase. During passive states, earth pressure distributions were observed to follow a linear pattern, as measured stresses increased with depth. However, during periods of contraction, a nonlinear pattern appeared, since lower active stresses were measured at the middle sensor than at the top and bottom sensors. This unpredicted behavior can be explained by considering the pressure reading at the middle sensor at the end of construction. The reading suggests that prior to the occurrence of thermally induced effects, the earth pressure at the middle sensor was lower than the pressures at the top and bottom sensors. Possibly this was due to soil interactions during construction that affected data collection at the middle sensor. In this case, induced

incremental reductions in pressure during periods of contraction would further reduce the cumulative value at the middle sensor, thus giving rise to a nonlinear distribution.

The earth pressure data plotted in Figure (3.4) do not indicate soil ratcheting, since no gradual increase in passive pressure was observed for successive passive cycles. As shown in Figure (3.4), the passive pressure at the bottom sensor was 66 kPa the first year and 68 kPa the second year. Similarly, pressures of 53 kPa and 52 kPa were measured at the middle sensor during the first and second passive cycles, respectively. In fact, evidence of soil softening was seen at the top sensor, since the pressure of 52 kPa measured the first year decreased by 10 kPa following the second expansion cycle, despite the observed net inward movement described by Kalayci (Kalayci 2012).

Table 3.4 Cumulative earth pressures at three sensor locations at the end of construction (Civjan et al. 2013)

Sensor location	**Earth pressure at the end of construction (kPa)**
Top	33.1
Middle	21.4
Bottom	42.1

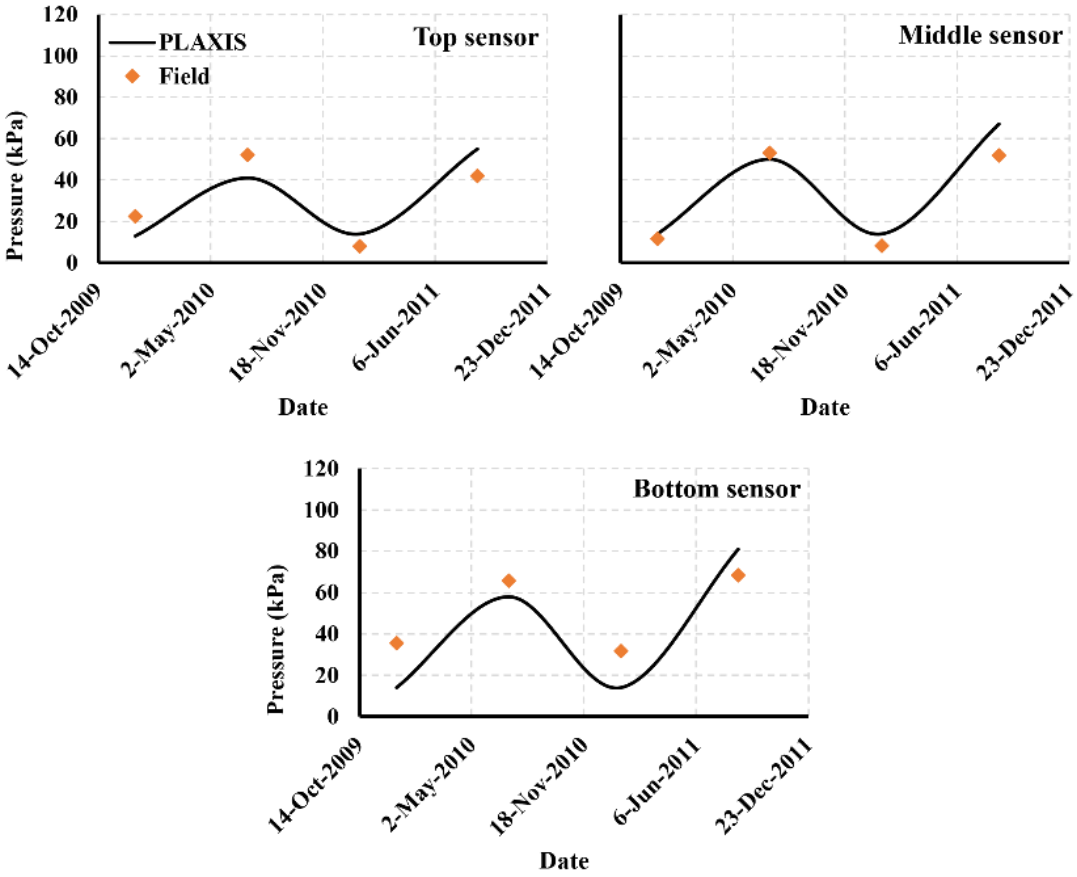

Figure 3.4 Verification of lateral earth pressures at the three sensor locations

3.4.1.2 Pile moments

Table (3.5) presents cumulative pile bending moments at the end of construction at three strain gage locations. Positive pile bending moments correspond to tensile strains on the side of the pile facing the embankment and compressive strains on the side facing the backfill, while negative pile bending moments correspond to compressive strains on the side of the pile facing the embankment and tensile strains on the side facing the backfill.

Figure (3.5) compares variations in pile bending moments at maximum and minimum temperatures obtained by the FE model via PLAXIS with values measured in the field at three strain gage locations. As can be seen in Figure (3.5), the pile bending moment results obtained from the PLAXIS FE simulations show excellent agreement with the values measured during full-scale monitoring of the substructure. Thermally induced lateral contractions and expansions caused the piles to bend in a double curvature, since the pile bending moments alternated between positive and negative values with increasing pile depth. During thermally induced bridge contractions, positive bending moments at the pile head decreased with increasing pile depth, until an inflection point was reached. This pile bending moment pattern is illustrated in Figures (3.5a) and (3.5c), which plot values obtained at minimum temperatures. In contrast, during thermally induced bridge expansions, the pile bending moment pattern had an opposite tendency, as illustrated in Figures (3.5b) and (3.5d), which plot values obtained at maximum temperatures. In this case, positive bending moments at the pile head were significantly reduced, thus introducing an additional inflection point slightly below the abutment base.

As shown in Figures (3.5a) and (3.5c), the maximum pile moments at the pile head were M_{Max}^{+ve} = 97 kN.m and M_{Max}^{+ve} = 80 kN.m, respectively. However, during bridge expansion, negative bending moments developed at the pile head, with the greatest absolute value of M_{Max}^{-ve} = -50 kN.m occurring during the second expansion cycle, as shown in Figure (3.5d). In addition, maximum positive bending moments occurred at approximately 1 m and 1.5 m below the base of the abutment, as shown in Figures (3.5b) and (3.5d), respectively. Finally, it should be noted that over the two-year monitoring period, the specified yield

moment of M_{yy} = 251 kN.m was not exceeded, as the maximum recorded bending moment of M_{Max} = 97 kN.m was approximately 61% lower than the yield moment.

Table 3.5 Cumulative pile bending moments at the end of construction (Civjan et al. 2013)

Strain gage location	Pile bending moment at the end of construction[1] (kN.m)
Top	38
Middle	36.6
Bottom	24.4

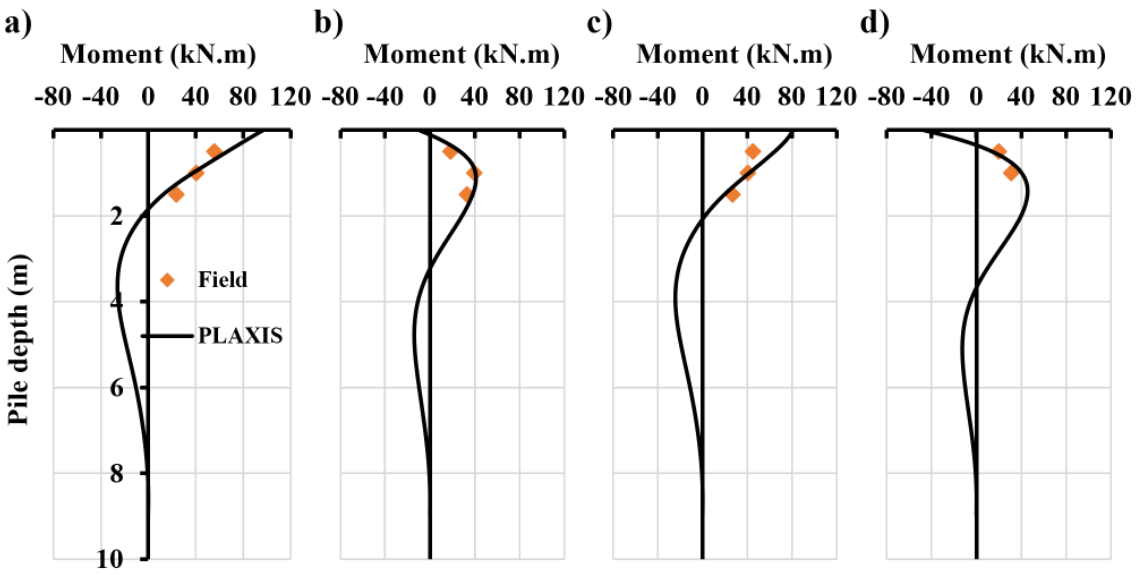

Figure 3.5 Verification of pile bending moments at maximum and minimum temperatures: **(a)** 12/19/2009 (T_{Min} = -12.5°C), **(b)** 07/07/2010 (T_{Max} = 38°C), **(c)** 01/23/2011 (T_{Min} = -13°C), and **(d)** 08/20/2011 (T_{Max} = 32.2°C)

3.4.2 Modelling of thermally induced loading

The extent of abutment lateral displacement during thermally induced loading can be quantified via full-scale monitoring setups. This involves installing displacement meters at

various heights on the abutment wall. However, researchers are sometimes required to conduct numerical analyses to assess the soil-structure interactions of IABs in the absence of data acquired in the field. Therefore, this section will first present an estimation of thermally induced abutment displacements, as discussed by Hibbeler (Hibbeler 2014). Secondly, in the present study, in addition to the calibrated FE system, another model was developed to utilize calculated abutment displacements to obtain corresponding earth pressures and pile bending moments.

Thermally induced abutment displacements $\Delta\delta$ (m) near the top of the abutment can be calculated as a function of the incremental temperature change ΔT (°C), the coefficient of thermal expansion of the deck and girder composite material α (/°C), and the bridge length L (m), by using Eq. 1 (Hibbeler 2014):

$$\Delta L = \alpha \Delta T \left(\frac{L}{2}\right) \quad \textbf{(1)}$$

Table (3.6) compares calculated displacements at the top of the abutment with data acquired in the field. Abutment displacements calculated by using Eq. 1 agreed reasonably well with the field data for the first contraction and expansion cycle and the second contraction cycle. However, significant discrepancies appeared for the second expansion cycle, where the calculated displacement was 10 mm (63%) less than the displacement measured in the field. This may be attributable to the linear relationship between the incremental displacements and changes in temperature assumed by Eq. 1. Thus, the calculation captured the time-dependent movement of the abutment toward the backfill soil only roughly, as found by Kalayci (Kalayci 2012).

Figure (3.6) compares lateral earth pressure curves generated via measured field data and theoretical methods with simulated displacements. As shown in Figure (3.6), there was close agreement between the theoretical and measured results for active pressures at the three pressure sensor locations. However, in the first expansion cycle, the 3 mm underestimation of displacement by the theoretical method resulted in a 12%, 8%, and 0% underestimation of the passive stresses occurring at the top, middle, and bottom sensor, respectively. In the second expansion cycle, the 10 mm underestimation of displacement by the theoretical method resulted in a 35%, 28%, and 23% underestimation of the passive stresses at the top, middle, and bottom sensors, respectively.

Figure (3.7) compares pile bending moment profiles generated via measured field data and theoretical methods with simulated displacements. As shown in Figure (3.7), in the contraction cycles, there was close agreement between the theoretical and measured results for the pile bending moment profiles. However, in the first expansion cycle, the 3 mm underestimation of displacement by the theoretical method resulted in a 20% underestimation of the maximum positive bending moment. In the second expansion cycle, the 10 mm underestimation of displacement by the theoretical method resulted in a 35% underestimation of the maximum positive bending moment and a 300 mm upward shift of the second point of inflection.

Table 3.6 Comparison between the field data and simulated lateral abutment displacements

Loading cycle	ΔT(°C)	Dates of max & min temperatures	Field data displacements[1] (mm)	Simulated displacements[1] (mm)
First contraction	-20	December 2009	7	5
First expansion	+30	July 2010	11	8
Second contraction	-21	January 2011	6	5
Second expansion	+24	August 2011	16	6

Note: ΔT = temperatures on the coldest and hottest days, using 7.8°C as a reference temperature.
[1]These displacements correspond to lateral movements at the top of the abutment.

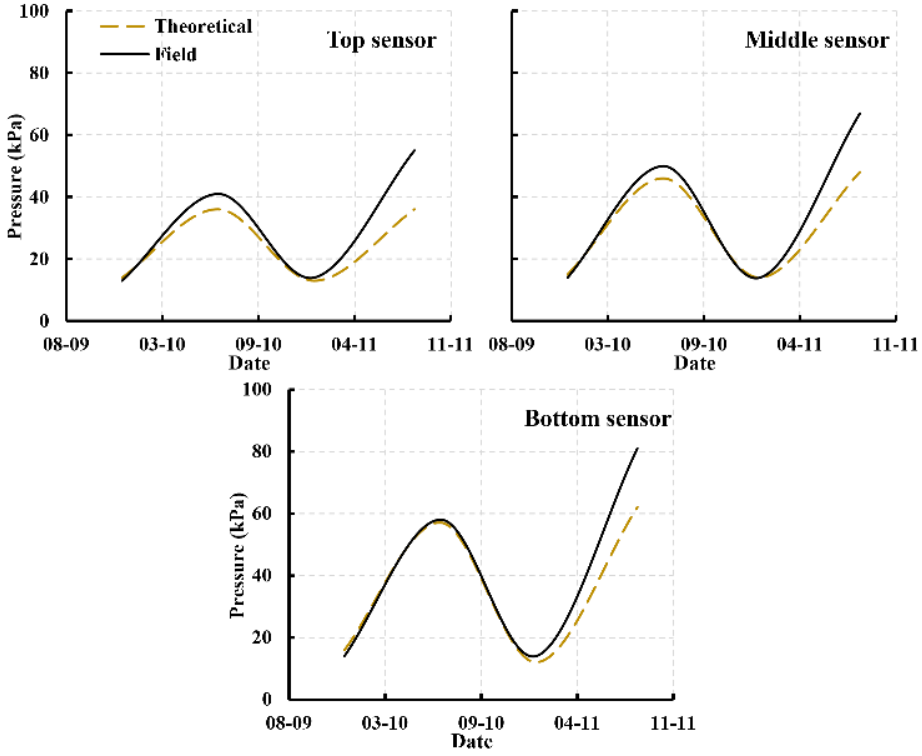

Figure 3.6 Comparison of lateral earth pressure curves obtained by utilizing theoretical methods and measured field data, for three sensor locations

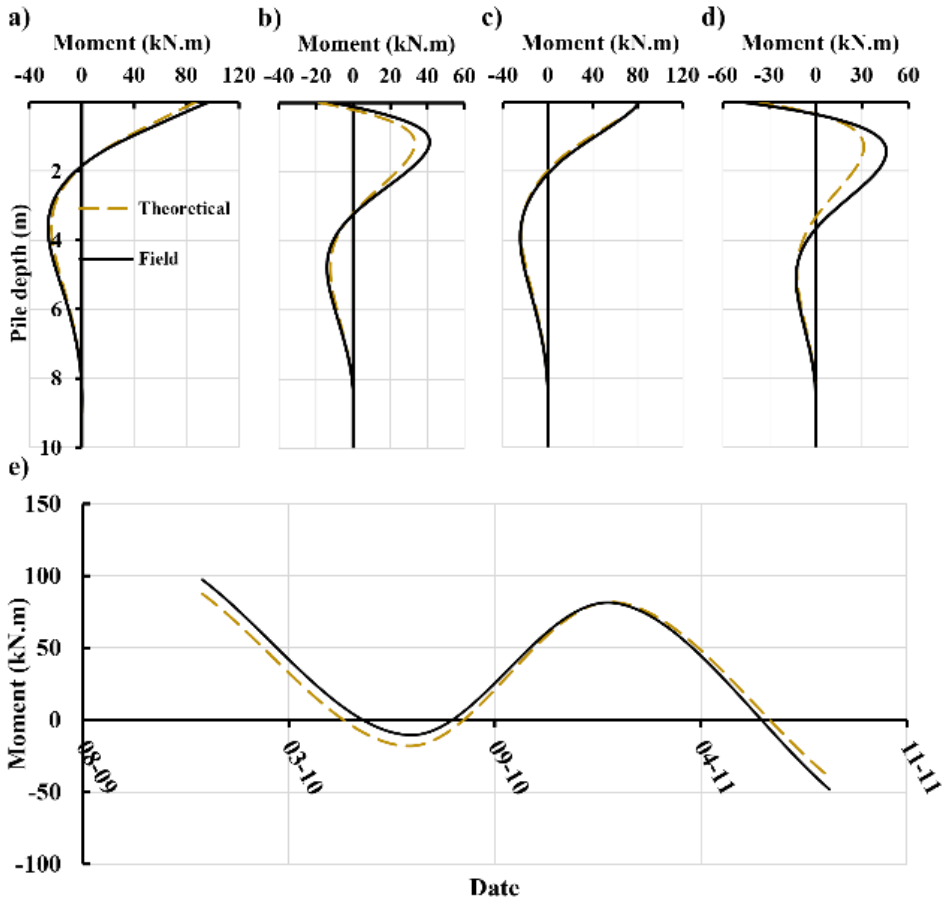

Figure 3.7 Comparison of pile bending moment profiles obtained by utilizing theoretical methods and measured field data, for: **(a)** 12/19/2009, **(b)** 07/07/2010, **(c)** 01/23/2011, **(d)** 08/20/2011, and **(e)** pile head bending moment variations with time

3.4.3 Results of parametric studies

This section presents findings of the parametric studies, which used the calibrated FE system to investigate the effects of varying the constitutive soil model, backfill stiffness, abutment concrete stiffness, pile size and orientation, and span length on IAB backfill stresses and pile bending moments.

3.4.3.1 Effect of constitutive soil model

Figure (3.8) compares the variations in backfill stresses obtained by utilizing the Mohr-Coulomb (MC) and hardening soil (HS) models, for three sensor locations. In the first and second contraction cycles, there is reasonable agreement between the MC and HS constitutive soil model results for active stresses at the top and middle sensor locations. However, for the bottom sensor location, the MC model overestimated the active pressures by 28.5% and 57% in the first and second contraction cycles, respectively. It can also be seen that the MC model underestimated the passive stresses at the top, middle, and bottom sensor locations. In the first expansion cycle, the MC model generated passive stresses that were 10% and 14% lower than those generated by the HS model for the top and middle sensor locations, respectively. Similarly, in the second expansion cycle, the MC model generated passive stresses that were 16%, 18%, and 10% lower than those generated by the HS model for the top, middle, and bottom sensor locations, respectively.

Figure (3.9) compares pile bending moment profiles obtained by utilizing the MC and HS constitutive soil models. As shown in Figure (3.9), in periods of contraction, utilization of the MC model for the subgrade soil had a negligible effect on the results obtained for the positive and negative bending moments. In contrast, in periods of expansion, use of the MC model resulted in decreased bending moments along the depth of the pile. Moreover, at the pile head, negative bending moments were generated by the HS model, whereas positive bending moments were generated by the MC model. In the first and second expansion cycles, the MC soil model also estimated points of inflection at shallower depths beneath the soil surface.

The significant variations in the results of the two soil models during passive cycles, illustrated in Figures (3.8) and (3.9), may be attributed to the elastic nature of the MC soil model. The MC model roughly mimics changes in soil stiffness for different stress levels and stress paths, provided that the local shear strength is not exceeded. This is due to the assumption of linear-elastic behavior (Hooke's law), which assumes that the elastic modulus of the soil (E) remains constant under applied stresses, if the failure contour is not reached. Therefore, with the MC soil model, plastic behavior occurs only at failure. This leads to inaccuracies, since soils experience plastic deformations that are dependent on the magnitude and path of the applied stress prior to failure (PLAXIS 2D manuals 2018).

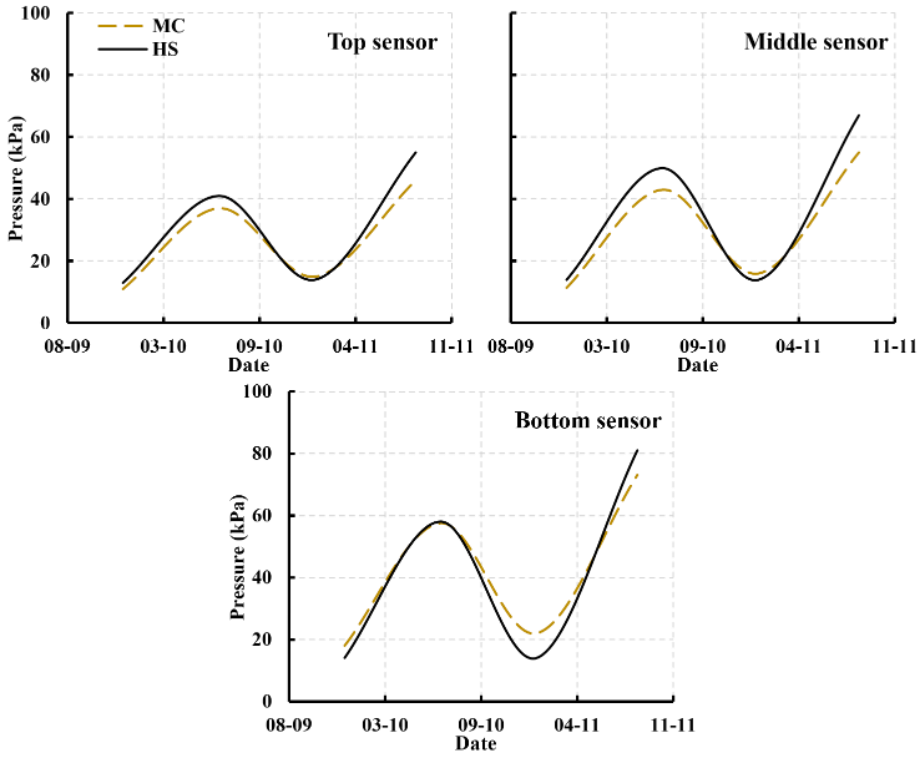

Figure 3.8 Comparison of lateral earth pressures in backfill soil obtained by utilizing the MC and HS soil models, for three sensor locations

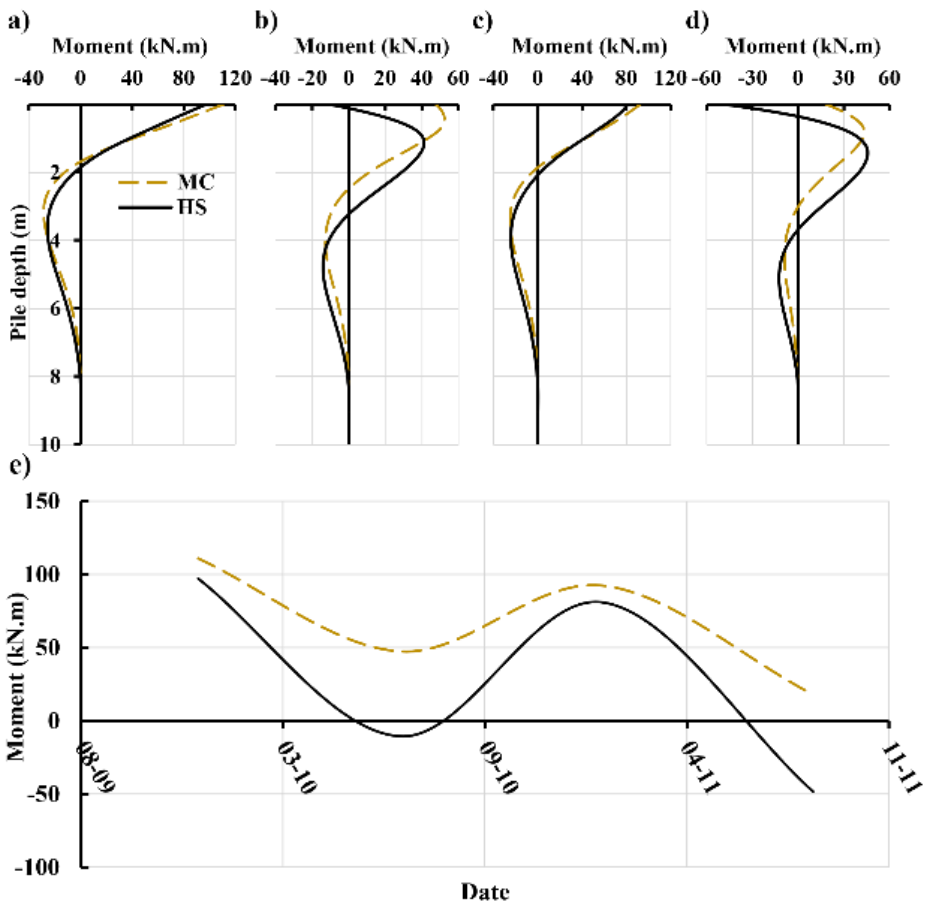

Figure 3.9 Comparison of pile bending moment profiles obtained by utilizing the MC and HS models for subgrade soil, at maximum and minimum temperatures, for: **(a)** 12/19/09, **(b)** 07/07/10, **(c)** 01/23/11, **(d)** 08/20/11, and **(e)** pile head bending moment variations with time

3.4.3.2 Effect of backfill stiffness

Figure (3.10) compares variations in earth pressure at three sensor locations, for four different backfill stiffnesses. As shown in Figure (3.10), earth pressures generated at the top, middle, and bottom sensor locations with different backfill stiffnesses followed a similar trend, where lateral stresses decreased during active states and increased during passive states. At all sensor locations, as backfill stiffness increased, insignificant changes

in the resultant active pressures occurred in periods of contraction. However, major discrepancies arose during periods of passive loading of the backfill soil. As stiffer backfill soils were used, the resultant passive stresses increased significantly at all sensor locations, particularly during the second expansion cycle. At the bottom sensor location, in the second expansion cycle, passive earth pressures ranged from 54 kPa for loose sand, to 235 kPa for gravel backfill. This corresponds to a 335% increase in passive stresses.

Figure (3.11) compares pile bending moment profiles obtained by utilizing four different backfill stiffnesses. As indicated in Figure (3.11), the pile bending moment profiles exhibited similar deformation patterns during periods of contraction. However, during periods of expansion, noticeable variations in the magnitude of maximum negative bending moments could be seen for different backfill stiffnesses. For example, as shown in Figure (3.11e), during periods of contraction, with abutment displacement away from the backfill, changes in the backfill stiffness had no significant impact on the bending moments. However, during periods of expansion, as the stiffness of the backfill soil increased, the magnitude of negative bending moments decreased, with positive bending moments developing for dense sand and gravel backfills during the first loading cycle. As shown in Figure (3.11e), in the first expansion cycle, the bending moments that developed at the pile head were -48 kN.m for loose sand and +14 kN.m for gravel backfill.

This behavior may be related to the force equilibrium between the bridge abutment and the backfill soil interface. As the bridge expands due to increasing temperatures, causing abutment displacement, a thermally induced horizontal force is transferred to the backfill soil and supporting piles. The ratio at which the applied force is distributed between the backfill soil and the piles is dependent upon their relative stiffness. A greater proportion of

the applied load will be borne by the component with a higher stiffness. Thus, during periods of thermally induced bridge expansion, increasing the stiffness of the backfill soil means that the backfill will bear some of the load previously borne by the foundation piles. This results in greater stresses in the backfill soil and smaller pile bending moments.

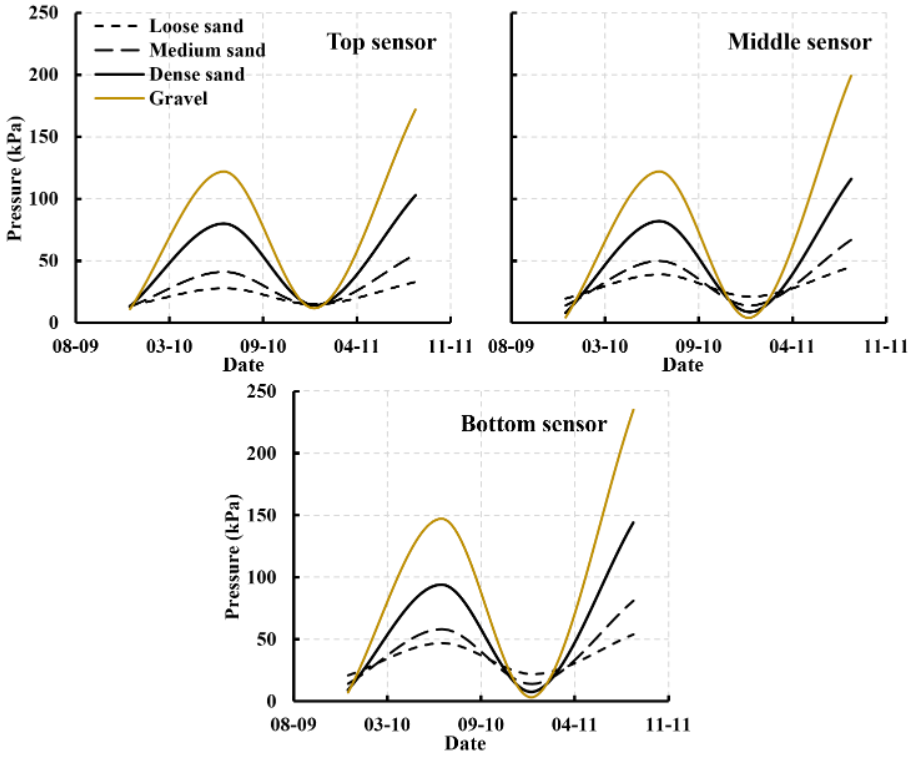

Figure 3.10 Comparison of lateral earth pressures calculated by utilizing four different backfill stiffnesses, from loose sand to gravel, for three sensor locations

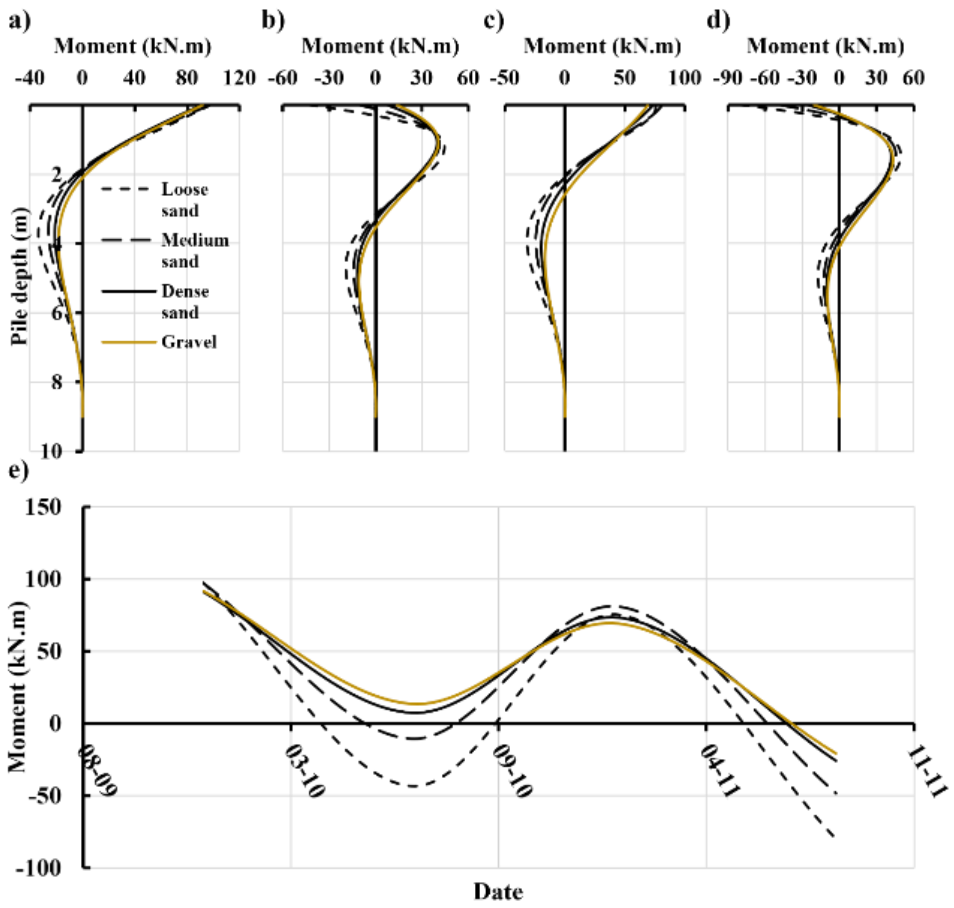

Figure 3.11 Comparison of pile bending moment profiles obtained by utilizing four different backfill stiffnesses, at maximum and minimum temperatures, for: **(a)** 12/19/09, **(b)** 07/07/10, **(c)** 01/23/11, **(d)** 08/20/11, and **(e)** pile head bending moment variations with time

3.4.3.3 Effect of concrete stiffness

Figure (3.12) compares variations in earth pressure at three sensor locations, for three different stiffnesses of abutment concrete. It can be seen that at all sensor locations, differences in concrete stiffness had no impact on earth pressure distributions in the active and passive states.

Figure (3.13) compares pile bending moment profiles obtained by utilizing three different stiffnesses of abutment concrete. Similarly to the earth pressure behavior described above, identical pile bending moment results were obtained when utilizing class A, class B, or class C concrete.

These results are due to the relative stiffnesses of the abutment concrete and the surrounding soil. In this study, the stiffness of the concrete materials used ranged from 21 GPa to 25 GPa, while the stiffnesses of the backfill and subgrade soils were 0.02 GPa and 0.05 GPa, respectively. Because of the extreme difference in the stiffness of the concrete and soil, a decrease of 4 GPa in the stiffness of the abutment concrete had no effect on the behavior of the surrounding soils. As a result, the magnitudes of the loads transferred by the abutment to the backfill soil and the subgrade piles remained basically unchanged.

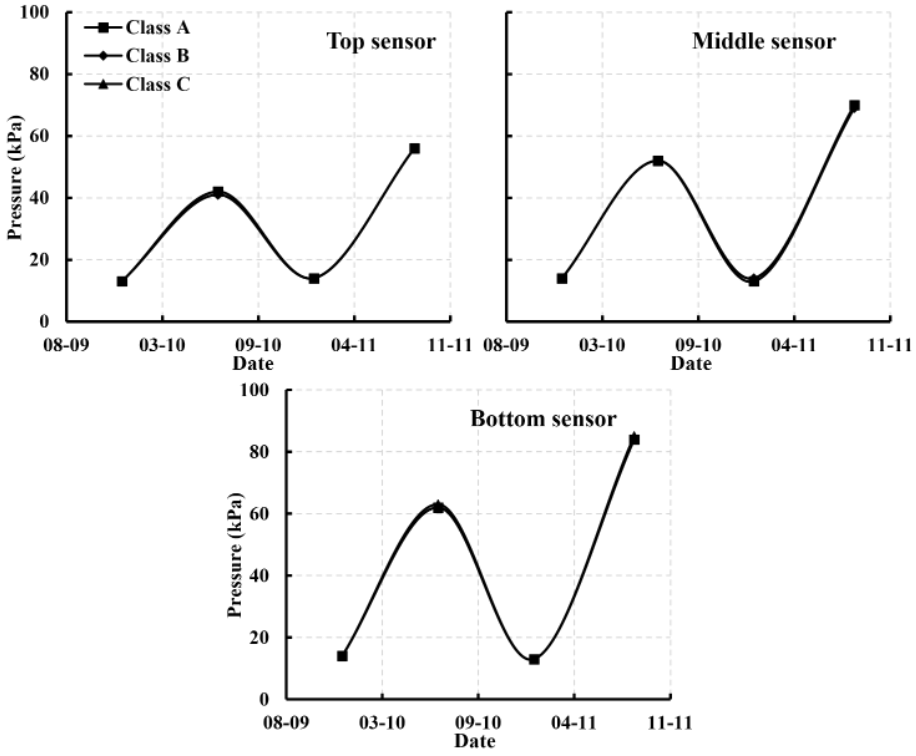

Figure 3.12 Comparison of lateral earth pressures obtained by utilizing three different stiffnesses of abutment concrete, for three sensor locations

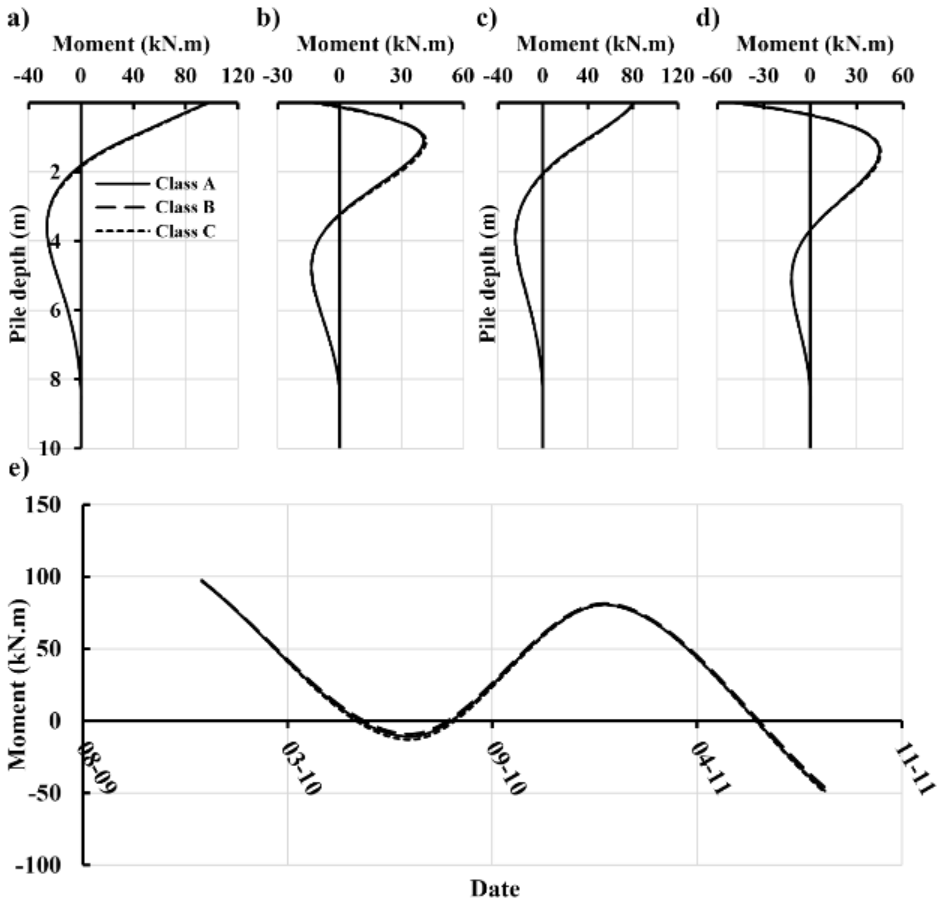

Figure 3.13 Comparison of pile bending moment profiles obtained by utilizing three different stiffnesses of abutment concrete, at maximum and minimum temperatures, for: **(a)** 12/19/09, **(b)** 07/07/10, **(c**) 01/23/11, **(d)** 08/20/11, and **(e)** pile head bending moment variations with time

3.4.3.4 Effect of pile size and orientation

Figure (3.14) compares variations in lateral earth pressures at three sensor locations, for piles with four different HP sections oriented for strong-axis bending. As the pile sections increased in size from HP 200 x 53 to HP 360 x 174, the corresponding active and passive stresses decreased at all three sensor locations. However, at the bottom sensor location, greater increases in the passive stresses were observed as pile sections decreased in size. For instance, in the first expansion cycle, at the bottom sensor location, passive stresses at

the backfill-abutment wall interface increased 15%, from 53 kPa for a HP 360 x 174 pile section to 61 kPa for a HP 200 x 53 pile section.

Figure (3.15) compares pile bending moment profiles obtained by utilizing piles with four different HP sections oriented for strong-axis bending. During bridge contractions and expansions, pile bending moment profiles exhibited similar patterns when different pile sections were used. However, Figure (3.15) shows that as the size of the pile sections increased, the magnitude of the positive and negative bending moments also increased. For example, when the pile section size was increased from HP 200 x 53 to HP 360 x 174, the magnitude of the pile head bending moments increased 150% in the first active cycle, and 168% in the second passive cycle. In addition, during bridge contractions and expansions, the size of the pile sections significantly influenced the depth at which inflection of the bending moments occurred. When larger pile sections were used, the inflection points occurred at much greater depths beneath the soil surface.

To show the effect of pile orientation, Figure (3.16) compares variations in lateral backfill stresses at three sensor locations, for piles with four different HP sections oriented for weak-axis bending. For a given pile section size, during bridge expansions, orientation for weak-axis bending resulted in larger stresses at the backfill-abutment interface than was the case with orientation for strong-axis bending. For example, as illustrated in Figures (3.14) and (3.16), a comparison of earth pressures obtained by utilizing an HP 200 x 53 section during the first passive cycle shows that changing the orientation from strong-axis to weak-axis bending increased the backfill stresses by 23%, 18%, and 21% at the top, middle, and bottom sensor locations, respectively.

Figure (3.17) compares pile bending moment profiles obtained by utilizing piles with four different HP sections oriented for weak-axis bending. In Figures (3.15) and (3.17), it can be seen that the use of smaller pile sections reduced the magnitude of positive and negative bending moments along the depth of the pile, in addition to causing bending moments to inflect at shallower depths beneath the soil surface. Furthermore, for a given pile section size, orientation for weak-axis bending reduced the magnitude of pile bending moments during bridge contractions and expansions. For example, for an HP 360 x 174 section, a comparison of Figures (3.15e) and (3.17e) shows that in the second active cycle, orientation for weak-axis bending decreased the pile head bending moment by approximately 18%.

The observed behaviors may be related to the force equilibrium between the bridge abutment and the supporting piles during thermally induced expansions and contractions. As the size of the pile section increases, the moment of inertia increases for both strong- and weak-axis orientations, thereby increasing rigidity. However, orienting piles for weak-axis bending significantly increases the flexibility of the bridge foundation. Backfill stresses were found to decrease as the stiffness of the piles increased, since a greater proportion of the induced load was transferred to the foundation piles, to maintain the force equilibrium. Similarly, since the load transferred to the piles is dependent on the pile rigidity, piles oriented for weak-axis bending were subject to smaller induced stresses. As a result, the corresponding pile bending moments were lower in piles oriented for weak-axis bending than in piles oriented for strong-axis bending.

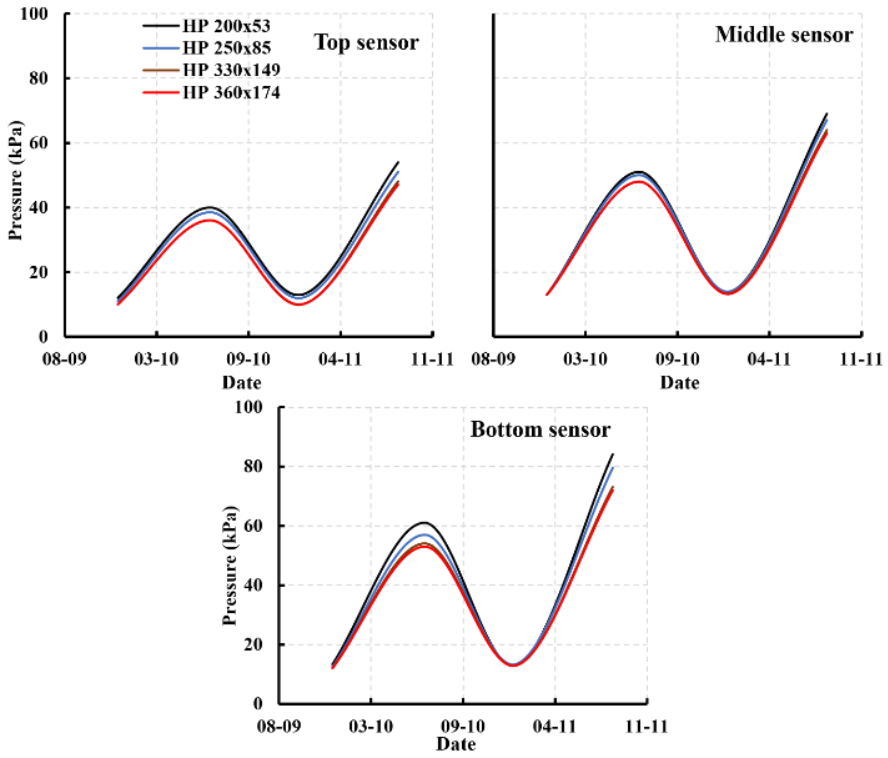

Figure 3.14 Comparison of lateral earth pressures obtained by utilizing four different HP pile sections oriented for strong-axis bending, for three sensor locations

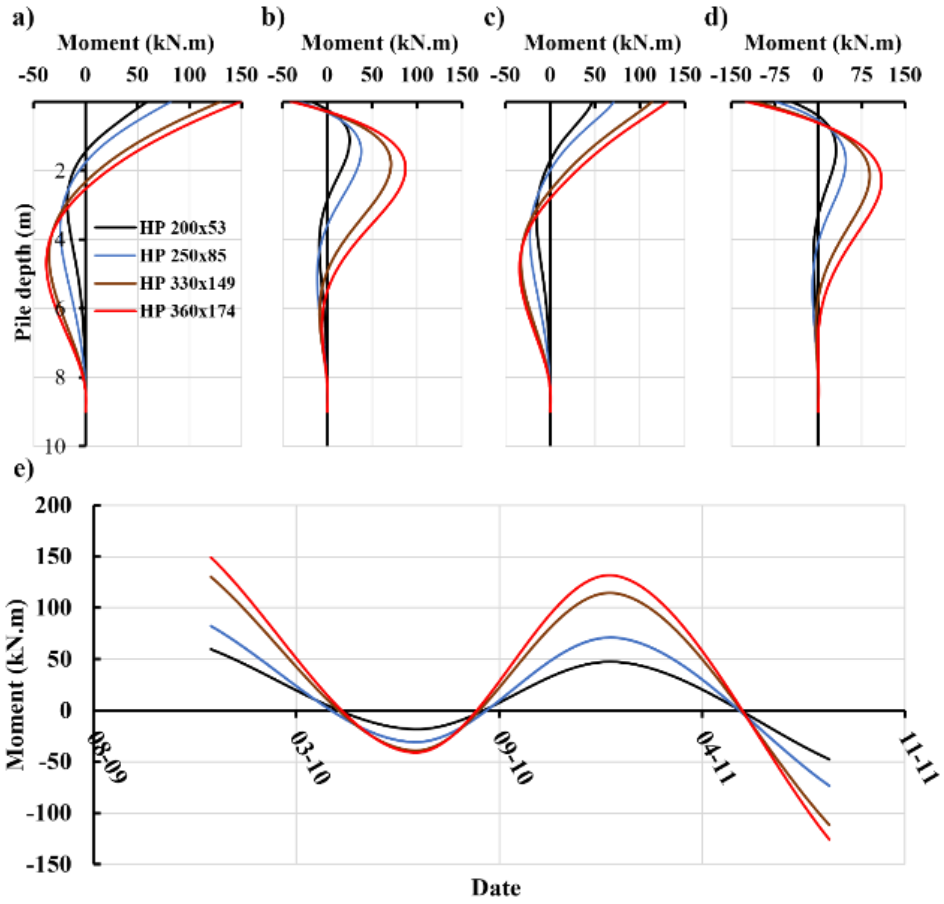

Figure 3.15 Comparison of pile bending moment profiles obtained by utilizing four different HP pile sections oriented for strong-axis bending, at maximum and minimum temperatures, for: **(a)** 12/19/09, **(b)** 07/07/10, **(c)** 01/23/11, **(d)** 08/20/11, and **(e)** pile head bending moment variations with time

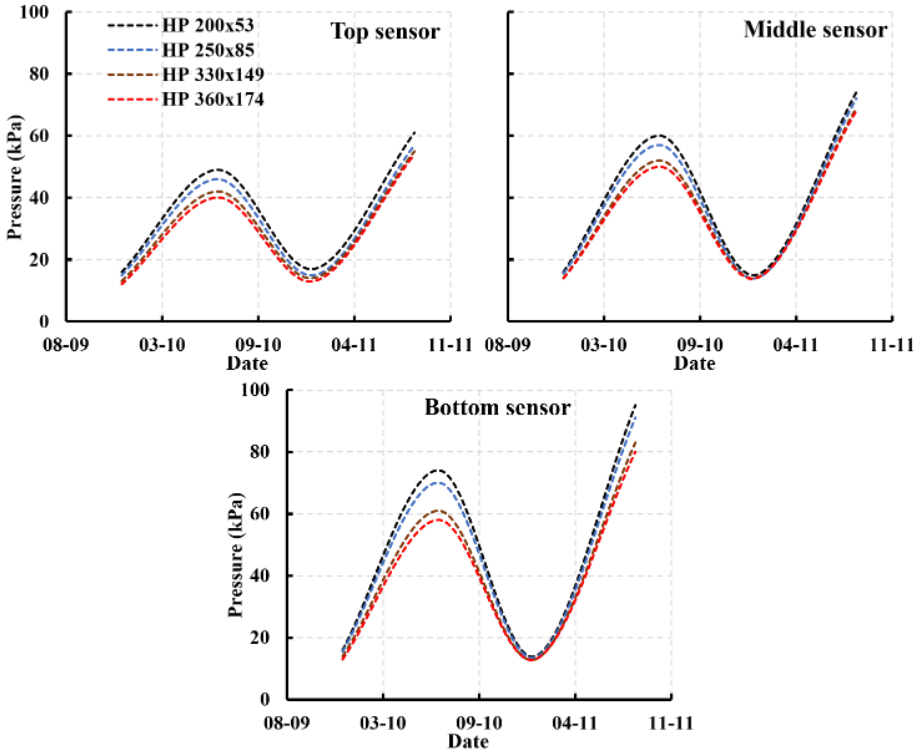

Figure 3.16 Comparison of lateral earth pressures obtained by utilizing four different HP pile sections oriented for weak-axis bending, for three sensor locations

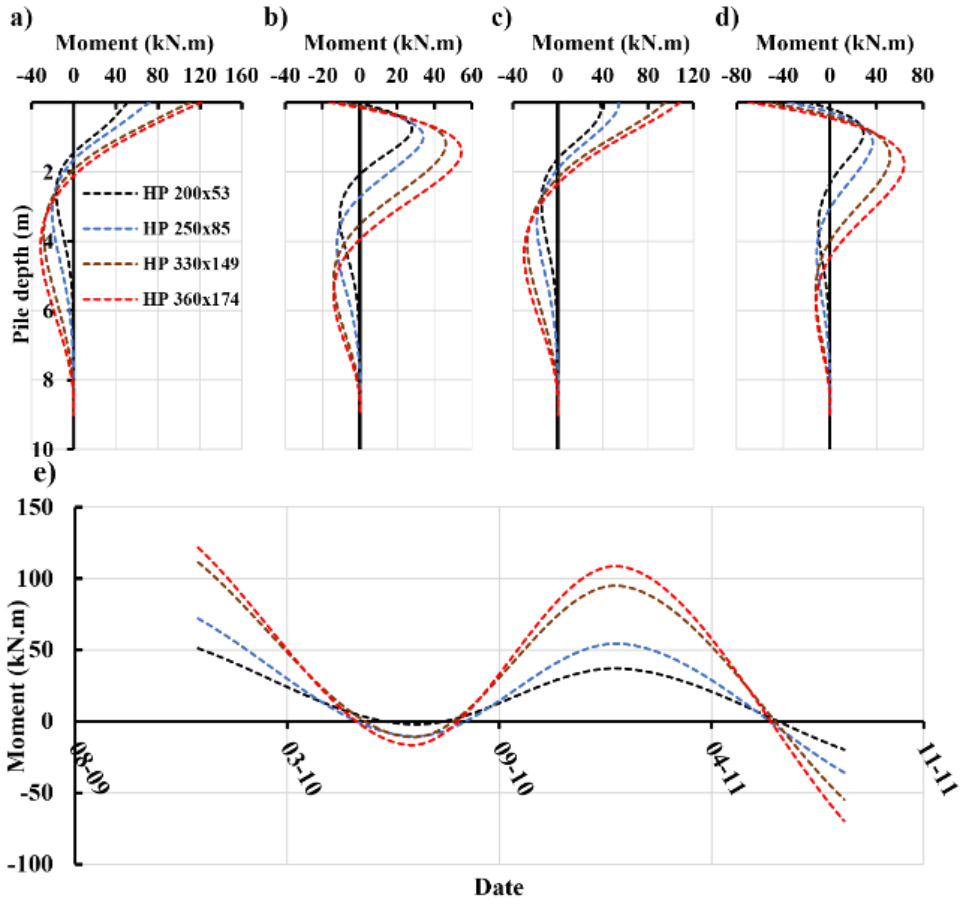

Figure 3.17 Comparison of pile bending moment profiles obtained by utilizing four different HP pile sections oriented for weak-axis bending, at maximum and minimum temperatures, for: **(a)** 12/19/09, **(b)** 07/07/10, **(c)** 01/23/11, **(d)** 08/20/11, and **(e)** pile head bending moment variations with time

3.4.3.5 Effect of span length

Figure (3.18) compares variations in backfill stresses at three sensor locations for five different span lengths, with the number of spans ranging from 1 to 5. It can be seen that as the number of spans increased, the resultant stresses during the active and passive states decreased. When the number of spans was varied between two and five, during bridge contractions and expansions, minimal changes were seen in the backfill stresses at the top,

middle, and bottom sensor locations. However, as shown in Figure (3.18), there was a significant difference in the results obtained when a single span was used. The greatest variation in the results was seen at the bottom sensor location, where reducing the number of spans from two to one increased the passive stresses by 52% during the first expansion cycle and 36% during the second expansion cycle.

Figure (3.19) compares the pile bending moment profiles obtained by varying the number of bridge spans from one to five, with corresponding variations in the span length. As shown in Figures (3.19b) and (3.19d), in periods of expansion, with abutment displacement toward the backfill soil, bending moment patterns were similar for all span lengths. During the two expansion cycles, utilizing a single span increased the magnitude of the maximum negative and positive bending moments, but did not affect the depth at which bending moment inflections occurred. Figure (3.19e) illustrates that reducing the number of spans to one increased the magnitude of the maximum negative bending moments by an average of 83% and 49% during the first and second expansion periods, respectively. During periods of contraction, similar pile bending moment patterns were observed when two, three, four, or five spans were used. However, reducing the number of spans to one resulted in significant changes in the pile bending moment patterns and magnitudes. As shown in Figures (3.19a) and (3.19c), for a single span, during contraction cycles, the variation in positive pile bending moments with depth is nonlinear. For example, Figure (3.19c) illustrates that for a single span, the maximum positive pile bending moment occurred at about 0.6 m below the base of the abutment, rather than at the pile head. It can also be seen that reducing the number of spans to one increased the depth of the point of inflection by 0.5 m in Figure (3.19a) and 1 m in Figure (3.19c).

Increases in backfill stresses as fewer bridge spans were utilized may be related to vertical stresses in the backfill soil immediately following bridge construction. Before the bridge is subject to thermally induced contractions and expansions, dead loads resulting from the self-weight of the deck and girder components increase the vertical stresses in the backfill, since the approach slab is rigidly connected to the abutment. This also increases the corresponding lateral earth pressures, as they are a function of the vertical stress and the coefficient of lateral earth pressure.

Furthermore, increases in pile bending moments may be associated with the extent of induced secondary moments (p-Δ effect). As the pile deflects into an active or passive position, a secondary moment is induced as a function of the vertical load and the eccentricity (the contracted/expanded distance). Thus, as the magnitude of the vertical force increases, the corresponding secondary and total moments increase accordingly.

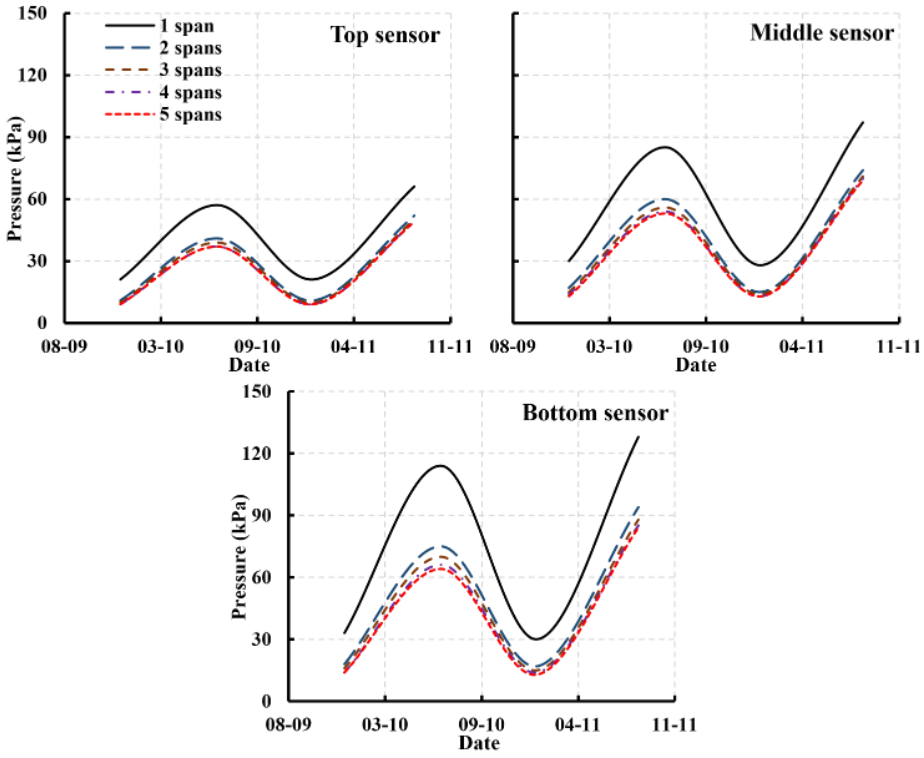

Figure 3.18 Comparison of lateral earth pressures obtained by utilizing five different span lengths (with the number of spans ranging from 1 to 5), for three sensor locations

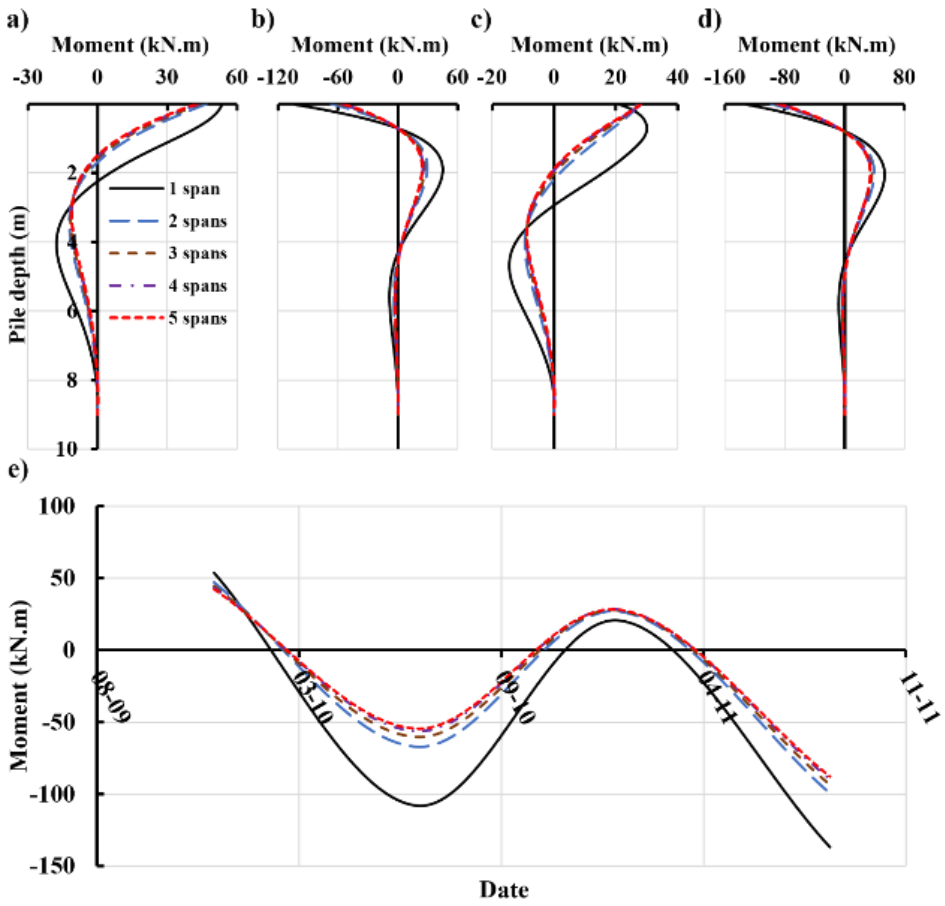

Figure 3.19 Comparison of pile bending moment profiles obtained by utilizing five different span lengths, at maximum and minimum temperatures, for: **(a)** 12/19/09, **(b)** 07/07/10, **(c)** 01/23/11, **(d)** 08/20/11, and **(e)** pile head bending moment variations with time

3.5 Summary and Conclusions

This paper first presented findings based on full-scale monitoring of the thermal response of the Middlesex bridge in Vermont, USA. This was followed by a description of the calibration of a two-dimensional FE model developed to mimic the full-scale SSIs, with verification of the model results against measured backfill stresses and pile bending

moments. Details of modelling thermally induced loading in the absence of full-scale measured data were then described together with the corresponding findings. A comprehensive parametric study was carried out to investigate the impact of varying the constitutive soil model, backfill stiffness, abutment stiffness, pile size and orientation, and span length on the thermal response of IABs. Based on the results of this study, the following conclusions can be drawn:

1. The calibrated FE system was shown to simulate the observed thermal response of the Middlesex bridge accurately. The earth pressures and pile bending moments obtained by the FE model closely adhered to those measured in the field.
2. For the two-year monitoring period, Eq. 1 reasonably approximated bridge contractions and expansions, except in the case of the second expansion cycle. In the second expansion cycle, the bridge was observed to undergo time-dependent effects, where a movement toward the backfill was seen. Because of the linear relationship between the induced displacement and changes in temperature assumed by Eq. 1, this equation does not consider time-dependent effects. Therefore, the calculated displacement was 10 mm less than the value measured in the field. As a result, the corresponding earth pressures and pile bending moments obtained were significantly lower than those measured in the field.
3. The constitutive soil models employed strongly influenced the accuracy and reliability of the results. In contrast to the MC soil model, the HS soil model exhibited enhanced capabilities for simulating the nonlinearity of the soils, particularly during periods of bridge expansion. As shown in Figure (3.8), the resultant passive pressures obtained when modelling the backfill soil were lower when the MC constitutive soil model was

used than when the HS model was used. Similarly, as shown in Figures (3.9b) and (3.9d), the bending moments obtained at the pile head were positive when the MC model was used to model the subgrade soil, but negative when the HS model was used.

4. Changing the stiffness of the backfill soil was found to impact the thermal response of IABs only during periods of expansion. Increasing the stiffness of the supporting backfill significantly increased the earth pressure during passive phases. It was also observed that stiffer backfill soils reduced bending moments in the foundation piles during passive cycles. This is because bridge contractions are influenced only by the restraints provided by the subgrade soil, while bridge expansions are influenced primarily by the backfill conditions.
5. Varying the stiffness of the abutment was found to have no effect on the earth pressures in the backfill soil or on the bending moments in the supporting piles, due to the significant difference in relative stiffness between the abutment concrete and the surrounding soils.
6. The size and orientation of the pile sections directly impacted the flexibility of the foundation piles. With decreasing pile section size, and orientation for weak-axis bending, the corresponding bending rigidities decreased significantly. Reducing the bending rigidity of the piles significantly increased the effect of corresponding contractions and expansions. Thus, it was found that using smaller pile sections oriented for weak-axis bending resulted in increased earth pressures and decreased pile bending moments.

The vertical load applied at the abutment end is directly linked to the number of bridge spans, where the magnitude of the applied load increases as the number of spans decreases.

Backfill stresses were found to increase as the magnitudes of vertical loads increased. This is because increasing the applied vertical load increases the vertical stresses in the backfill soil. In turn, this results in increased horizontal stresses within the backfill soil, since horizontal stresses are the product of vertical stresses and the coefficient of lateral earth pressure. Furthermore, pile moments were found to increase as the number of bridge spans decreased. This may be related to the additional induced moment due to p-Δ effects. As the value of p increases, the corresponding moment increases accordingly.

References

Arsoy, S., Barker, R. M. & Duncan, J. M., 1999. The Behavior of Integral Abutment Bridges, Virginia: Virginia Transportation Research Council.

Bonczar, C., Civjan, S., Breña, S., DeJong, J., (2005). Behavior of Integral Abutment Bridges: Field Data and Computer Modeling, Amherst: Federal Highway Administration.

Breña, S.F., Bonczar, C.H., Civjan, S.A., DeJong, J.T., Crovo, D.S., (2007). Evaluation of Seasonal and Yearly Behavior of an Integral Abutment Bridge. *Journal of Bridge Engineering*, 12(3), 296-305.https://doi.org/10.1061/(ASCE)1084-0702(2007)12:3(296)

Civjan, S. A., Kalayci, E., Quinn, B. H., Breña, S. F., & Allen, C. A. (2013). Observed integral abutment bridge substructure response. *Engineering Structures,* 56, 1177-1191. ISSN 0141-0296, https://doi.org/10.1016/j.engstruct.2013.06.029.

Civjan, S.A., Bonczar, C., Breña, S.F., DeJong, J., Crovo, D., (2007). Integral Abutment Bridge Behavior: Parametric Analysis of a Massachusetts Bridge. *Journal of Bridge Engineering,* 12(1), 64-71. https://doi.org/10.1061/(ASCE)1084-0702(2007)12:1(64)

Duncan, J.M., Chang, C.Y., (1970). Nonlinear Analysis of Stress and Strain in Soils. *Journal of the Soil Mechanics and Foundations Division*, 96(5), https://doi.org/10.1061/JSFEAQ.0001458

El Naggar, H., Mahgoub, A., Duguay, F., and Valsankgar, A. (2016). Impact of the Employed Soil Model on the Predicted Behaviour of Integral Abutment Bridges. *Proceedings of the 69th Canadian Geotechnical Conference*, Vancouver, Canada

Hibbeler, R. C., (2014). Mechanics of Materials. 9th ed. Upper Saddle River: Pearson Prentice Hall.

Hoppe, E.J. and Gomez, J.P. (1996). Field study of an integral backwall bridge, Virginia Transportation Research Council, VTRC 97-R7, October 1996, 47 p.

Huang, J., Shield, C., French, C., (2011). Behavior of an Integral Abutment Bridge in Minnesota, US. *Structural Engineering International*, 21(3), 320-331, https://doi.org/10.2749/101686611X12994961034336

Huntley, S.A. and Valsangkar, A.J., (2013). Field monitoring of earth pressures on integral bridge abutments. *Canadian Geotechnical Journal*, 50(8), 841-857. https://doi.org/10.1139/cgj-2012-0440

Huntley, S.A. and Valsangkar, A.J., (2014). Behavior of H-piles supporting an integral abutment bridge. *Canadian Geotechnical Journal*, 51(7), 713-734. https://doi.org/10.1139/cgj-2013-0254

Kalayci, E. (2012). *Performance monitoring and analysis of Integral Abutment Bridges* (Publication No. 3545945) [Doctoral dissertation, University of Massachusetts Amherst]. ProQuest Dissertations Publishing.

Kim, W., & Laman, J.A., (2010). Integral abutment bridge response under thermal loading. *Engineering Structures*, 32(6), 1495-1508. https://doi.org/10.1016/j.engstruct.2010.01.004.

Kong, B., Cai, C.S., Zhang, Y., (2016). Parametric study of an Integral abutment bridge supported by prestressed precast concrete piles. *Engineering Structures*, 120, 37-48. https://doi.org/10.1016/j.engstruct.2016.04.034

LaFave, J.M., Brambila, G., Kode, U., Liu, G., Fahnestock, L.A., (2021). Field Behavior of Integral Abutment Bridges under Thermal Loading. *Journal of Bridge Engineering,* 26(4). https://doi.org/10.1061/(ASCE)BE.1943-5592.0001677

Mahgoub, A. and El Naggar, H., (2020). Innovative Application of Tire-Derived Aggregate around Corrugated Steel Plate Culverts. *Journal of Pipeline Systems Engineering and Practic*, 11(3).https://doi.org/10.1061/(ASCE)PS.1949-1204.0000466

PLAXIS 2D manuals (2018).

Sluis, J., Besseling, F., Stuurwold, P., Lengkeek, A., (2014). *Validation and Application of the Embedded Pile Row Feature in PLAXIS 2D*. Witteveen+Bos, The Netherlands

Zakhem, A.M. and El Naggar, H., (2019) Effect of the constitutive material model employed on predictions of the behaviour of earth balance (EFB) shield-driven tunnels. *Transportation Geotechnics*, 21. https://doi.org/10.1016/j.trgeo.2019.100264

CHAPTER 4 THREE – DIMENSIONAL MODELLING OF INTEGRAL ABUTMENT BRIDGES

Ahmed Abdullah and Hany El Naggar

4.1 Introduction

Integral abutment bridges (IABs) were first designed around the 1930's in the aim to replace jointed bridges (Kong et al. 2016). These structures became rapidly widespread after the early 1960's owing to their favorable attributes (Arsoy et al. 1999). As Canada slowly began integrating the use of IABs during the 1960's, it was reported by the Ministry of Transportation of Ontario (MTO) that over 100 IABs were constructed by the early 1990's (Husain and Bagnariol 2000).

These structures are distinguished by eliminating the necessities of bearing and expansion joints, and thus monolithically casting the deck and girders with the abutments (Abdel-Fattah et al. 2018). This integral assembly between the superstructure and substructure corresponds to a continuously rigid structure. IABs constructed within the US utilize a single row of vertical piles oriented for weak axis bending to support stub-type abutments (Arockiasamy et al. 2004). However, the substructure of IABs built in the UK are comprised of flexible abutments with shallow foundations (Caristo et al. 2018). Converse to conventional bridges, IABs are associated with simpler designs and analysis methods due to the elimination of expansion and bearing joints. These structures have shown enhanced resisting capabilities against longitudinal pavement pressures, since the induced compressive stresses are distributed over a greater area. Furthermore, because of their simple design and small number of structural members, IABs have been associated with

quicker construction times. As IABs provide greater resistance against uplift forces due to the self-weight of the structural members, broader spans are achievable. In addition, the monolithic nature of the superstructure provides a greater area for the distribution of vehicle loads, thus reducing service and impact stresses within the superstructure (Burke 1993). Research conducted by Yang et al. (Yang et al. 1985) indicated that the elimination of expansion and bearing joints reduced construction and maintenance costs. A report prepared by Arsoy et al. (Arsoy et al. 1999) specified that constructing IABs permits for larger end span ratios and was found to improve the riding quality due to their continuous nature. Finally, Hoppe and Gomez (Hoppe and Gomez 1996) have suggested that IABs have shown enhanced seismic performances compared to conventional bridges.

The complex soil-structure interactions (SSIs) of IABs in response to cyclic thermal loadings are yet to be fully understood due their relatively recent introduction. However, by utilizing the finite element method (FEM), researchers are able to perform numerical analyses to investigate the impact of parameter variations on the thermal response of IABs. Hence, this has led researchers to conduct full-scale monitoring programs and numerical research to better understand the changes in performance of IABs when subjected to cyclic thermal loadings. Ooi et al. (Ooi et al. 2010) monitored the thermal response of the Kii bridge in Hawaii over a 45-month period. It was found that the drilled shaft foundations deviated towards the stream after backfilling the abutment with controlled-low strength material (CLSM) and well-graded gravel, providing evidence of deep seated movements. The Kii bridge was observed to undergo time-dependent effects causing irreversible abutment movements towards the stream, and therefore decreasing the corresponding passive and active pressures. Induced daily thermal displacements of the abutments were

significantly influenced by the degree of exposure to solar-radiation, where abutments exposed to solar-radiation were observed to experience larger displacements. The seasonal movements of short spanned IABs located in tropical areas were found to be governed by stream induced loadings rather than temperature induced loadings. Instrumented strain gages and tilt meters provided evidence of abutment translation and rotation. It was seen that the redistribution of dead loads among the drilled pile shafts due to induced non-uniform solar-radiation deformations caused the internal forces within the superstructure to fluctuate with time. In accordance with measured strain gage data, bending moments within the drilled shafts under induced stream and thermal loadings were found to be less than the cracking moment. Ooi et al. (Ooi et al. 2010b) continued research investigations on the Kii bridge by conducting numerical studies via calibrated 2D and 3D FE models, where various key model parameters were varied. In the event of deep seated soil movements, it was found that pile curvatures obtained using the 3D model were larger than 2D pile curvatures. In comparison, using a 3D model yielded to larger maximum negative bending moments at the pile head, while 2D results indicated that the maximum negative bending moment occurs at a depth below the base of the abutment. It was concluded that realistic abutment translations and rotations under induced thermal contractions and expansions were captured by defining prescribed loads at the top and bottom of the bridge superstructure. Stream loadings on the abutment were numerically simulated by varying the stream elevations during wet and dry seasons. While raising the elevation of the stream caused the abutment and drilled shaft to further displace into the backfill soil, the corresponding passive earth pressures remained unchanged. A significant increase in agreement was seen when obtained FE pile axial forces were compared to corrected field

measured pile axial force in contrast to uncorrected field results. Fennema et al. (Fennema et al. 2005) investigated the thermal performance of an IAB located in Pennsylvania, USA, by conducting a full-scale monitoring program using 64 gages over a period of four months. In addition, utilizing calibrated 2D and 3D FE models, numerical studies were conducted to evaluate the validity of existing methods used to predict the behavior of IABs in response to induced cyclic thermal loading. It was concluded that using the *p-y* method to simulate the SSI of IABs is a valid approach due to its simplicity and efficiency. Furthermore, it was found that the using 2D models to predict the behavior of IABs is sufficient, since obtained pile deformations using 2D and 3D models agreed reasonably well. Converse to design assumptions, it was found that the abutment accommodated induced thermal movements primarily via rotations instead of lateral translations. Based on measured girder-abutment rotation data, the connection between the girder and the abutment was concluded to be a hinged connection, since the rotations exhibited by the girders and the abutments were opposite. The magnitude of axial forces within the bridge girders were found to be influenced by the positioning of the girder, stiffness of the backfill soil in periods of expansion, and extent of creep and shrinkage effects. In addition, significant tensile stresses were observed to develop within the girders under the design temperature, and hence was recommended to be considered during design. Quinn and Civjan (Quinn and Civjan 2017) conducted parametric studies using 3D FE models on a design IABs in accordance with Vermont and Massachusetts design guidelines, USA. It was observed that pile orientation had negligible impacts on the longitudinal displacements and rotation of the bridge abutment. However, it was seen to significantly impact the transverse displacements of the abutments. For abutments with 0^o skew, orienting piles for

weak-axis bending resulted in lower pile moments, while strong-axis bending reduced the percentage of the pile yielding moment. However, for skewed abutments, it was indicated that pile moments were critical for weak axis bending. In addition, significant transverse displacements occurred within piles oriented about weak axis and strong axis bending because of the plane rotation of the skewed abutment. Furthermore, in the presence of backfill soil, critical pile moments were seen to develop at obtuse and acute corners during expansion and contraction, respectively. However, pile moments at the obtuse and acute corners under induced expansions and contractions were similar in the absence of backfill soil. Research conducted by Kim and Laman (Kim and Laman 2010) involved performing numerical analyses using calibrated FE 2D models to study the short-tern thermal response of IABs when key parameters were varied. It was observed that as the length of the bridge increased, the lateral displacement and moment within the piles increased. However, negative moments within the girders were seen to decrease as the bridge length increased. Variations in backfill height and stiffness were not seen to impact the structural performance of the girders and piles. As the stiffness of the pile soil increased, girder and pile moments were seen to increase, however, displacements at the pile head were found to decrease. Kim and Laman (Kim and Laman 2012) then built upon previous research by conducting full-scale monitoring programs of four IABs in Pennsylvania, USA, to study the long-term performance of IABs under cyclic thermal loading. Over the course of the monitoring period, it was observed that all IABs exhibited irreversible inward movements with each loading cycle. With time, it was observed that the variation in earth pressures at the top and bottom of the abutment decreased. Measured field data indicated that differential rotation occurred between the abutment and girders at the construction joint

location. In addition, girders developed positive and negative bending moments during induced contractions and expansions, respectively. Finally, based on monitored data, live plus impact loads due to the ongoing vehicles strongly influenced the performance of the bridge.

In the literature, most previous research analyzes the complex SSIs of IABs under the influence of temperature driven loads via the beam-spring approach. This method idealizes structural components via linear-elastic finite beam elements in accordance with the Lagrangian formulation, discretized at n intervals with corresponding node endings. The soil medium is modelled using one-dimensional linear/nonlinear horizontal and vertical Winkler springs connected incrementally to the node endings of the beam elements (Greimann et al. 1986). The stiffness (k_h) of the soil sprigs are characterized through load-deflection ($p - y$) curves based on full-scale load tests. Utilizing such an approach only computes internal forces within the structural members and springs as well as displacements at the specified node endings (Coduto 2001). However, as opposed to the continuum nature of soils, this approach gives rise to significant discontinuities. Furthermore, conditions such as drainage, pore water pressures, and soil boundaries are not captured (Dhadse et al. 2021). Greimann et al. (Greimann et al. 1986) indicated that by utilizing the beam-spring approach, torsional resistance provided by the surrounding soil is neglected. Furthermore, the deformation of a single soil spring at a certain depth is independent of the neighboring springs. Finally, the axial and lateral response of the soil springs to applied stresses are independent. Thus, this study aims to build on previous research by modelling the complex SSIs of IABs in response to cyclic thermal loading as a full continuum, utilizing interface elements between discontinuous materials. This

corresponds to a more realistic representation of the relative deformation and stress transfer between structural elements and the surrounding soil over the entire depth. The stress-strain response of soil can be defined using advanced constitutive soil models which consider nonlinear behaviors such as stiffness-stress dependency, variations in soil stiffness during unloading/reloading, time-dependent effects, and strain hardening/softening (Dhadse et al. 2021; PLAXIS 3D manuals 2018).

In accordance with Kalayci (Kalayci 2012), this paper will first provide details related to the selected case study bridge along with the corresponding full-scale monitoring program, instrumentation, construction sequence, and acquired monitored data over a two-year period. Specifics concerning the development and verification of a calibrated three-dimensional finite-element model using PLAXIS 3D against field monitored data are then presented. Finally, utilizing the calibrated FE model, a detailed description will be presented of the conducted parametric studies to investigate the impact of varying the backfill stiffness, pile size and orientation, abutment stiffness, and the constitutive soil model on the corresponding lateral earth stresses and pile bending moments under induced cyclic thermal loading.

4.2 Bridge description

The IAB analyzed in this paper is located on route VT12 over Martin's Brook in Vermont, USA. Starting on mid-June 2009, the construction of the Middlesex bridge commenced over a duration of four and a half months. Around late October 2009, the bridge was opened for traffic. Table (4.1) highlights the starting dates of the key construction activities.

The Middlesex bridge is a straight bridge with a single span of 43 m from bearing to bearing. The 4 m high abutments incorporate a 1 m thickness and extend 10.2 m in the out-of-plane direction. The abutment diaphragm and pile cap are connected via a construction joint to facilitate a rigid connection. Five grade 345W steel plate girders, equally spaced at 2.05 m are embedded and anchor bolted into the abutment diaphragms. The girders support a reinforced concrete (RC) deck with a thickness of 0.22 m. Each abutment is supported by five grade 345 steel HP 310 x 125 piles equally spaced at 2.05 m. To ensure fixed head conditions, piles are embedded 1 m into the pile cap. Each pile is driven 9 m into the in-situ soil to satisfy adequate bearing capacity requirements. A RC approach slab with a length of 6 m and a thickness of 0.38 m was casted integrally with the abutment diaphragm back wall. Each abutment comprises of two 0.45 m thick perpendicular wing walls, extending 3 m behind the abutment back wall. The bridge schematics are shown in Figure (4.1).

In-situ and backfill soils were classified as cohesionless and compacted granular medium dense sand, respectively, according to geotechnical reports prepared by the Vermont Agency of Transportation (VTrans). Having a slope of 1V:1.5H, the stratigraphy of the in-situ soil consisted of a 1.5 m thick layer of compacted medium dense sand, overlaying a 10 m thick layer of medium dense sand and silty sands with some gravel, before reaching bedrock. The ground water table was encountered at the base of the abutment according to ground water investigations.

Table 5 Middlesex bridge construction sequence (Kalayci 2012)

Construction activity	Starting date (mm/dd/yyyy)
Pile driving	06/15/2009
Pouring of pile cap and lower wing wall	07/15/2009
Backfilling of pile cap soil	07/22/2009
Girder placement	07/22/2009
Placement of deck	08/27/2009
Pouring of upper abutment and wing wall	09/21/2009
Backfilling of upper abutment	10/07/2009
Placement of approach slab	10/09/2009

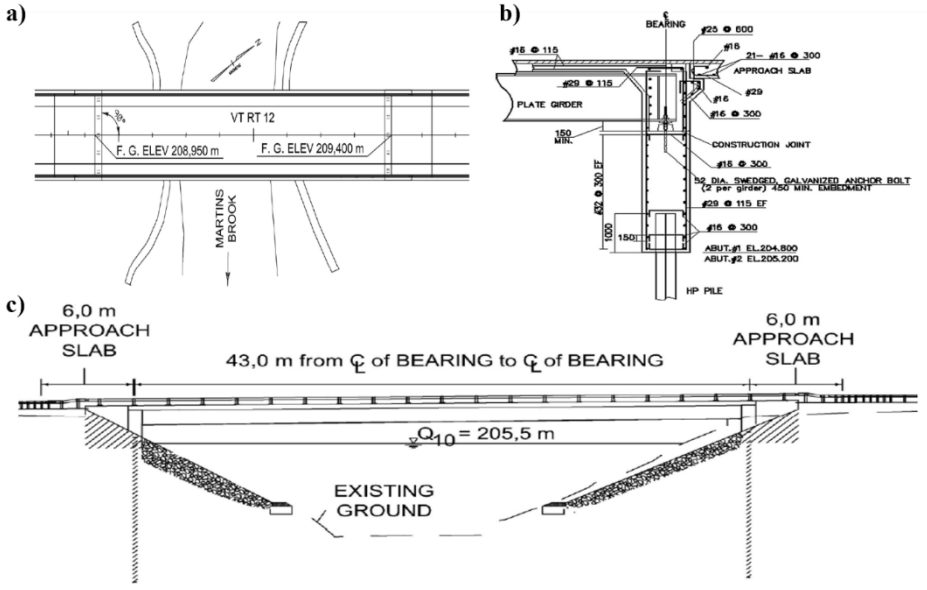

Figure 4.1 Bridge: **(a)** Plan view, **(b)** abutment cross-section, and (**c)** elevation view (Civjan et al. 2013)

4.2.1 Bridge instrumentation

The full-scale monitoring objectives for abutments 1 and 2 were to measure the passive and active earth pressure distributions at the abutments and wing walls, lateral and longitudinal displacements of the abutments, rotation of the abutments, pile strains, and

girder strains over a period of two-years after the end of construction. However, field acquired data corresponding to the variations in lateral earth stresses in the backfill and pile strains at abutment 1 were the primary focus of this paper. Extensive details related to the full-scale instrumentation and monitored data can be found in Kalayci (Kalayci 2012). Bridge deformations were monitored via vibrating-wire (VW) Geokon gages and multiplexers, while utilizing Campbell Scientific CR1000 and CR10X data loggers for data acquisition every six hours. As a result of electrical storms causing instrumental malfunctions, data were not collected between April 20, 2011, and May 13, 2011. The instrumentation plan of the Middlesex bridge is shown in Figure (4.2).

Earth pressure distributions at the abutment-backfill interface were monitored using seven Geokon 4815 pressure cells (PC). As shown in Figure (4.2), PCs were instrumented at three various elevations and widths beneath the diaphragm-pile cap construction joint. Each PC consisted of two components: **(1)** a transducer housing; **(2)** a circular pressure cell. Prior to backfilling, PCs were nailed onto the pile-cap formwork. This was to ensure that the cells would have a flush contact with the soil at the backfill-pile cap interface. The VWs found in the transducer housing were then slightly bent away for the back wall of the pile cap.

Five Geokon 4000 strain gages were installed in the upper 1.5 m of the piles, since bending moments are critical near the base of the abutment. As seen in Figure (4.2), three strain gages equally space at 0.5 m were installed on the exterior pile. On the center interior pile, two strain gages were installed spaced at 1 m. The installation process first comprised of excavating the top 1.5 m of the in-situ soil following pile driving. This was then followed by the attachment of strain gage mounting blocks to

the pile flanges, with a parallel alignment to the roadway direction. The excavated soil was then backfilled and compacted.

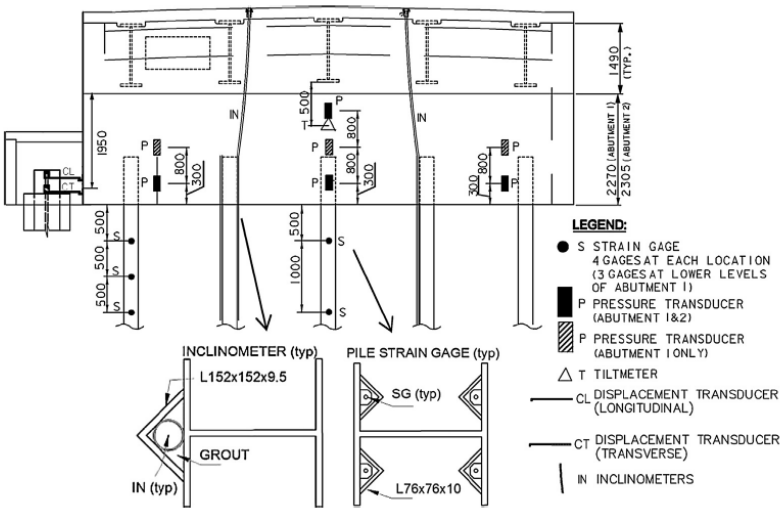

Figure 4.2 Middlesex bridge instrumentation plan (Civjan et al. 2013)

4.3 Finite Element Analysis

The full-scale interactions between the abutment-backfill and pile-soil under induced cyclic thermal loadings were numerically analyzed via the software package PLAXIS 3D 2021. As part of the analysis, the developed 3D model was first verified against full-scale data monitored in the field. Using the calibrated FE model, a series of parametric studies were then conducted to investigate changes in performance in response to the variation of key model parameters. The following section presents the details concerning the model development process, verification, and parametric studies.

4.3.1 Finite Element Mesh

Figure (4.3) shows the 3D FE model developed for verification. The soil layers and concrete clusters in the model were modelled using 10-noded tetrahedral volume elements, which were selected from the PLAXIS 3D element library. Girder and pile components were modelled via 3-noded beam and embedded beam elements, respectively, for optimized compatibility with the surrounding concrete and soil clusters. The bridge deck was modelled utilizing 6-noded triangular plate elements with six degrees of freedom at each node. The verified model contained approximately 220,000 elements. To maintain a reasonable computational time frame, elements within the abutment and pile deformation zones were refined locally and had an average size of approximately 96 mm. With respect to results obtained following a sensitivity analysis, the left boundary of model was extended -30 m from the center of the abutment. This was set since insignificant changes in backfill earth pressures and pile moments were observed when greater distances were utilized.

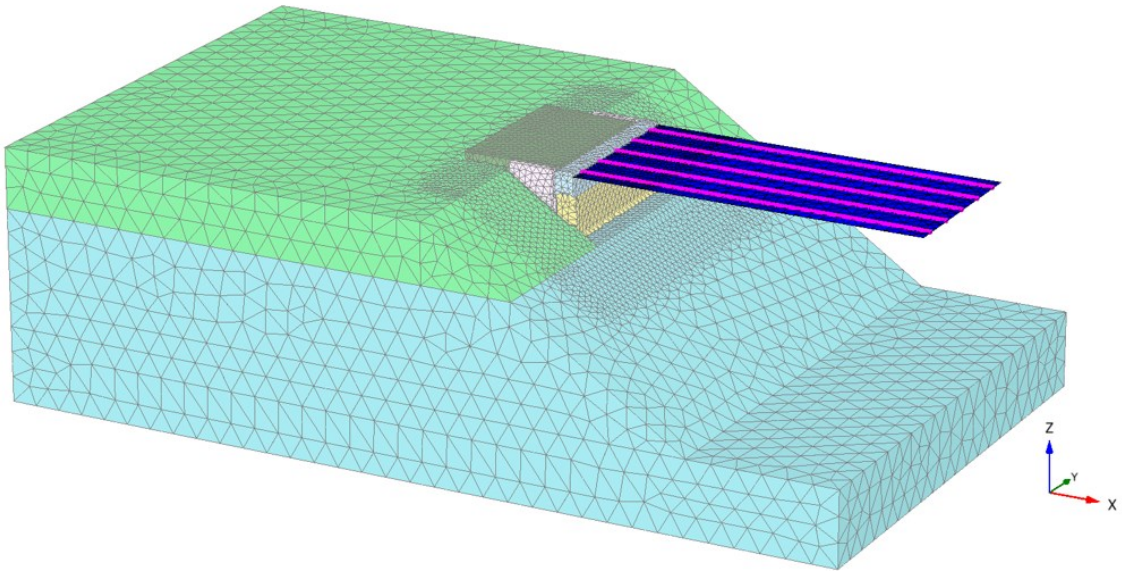

Figure 4.3 Three-dimensional FE model mesh

4.3.2 Boundary conditions

Due to the symmetrical nature of the Middlesex bridge about the two horizontal axes and the 0^o skew angle of the abutment, only half of the structure was considered during analysis as shown in Figure (4.3). The base of the model was assumed to be fully restrained against deformation in all directions. The top boundary of the model was permitted to deform about the *x*, *y*, and *z* axes. Finally, the lateral boundaries were only normally fixed against deformation.

4.3.3 Backfill and subgrade soil properties

The hyperbolic hardening soil model (HSM) extracted from the PLAXIS 3D constitutive model library was used to simulate the behavior of the backfill and pile soils, at a confining pressure (p_{ref}) of 100 kPa (PLAXIS 3D manuals 2018). As part of the HSM formulation,

this nonlinear constitutive soil model considers the combined double-stiffness model for elasticity and isotropic strain hardening. Originating from the hyperbolic model formulated by Duncan and Chang (Mahgoub and El Naggar 2020), the HSM is an elasto-plastic model which utilizes the theory of plasticity capable of representing soil densification, stiffness-stress dependency, plastic yielding, and dilatancy. Under induced thermal contractions and expansions, the HSM accurately simulates changes in soil stiffnesses at various stress levels, thus realistically capturing the stiffness-stress dependency of soils. Furthermore, it utilizes independent triaxial and oedometer stiffnesses, therefore yielding to accurate variations in soil behavior under deviatoric shear and compressive stresses. Furthermore, the utilization of the HSM captures the stress history of soils due to the variation in stiffness during unloading/reloading processes (Dhadse et al. 2021, Schanz et al. 1999). Finally, for small shear strains, the HSM utilizes hysteretic behaviors and shear dilatancy to accurately simulate variations in soil stiffness (El Naggar et al. 2016). Table (4.2) highlights the soil properties utilized in the verified system to represent the backfill and pile soil behaviors.

Table 6 FE model soil properties

Parameter	Backfill soil[1]	Subgrade soil[2]
Dry unit weight, γ_{dry} ($^{kN}/_{m^3}$)	17	19
Saturated unit weight, γ_{sat} ($^{kN}/_{m^3}$)	18.5	20
Secant stiffness in standard drained triaxial test, E_{50}^{ref} (kPa)	20	50
Tangent stiffness for primary oedometer loading, E_{oed}^{ref} (kPa)	16	40
Unloading/reloading stiffness, E_{ur}^{ref} (kPa)	60	150
Cohesion, c' (kPa)	1	2
Internal friction angle, φ' (^{o})	35	35
Dilatancy, ψ (^{o})	5	5
Power for stress-level dependency of stiffness, m	0.5	0.5

[1]For the backfill soil P_{ref} = 100 kPa and R_{int} = 0.3
[2]For the subgrade soil P_{ref} = 100 kPa and R_{int} = 0.6

4.3.4 RC abutment and approach slab properties

The concrete abutment and approach slab were simulated via linear elastic volume elements. PLAXIS formulates the linear elastic model through Hooke's law of linear elasticity. This constitutive model only incorporates the modulus of elasticity (E) and Poisson's ratio (v) of the concrete. In accordance with Kalayci (Kalayci 2012), the abutment pile cap incorporated an elastic modulus of 23 GPa, while the abutment diaphragm and approach slab had an elastic modulus of 25 GPa. The Poisson's ratio and unit weight for all concrete elements were set to 0.2 and 24 kN/m^3, respectively. To simulate soil-structure interactions such as stress transfers, slippage, and the relative movement between concrete elements and the surrounding soil during induced contractions and expansions (Dhadse et al. 2021), 12-node interface elements with zero thickness were

defined. A strength reduction factor (R_{int}) of 0.3 at the interfaces between the backfill and the abutment, approach slab, and wing-walls.

4.3.5 Pile, deck, and girder structural properties

The five steel plate girders supporting the deck were modelling using 3-noded elastic beam elements with six degrees of freedom at each node. In accordance with Mindlin's beam theory, these elements undergo shear, bending, and axial deformations (PLAXIS 3D manuals 2018). Each girder had a strong-axis and weak-axis moment of inertia of 0.0152 m^4 and 0.9 x 10^{-3} m^4, respectively. The cross-sectional area and elastic modulus were equal to 0.057 m^2 and 200 GPa, respectively.

The steel HP piles were modelled by 3-noded elastic embedded beam elements with six degrees of freedom at each node ending. These elements are formulated using beam elements to generate axial and flexural rigidities. The SSI of embedded beam elements is simulated via special interface elements with the surrounding soil, corresponding to skin and base resistances. As these elements embody a zero thickness, PLAXIS generates an elastic zone equal to the actual dimension of the pile where soil plasticity is neglected, thus corresponding to an equivalent volume pile behavior (PLAXIS 3D manuals 2018; Sluis et al. 2014). To simulate the relative motion between the HP piles and the surrounding soil under thermal contractions and expansions, a special interface with a strength reduction factor of 0.6 was utilized. The modulus of elasticity and unit weight of the steel piles were set equal to 200 GPa and 78.5 kN/m^3, respectively. The cross-sectional area of each pile was set to 0.0159 m^2, corresponding to a strong-axis and weak-axis moment of inertia of 0.27 x 10^{-3} m^4 and 0.089 x 10^{-3} m^4, respectively.

The RC deck was modelled via 6-noded triangular elastic plate/shell elements with six degrees of freedom per node. Similar to beam elements, plate elements are formulated in accordance with Mindlin's plate theory which permits deformations under shear, bending, and axial forces (PLAXIS 3D manuals 2018). The thickness (d) of the deck was equal to 0.22 m. To model the concrete nature of the deck, the modulus of elasticity and Poisson's ratio of the plate element were set to 25 GPa and 0.2, respectively.

4.3.6 FE construction sequence

The staged construction for the verified FE system was defined in accordance with actual records during the full-scale construction schedule of the Middlesex bridge. Based on the K_0 procedure, a linear variation for in-situ vertical stresses were generated for the existing soil, depending on the unit weight of each soil layer (Mahgoub and El Naggar 2020). This initial stress generation procedure takes the loading history of the soil into consideration. Then, an open excavation with a width of 17.2 m and a slope of 1V:1.5H was simulated for the top 1.5 m of the in-situ soil prior to pile driving. After excavation, the five HP embedded pile elements equally spaced at 2.05 m were activated. The excavated in-situ soil cluster was then reactivated and compacted to simulate the backfilling process. Next, the pile-cap and wing-wall concrete clusters were activated together with the corresponding base interface elements. The first stage of soil backfilling with a thickness of 2.531 m was activated and compacted along with the corresponding backfill-pile cap and backfill-wing wall interface elements. Then, the upper wing-wall and abutment diaphragm clusters, deck, girders, and vertical loads were activated. The final stage of soil backfilling with a thickness of 1.09 m was activated and compacted together with the corresponding backfill-diaphragm and backfill-wing wall interface elements. Finally, extracted from measured

full-scale inclinometer data, prescribed lateral displacements were applied cyclically at the top of the abutment diaphragm, to simulate the two-year thermal contractions and expansions of the Middlesex bridge.

4.3.7 Parametric studies

Following the verification of the proposed 3D FE system, a series of parametric studies were conducted to investigate the influence of varying the backfill stiffness, pile size and orientation, abutment stiffness, and constitutive soil model on the resultant backfill earth pressure distributions and pile bending moments.

The first parametric study investigated the impact of varying the backfill stiffness behind the abutment back wall at a confining pressure (P_{ref}) of 100 kPa. In this parametric study, the four backfill stiffness comprised of loose sand (E_{50}^{ref} = 7.5 MPa), medium sand (E_{50}^{ref} = 20 MPa), dense sand (E_{50}^{ref} = 60 MPa), and gravel (E_{50}^{ref} = 150 MPa).

The second parametric study investigated the effect of utilizing various pile sizes oriented for strong axis and weak axis bending. The four pile sections used in this parametric study were HP 200 x 53, HP 250 x 85, HP 310 x 125, and HP 360 x174. The geometric properties of the different HP piles including the cross-sectional area, strong axis moment of inertia, and weak axis moment of inertia are summarized in Table (4.3).

The third parametric study investigated the effect of varying the stiffness of the RC abutment diaphragm and pile cap. For this study, RC classes such as Class A (E = 23.2 GPa), Class B (E= 21.5 GPa), and Class C (E = 24.9 GPa) were utilized.

The fourth parametric study investigated the impact of utilizing the linearly-elastic-perfectly-plastic Mohr-Coulomb (MC) soil model found in the PLAXIS 3D material model

library. For this study, the HS model was substituted for the MC model utilized in the calibrated FE system to model the behavior of the backfill and pile soil under induced thermal contractions and expansions.

Table 7 Various HP pile sections utilized in the second parametric study

HP pile section	Section area, A (m^2)	Strong-axis moment of inertia, I_1 (m^4)	Weak-axis moment of inertia, I_2 (m^4)
HP 200 x 53	6.84×10^{-3}	49.4×10^{-6}	16.8×10^{-6}
HP 250 x 85	10.8×10^{-3}	123×10^{-6}	42×10^{-6}
HP 310 x 125	16×10^{-3}	270×10^{-6}	89×10^{-6}
HP 360 x174	22.2×10^{-3}	508×10^{-6}	184×10^{-6}

4.4 Results and Discussion

This section first the discusses the monitored data acquired during the full-scale monitoring of the Middlesex bride, coupled with the relevant findings related to the verification of the FE 3D model at the abutment-backfill and pile-soil interfaces during induced cyclic contractions and expansions. The second part of this section reports the results and discusses the changes in performance associated with the thermal response of the calibrated FE model when key model parameters were varied.

4.4.1 Results of full-scale monitoring

Findings reported in this present study primarily focus on the generated lateral earth pressure distributions and pile moments corresponding to induced cyclic thermal loadings. However, extensive data related to the full-scale monitored data are presented in Kalayci (Kalayci 2012). To verify the reliability of the proposed model, acquired lateral earth stress

variations and pile bending moments during the full-scale monitoring program were plotted against simulated findings using the calibrated FE model.

4.4.1.1 Lateral earth pressure distributions

The accumulated lateral earth stress distributions at the instrumented PC sensor locations at the end of construction are highlighted in Table (4.4).

Figure (4.4) contrasts the field monitored lateral earth stress variations during extreme minimum and maximum temperatures at each sensor location against findings generated by the proposed FE system using PLAXIS 3D. As shown in Figure (4.4), the lateral stresses at the abutment-backfill interface obtained via the developed PLAXIS FE system closely match to the field monitored earth pressure distributions. As indicated by the plotted figure, accumulated earth pressures at the end of construction incrementally increased and decreased with induced bridge expansions and contractions, respectively. Thus, during temperature rises, induced girder and deck expansions caused the backfill soil to occupy passive states. However, as ambient temperatures dropped, bridge contractions forced the backfill soil into active states. Furthermore, the magnitude of induced stresses strongly depended on the lateral extent of bridge contractions and expansions. This was observed as the resultant incremental passive stresses increased with larger bridge expansions into the backfill soil. As the abutment translated into the backfill during expansive cycles, the monitored lateral earth pressures were found to vary linearly with depth. This was not the case during the first and second active cycles however, as the instrumented PCs indicated unusual drops in lateral stresses at the middle sensor, giving rise to nonlinear distributions. This unforeseen behavior can be explained by investigating the construction history of the

backfill in relation to the middle sensor. By inspecting the measured pressure data at the end of construction, the cumulative value at the middle sensor was less than the top and bottom sensors. This may be associated with unforeseen soil interactions at middle sensor location during the backfilling and compaction process at the abutment-backfill interface, therefore resulting in lower values than anticipated. As a result, incremental decreases in earth pressures corresponding to induced abutment contractions would further reduce active stresses at the middle sensor.

Research conducted by Khodair (Khodair 2009) to investigate the cyclic thermal response of IABs indicated the occurrence of soil ratcheting at the backfill-abutment interface. However, this was not the case for the Middlesex bridge according to monitored earth pressure data. Lateral stress distributions plotted in Figure (4.4) do not provide evidence of soil ratcheting, since the average passive pressures at the bottom sensor during the first and second expansion cycles were 65 kPa and 68 kPa, respectively. Conversely, as observed by Kim and Laman (Kim and Laman 2010), soil softening was observed at the top sensor, since the passive stresses during the first and second year were 52 kPa and 42 kPa, respectively, irrespective of the net inward movement towards the backfill soil indicated by Kalayci (Kalayci 2012).

Table 8 Cumulative earth pressures at three sensor locations at the end of construction (Civjan et al. 2013)

Sensor location	**Earth pressure at the end of construction (kPa)**
Top	33.1
Middle	21.4
Bottom	42.1

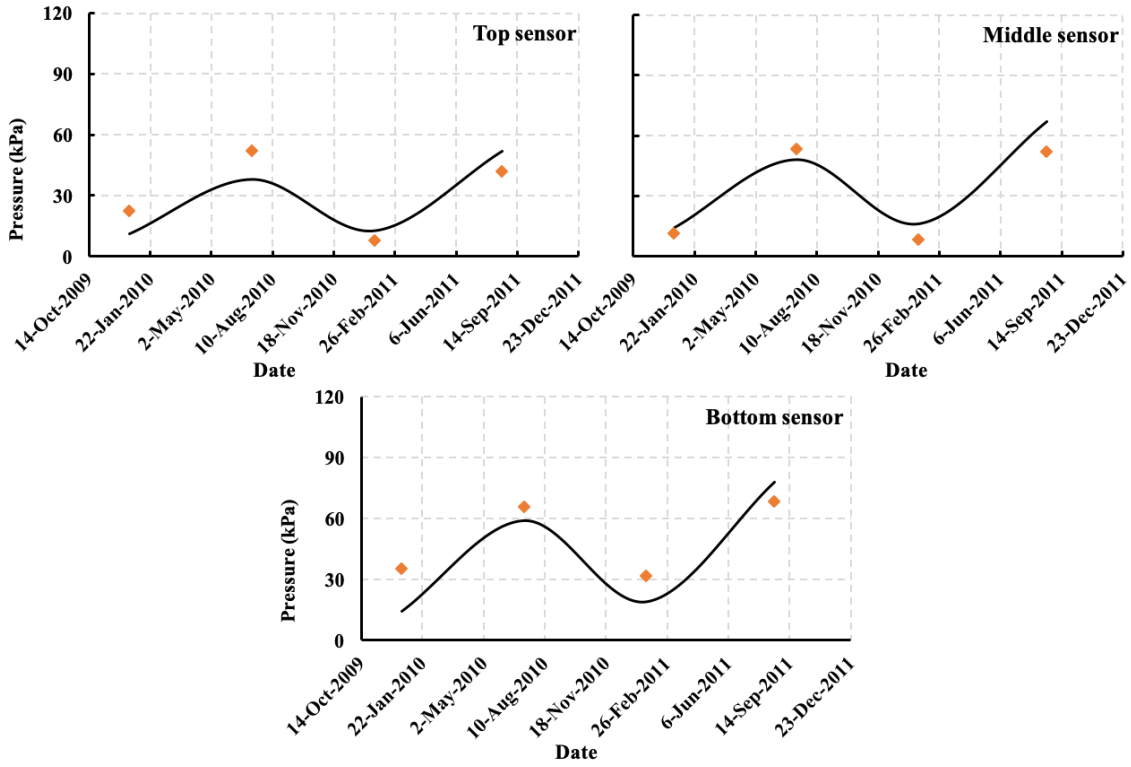

Figure 4.4 Verification lateral earth pressures at three PC sensor elevations

4.4.1.2 Pile moments

Table (4.5) summarizes the accumulative pile bending moments corresponding to the end of construction at the top, middle, and lower strain gages. Positive pile bending moments indicate that the pile side facing the embankment is tension, while the pile side facing the backfill is in compression. Negative pile bending moments indicate that the pile side facing the embankment is in compression, while the pile side facing the backfill is in tension. Figure (4.5) contrasts the field monitored pile bending moments during extreme minimum and maximum temperatures at each strain gage location against findings generated by the proposed FE system using PLAXIS 3D. As shown in Figure (4.5), the generated pile bending moment profiles via the calibrated PLAXIS FE system closely adhere to the full-

scale field monitored pile bending moments at the top, middle, and lower strain gage locations under induced abutment contractions and expansions. During seasonal changes, the thermal response of the substructure caused pile bending moments to alternate between positive and negative values with depth, hence bending in a double curvature. As indicated in Figures (4.5a) and (4.5c), maximum positive bending moments observed at the pile head during extreme bridge contractions decreased almost linearly with depth within the upper 2 m of the pile, prior to reaching inflection. However, as shown in Figures (4.5b) and (4.5d), the substructure response to induced expansions resulted in maximum negative moments which decreased nonlinearly with depth before reaching points of inflection and maximum positive moments at a depth below the base of the abutment.

As indicated in Figures (4.5a) and (4.5c), in periods of induced abutment contractions, the maximum positive pile bending moments at the pile head following the first and second year were equal to 90 kN.m and 86 kN.m, respectively. As shown in Figures (4.5b) and (4.5d), following the first and second expansive cycles, maximum negative bending moments at the pile head were equal to -35 kN.m and -77 kN.m, respectively. Furthermore, points of inflection occurred approximately 0.4 m and 3.85 m below the pile head during the first year of expansion, and approximately 0.3 m and 3.6 m below the pile head following second expansive cycle. Finally, with the maximum recorded moment over the two-year monitoring period equaling 90 kN.m, the substructure piles did not experience yielding since the 251 kN.m yielding moment of the steel HP piles was not exceeded.

Table 9 Cumulative pile bending moments at the end of construction (Civjan et al. 2013)

Strain gage location	Pile bending moment at the end of construction[1] (kN.m)
Top	38
Middle	36.6
Bottom	24.4

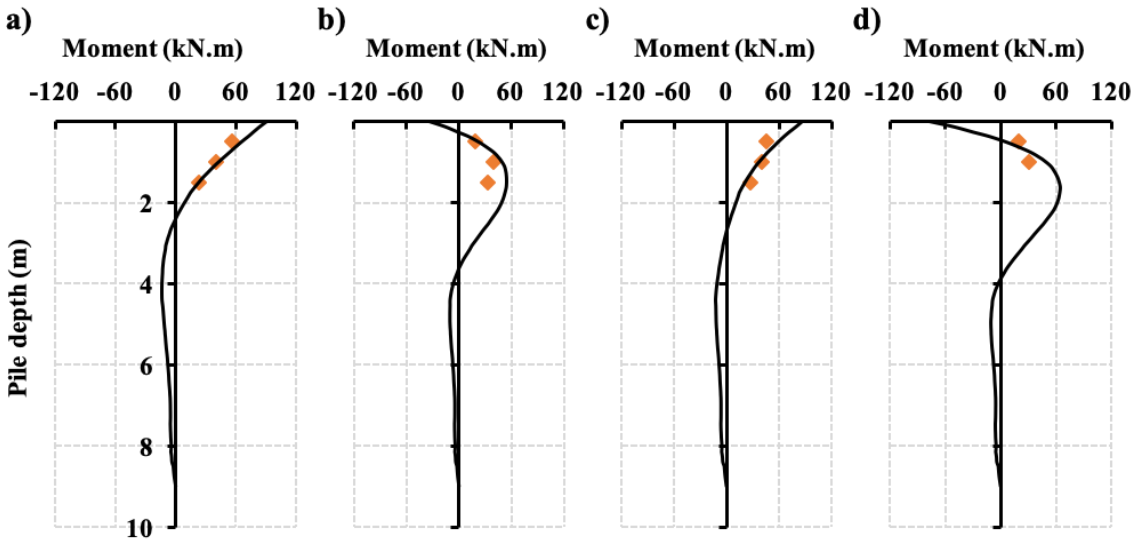

Figure 4.5 Verification of pile bending moments at maximum and minimum temperatures: **(a)** 12/19/2009 – 1st year (T_{Min} = -12.5°C), **(b)** 07/07/2010 – 1st year (T_{Max} = 38°C), **(c)** 01/23/2011 – 2nd year (T_{Min} = -13°C), and **(d)** 08/20/2011 (T_{Max} = 32.2°C) – 2nd year

4.4.2 Results of parametric studies

4.4.2.1 Effect of backfill stiffness

Figure (4.6) compares the changes in earth pressure distributions at the backfill-pile cap interface at three PC sensor elevations, for various backfill stiffnesses ranging from loose sand to gravel. Irrespective of the backfill stiffness, it can be seen from Figure (4.6) that as

the abutment contracts and expands into active and passive states, the corresponding lateral stresses decreased and increased, respectively, at the top, middle, and bottom PC sensors. During periods of contraction, changes in backfill stiffness had insignificant effects on active pressure magnitudes generated at the top, middle, and bottom sensors. Conversely, at all sensor locations, significant variations were found during periods of expansion, where increasing the stiffness of the soil from loose sand to gravel considerably increased the resultant passive pressure distributions. As shown in Figure (4.6) during the first and second expansive cycles, increasing the stiffness of the backfill from loose sand to gravel corresponded to an increase in passive pressures by 524% and 534%, respectively. This matches the conclusions drawn by Kong et al. (Kong et al. 2016) following a numerical study conducted on an IAB supported by pre-stressed precast concrete piles in Louisiana, USA.

Figure (4.7) compares pile bending moments corresponding to four different backfill stiffnesses. As shown in Figure (4.7), utilizing various backfill soil stiffnesses during induced thermal contractions and expansions had no effects on the general shape of the bending moment profiles. Though, unlike the trend exhibited by the earth pressure distributions in response to increases in backfill stiffness, Figure (4.7) showed that the maximum positive and negative bending moments decreased when stiffer backfill soils were utilized during contractive and expansive cycles. As indicated in Figure (4.7e), the maximum positive moment generated at the pile head was 97 kN.m for loose sand and 75 kN.m for gravel during the first cycle of contraction. Similarly, as shown in Figure (4.7e), the maximum negative moment generated at the pile head was -49 kN.m for loose sand

and -6 kN.m for gravel. This agrees with conclusions drawn by Civjan et al. (Civjan et al. 2007) following a parametric study on an IAB in Massachusetts, USA.

These changes in performance in response to different backfill stiffnesses may be related to the force equilibrium between the bridge abutment-backfill interface and the supporting piles. As ambient temperatures rise, the composite deck and girder material section undergo thermal expansions. This induces horizontal axial forces onto the abutment causing it to displace into the backfill soil. As a result, the backfill soil and piles generate passive stresses and shear forces in response to the axial forces transferred by the abutment. To maintain equilibrium, loads applied by the abutment are distributed between the backfill soil and piles according to their relative stiffness, where a greater ratio of the force is transmitted to the component with the highest stiffness. Hence, increasing the stiffness of the backfill during induced abutment expansions will relieve some of the stresses previously borne by the bridge piles. Consequently, this will correspond to increased passive stress distributions and bending moment reductions within the foundation piles.

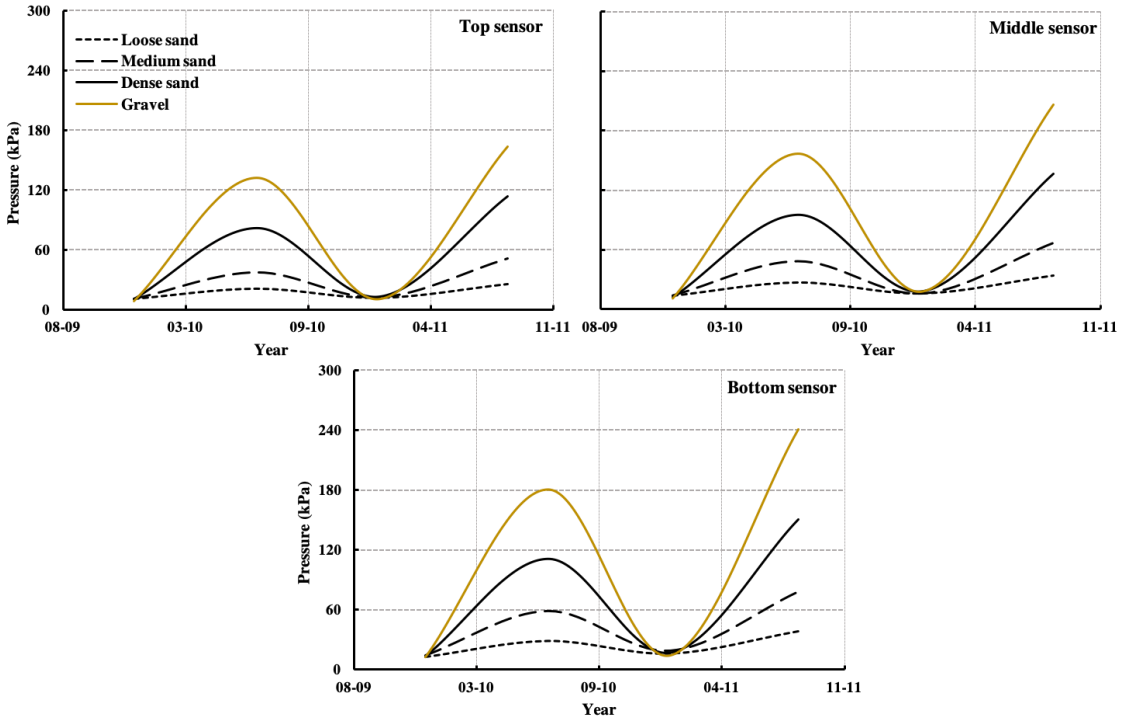

Figure 4.6 Comparison of lateral pressures calculated by using four various backfill stiffnesses, ranging from loose sand to gravel, for three sensor elevations

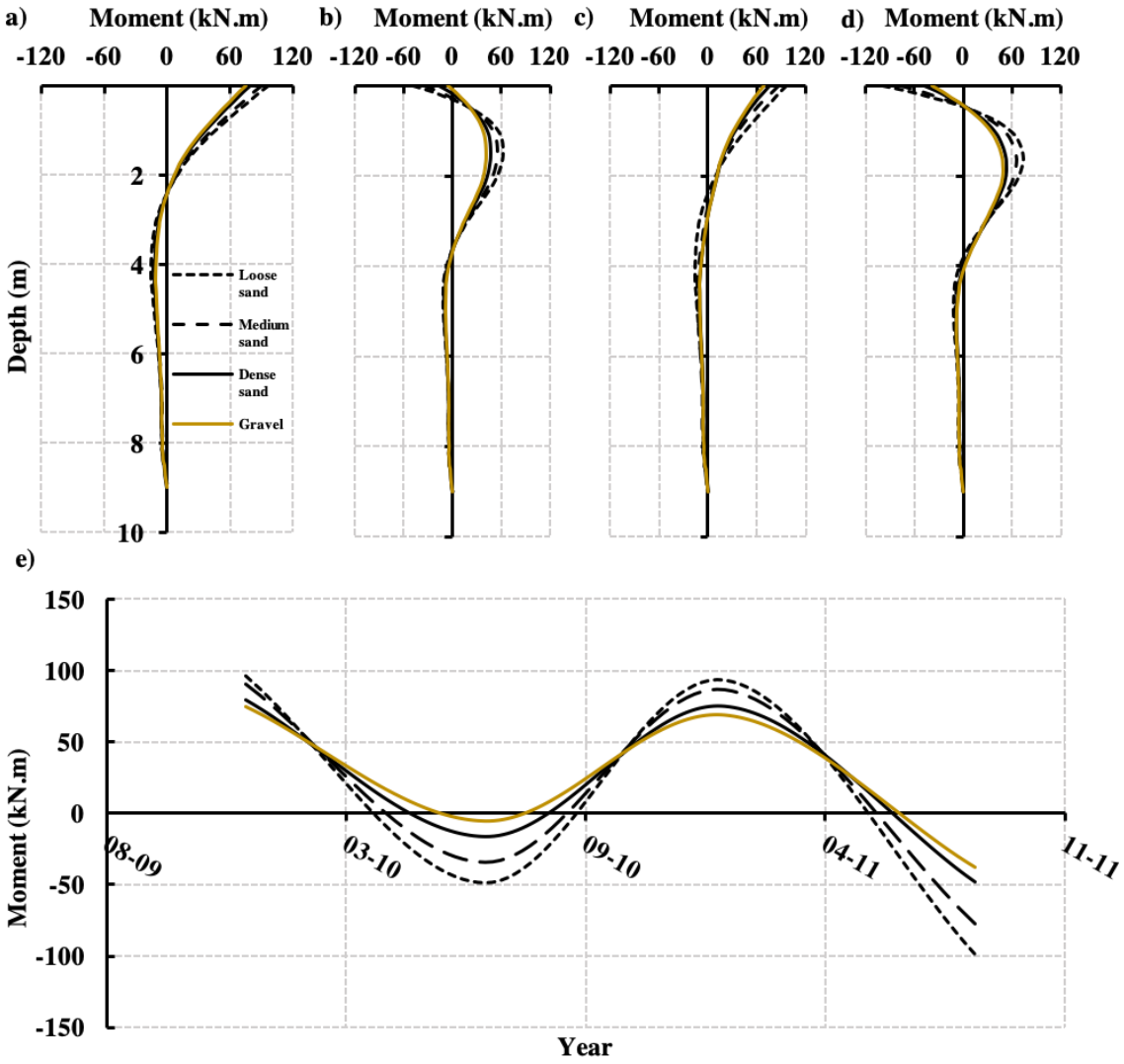

Figure 4.7 Comparison of pile bending moment profiles calculated for four different backfill stiffnesses, at maximum and minimum temperatures, for: **(a)** 12/19/09, **(b)** 07/07/10, **(c)** 01/23/11, **(d)** 08/20/11, and **(e)** variations in pile head moments with time

4.4.2.2 Effect of pile size and orientation

Figure (4.8) compares variations in lateral earth pressures for four different HP pile sections oriented for strong-axis bending at three PC sensor elevations. As shown in Figure (4.8), a similar pattern was followed at all three sensor locations, where the corresponding

passive earth pressures decreased as the pile size increased from HP 200 x 53 to HP 360 x 174. Furthermore, in response to utilizing different HP pile sections, the magnitude of the passive earth pressure variations increased with depth. However, varying the size of the HP section during periods of contraction had negligible effects on the corresponding active pressure distributions at all three sensor locations. For example, as indicated in Figure (4.8), the resultant passive stress variations corresponding to the first expansion cycle decreased by 8%, 9%, and 15% at the top, middle, and bottom sensor, respectively, as the pile section was increased from HP 200 x 53 to HP 360 x 174.

Figure (4.9) compares pile bending moment profiles obtained by utilizing four different HP pile sections oriented for strong-axis bending. As shown in Figure (4.9), maximum positive and negative pile bending moments increased when larger HP pile sections were utilized in periods of contraction and expansion. For instance, as shown in Figure (4.9a), as the pile section increased from HP 200 x 53 to HP 360 x 174, the corresponding maximum positive bending moment at the pile head increased by 238% in the first contraction cycle. Similarly, as shown in Figure (4.9d), the magnitude of the maximum negative and positive bending moments increased by 74% and 266%, respectively, when the pile section increased from HP 200 x 53 to HP 360 x 174 in the second expansion cycle. Moreover, it was observed that the depth at which inflection occurred was significantly influenced by the size of the utilized pile section in periods of contraction and expansion. Decreasing the pile section from HP 360 x 174 to HP 200 x 53 caused the inflection points to occur at shallower depths.

To investigate the influence of pile orientation, Figure (4.10) compares variations in lateral earth pressures for four different HP pile sections oriented for weak-axis bending at three

PC sensor elevations. In periods of abutment expansion, a general pattern was observed at all three sensors for piles oriented for weak-axis bending, where the corresponding passive earth stresses increased in contrast with strong-axis orientation for a given HP section. For instance, as shown in Figures (4.8) and (4.10), observed passive earth stresses during the first expansion cycle increased by 6%, 5%, and 11% at the top, middle, and bottom sensors, respectively, when utilizing an HP 360 x 174 section oriented for weak-axis bending in contrast to strong-axis bending. Alternating the orientation of the HP pile sections was found to have negligible impacts on the active pressure variations at all three sensor locations.

Figure (4.11) compares pile bending moment profiles obtained by utilizing four different HP pile sections oriented for weak-axis bending. For a given pile section, orientation for weak-axis bending corresponded to reduced maximum positive and negative moments during periods of contraction and expansion. For example, as shown in Figures (4.9a) and (4.11a), a comparison of the bending moments at the pile head when utilizing an HP 360 x 174 section during the first cycle of contraction indicates that alternating the orientation from strong-axis to weak-axis bending decreased the maximum positive moment by 33%. Similarly, as indicated in Figures (4.9d) and (4.11d), when an HP 360 x 174 section was utilized during the second cycle of expansion, changing the orientation from strong-axis to weak-axis bending reduced the maximum negative and positive bending moments by 20% and 40%, respectively.

This deformation pattern may be related to the force equilibrium between the abutment and the foundation piles when subjected to induced thermal contractions and expansions. In accordance with the load distribution method, the force equilibrium between the backfill

and the supporting piles is conserved by distributing the applied stress based on their relative stiffness. Hence, a larger portion of the applied stress is borne to the element with a higher stiffness (Hibbeler 2014). In addition, as the cross-sectional area of the HP pile increases, the moment of inertia about the strong- and weak-axes increase. However, in comparison, orientation for weak-axis bending yields to a smaller moment of inertia than strong-axis bending, thus increasing the flexibility of the supporting piles. Utilizing larger HP pile sections decreased the corresponding lateral passive stresses, since a greater ratio of the applied stress previously resisted by the backfill was transferred to supporting piles. Furthermore, by orienting the piles for weak-axis bending, the magnitude of the applied stress transferred to the pile decreased. This yielded to smaller pile bending moments during periods of contraction and expansion in contrast to piles oriented for strong-axis bending, agreeing with research conducted by Baptiste et al. (Baptiste et al. 2011) following a parametric study on prestressed concrete girder IABs.

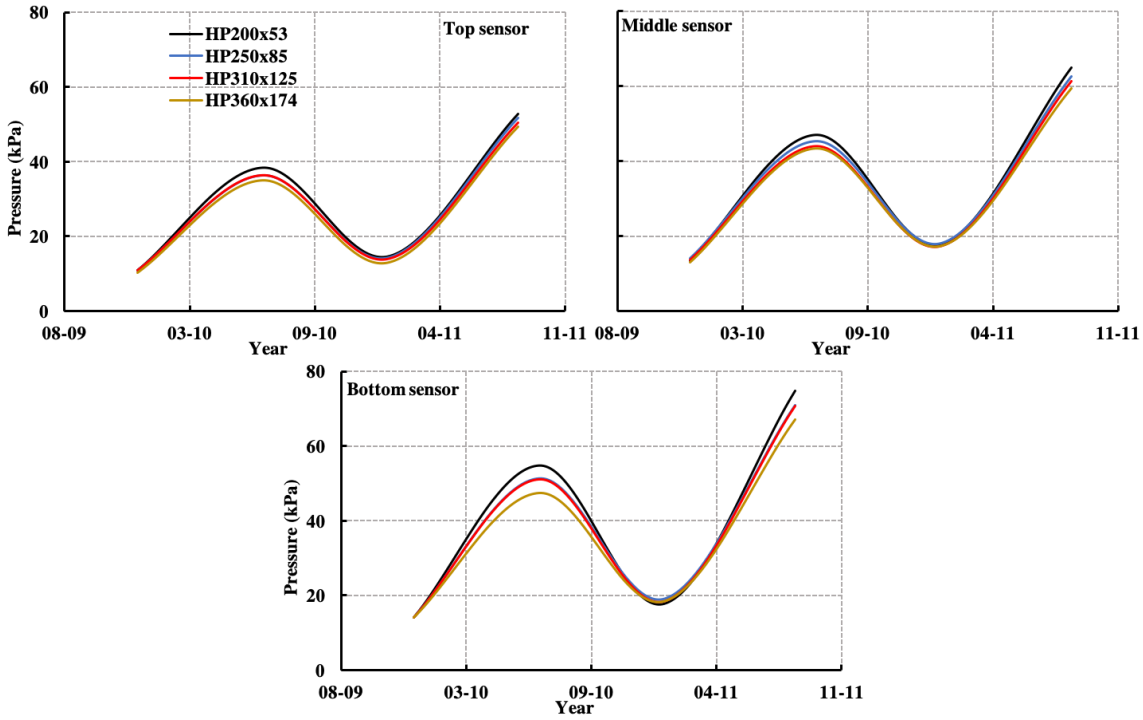

Figure 4.8 Comparison of lateral earth pressures at three PC sensor elevations obtained by using four different HP pile sections oriented for strong-axis bending

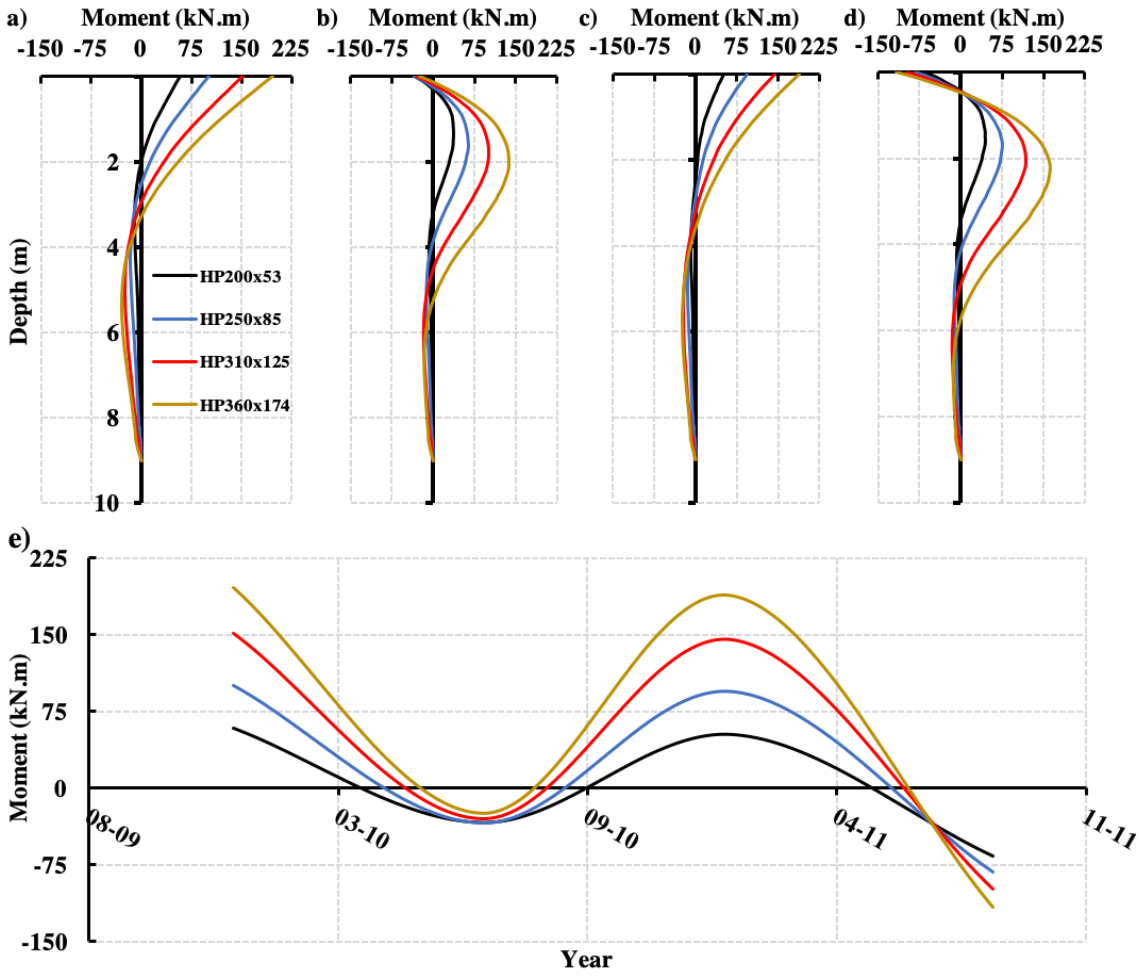

Figure 4.9 Comparison of pile bending moment profiles obtained by using four different HP pile sections oriented for strong-axis bending, at maximum and minimum temperatures, for: **(a)** 12/19/09, **(b)** 07/07/10, **(c)** 01/23/11, **(d)** 08/20/11, and **(e)** variations in pile head bending moments with time

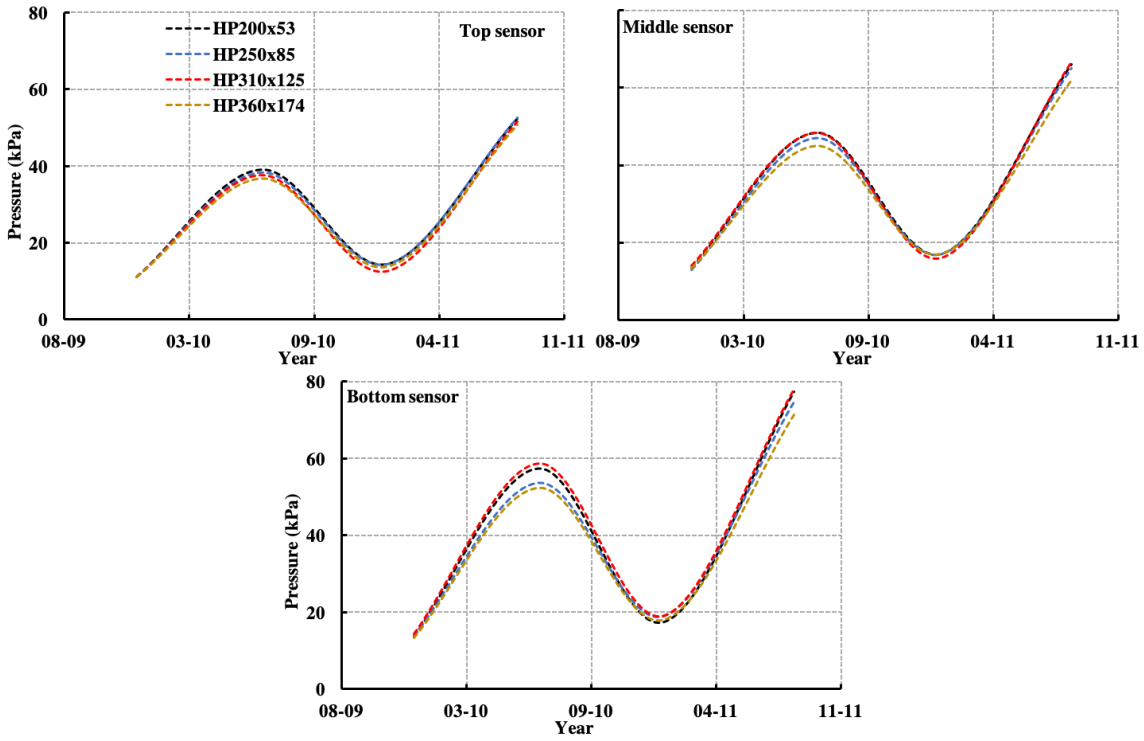

Figure 4.10 Comparison of lateral earth pressures at three PC sensor elevations obtained by using four different HP pile sections oriented for weak-axis bending

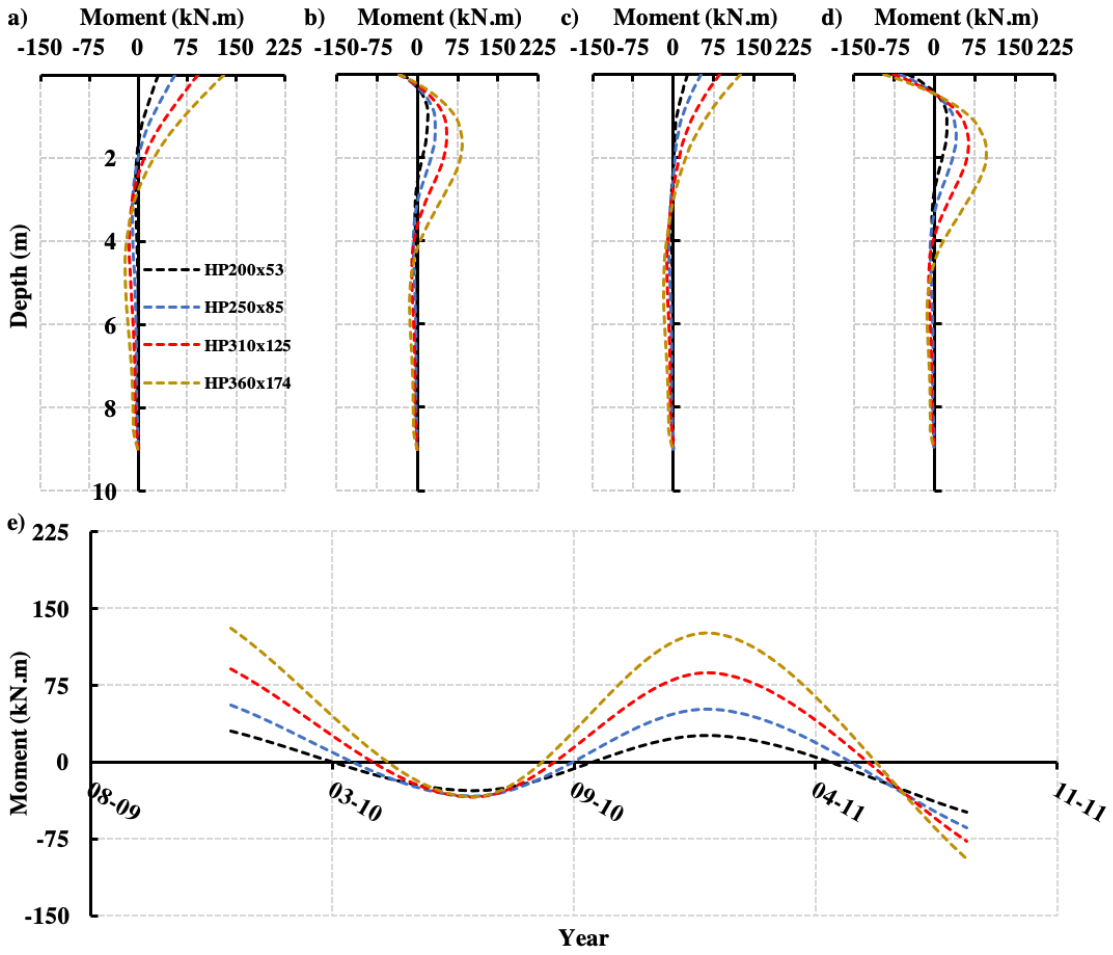

Figure 4.11 Comparison of pile bending moment profiles obtained by using four different HP pile sections oriented for weak-axis bending, at maximum and minimum temperatures, for: **(a)** 12/19/09, **(b)** 07/07/10, **(c)** 01/23/11, **(d)** 08/20/11, and **(e)** variations in pile head bending moments with time

4.4.2.3 Effect of abutment stiffness

Figure (4.12) compares variations in lateral earth pressures for three different RC classes at three PC sensor elevations. As indicated in Figure (4.12), varying the stiffness of the RC abutment from Class A to Class C had no influence on the corresponding active and passive pressures for all three sensor elevations.

Figure (4.13) compares pile bending moment profiles obtained by utilizing three different classes of RC. As shown in Figure (4.13), differences in abutment stiffness had no effect on the resultant pile bending moment profiles during periods of contractions and expansions.

The observed behavior maybe be related to the relative stiffness between the RC bridge abutment and the surrounding soil. The stiffenesses of the backfill and pile soils utilized in the 3D model were 0.02 GPa and 0.05 GPa, while the stiffnesses of the RC abutments used in this study varied between 22 GPa and 25 GPa. Thus, relative to the soil surrounding the abutment, a variation of approximately 3 GPa in concrete stiffness has minimal effects on the load transferring capabilities of the abutment. Hence, the magnitude of the applied loads borne on the backfill and piles is unaffected, thus yielding to identical results.

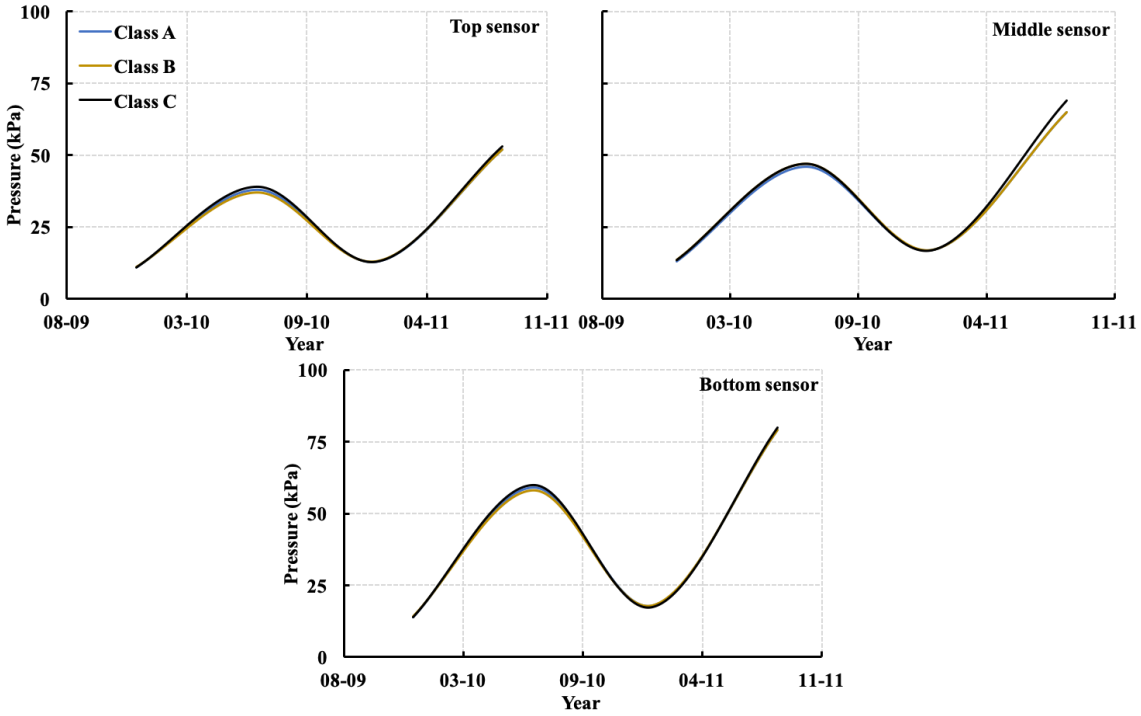

Figure 4.12 Comparison of lateral earth pressures at three PC sensor elevations obtained by using three different abutment stiffnesses

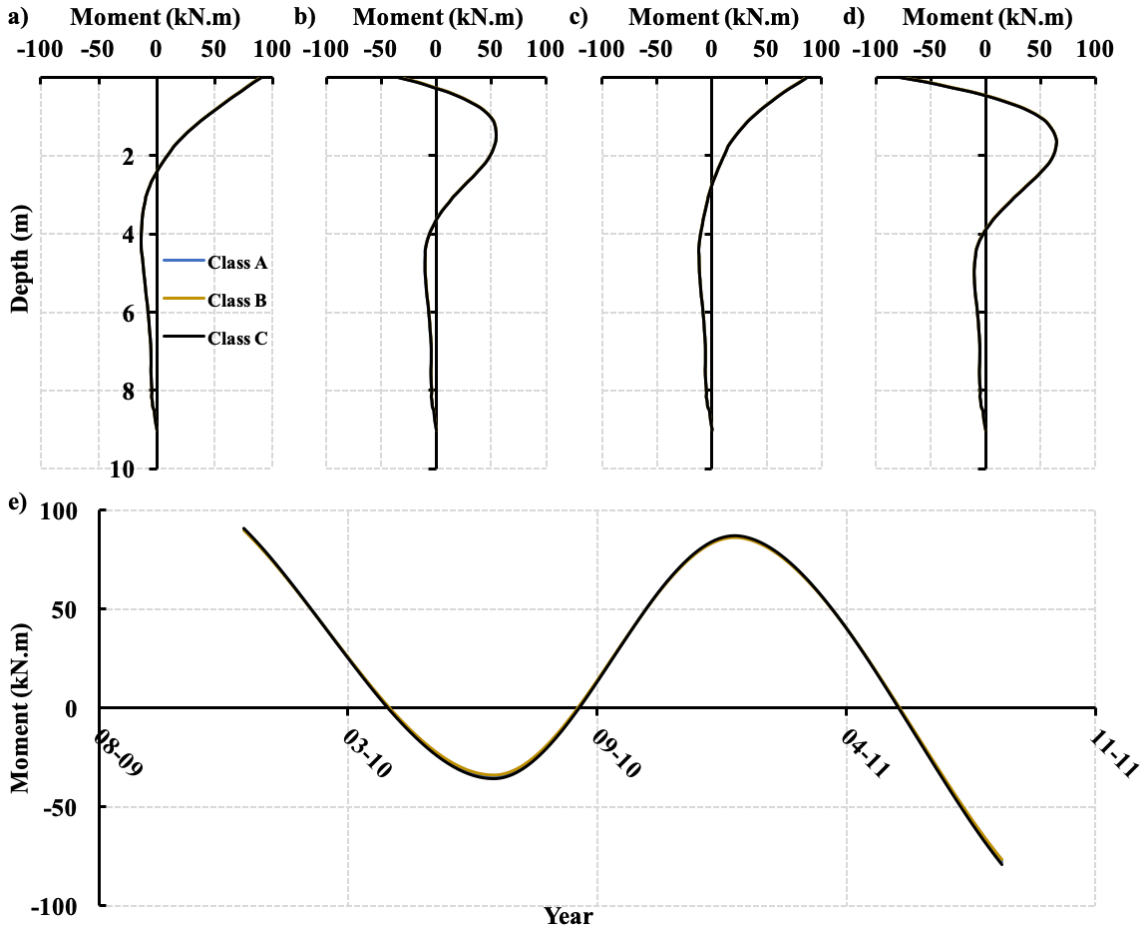

Figure 4.13 Comparison of pile bending moment profiles obtained for three abutment stiffnesses, at maximum and minimum temperatures, for: **(a)** 12/19/09, **(b)** 07/07/10, **(c)** 01/23/11, **(d)** 08/20/11, and **(e)** variations in pile head bending moments with time

4.4.2.4 Effect of constitutive soil model

Figure (4.14) compares variations in lateral earth pressures obtained by using the Mohr-Coulomb (MC) and Hardening Soil (HS) constitutive models at three PC sensor elevations. As shown in Figure (4.14), using the MC and HS models yielded to similar earth pressure distributions at the top sensor. At the middle sensor, while similar active stresses were obtained when utilizing the MS and HS models, using the MC model noticeably

underestimated passive pressures corresponding to the first and second expansion cycles. However, significant discrepancies were observed at the bottom sensor, where using the MC model yielded to smaller active and passive earth pressures in comparison with pressures obtained using the HS model. For instance, as shown in Figure (4.14), utilizing the MC model underestimated active and passive stresses by 42% and 24% in comparison with stresses obtained using the HS model during the second contraction and expansion cycles, respectively.

Figure (4.15) compares pile bending moment profiles obtained by utilizing the MC and HS constitutive soil models. As presented in Figure (4.15), changing the constitutive behavior of the soil had no effect on the general moment profile. However, utilizing the MC model underestimated maximum positive and negative moments during periods of contraction and expansion, respectively. Furthermore, changing the constitutive behavior of the soil from a HS model to a MC model caused positive moments to inflect at shallower depths during induced abutment contractions. For example, as shown in Figure (4.15e), maximum positive and negative bending moments at the pile head decreased by 31% and 62% as the constitutive behavior of the soil was changed from the HS to the MC model in the first cycle of contraction and expansion, respectively.

The variation in results between the MC and HS model maybe attributed to the elastic formulation and limitations associated with the MC model. Soil is a highly nonlinear and complex material which exhibits anisotropic and time-dependent behaviors under applied stresses. An important aspect associated with real soil behavior is the stiffness variation of soils based on the applied stress levels and paths. As stress levels increase, the stiffness of the soil increases accordingly. In addition, soils embody different stiffness levels to

accommodate various stress paths such as unloading/reloading, 1D compression, and deviatoric shear. Another important aspect of real soil behavior is related to irreversible plastic deformations prior to failure. Under applied stresses, soils undergo elastic and plastic deformations. As the applied load is removed, deformations within the elastic region of the soil are retained, given that failure has not occurred. However, in addition to elastic deformations, soils also undergo permanent plastic deformations prior to failure, which in turn impact the overall stiffness of the soil. Hence, opposite to the HS model, the MC model crudely simulates the complex stiffness response of soils prior to failure. Since the MC is formulated based on Hooke's law and mohr-coulomb's failure criterion, irreversible plastic deformations prior to the mobilization of shear strength are neglected. Thus, under applied stresses, soils are modelled to behave linearly elastic according to Hooke's law by a constant elastic modulus (E) and Poisson's ratio (v) prior to reaching the failure contour. This hinders the MC model's ability to capture the stiffness-stress dependency of soils under changing stress levels and paths, and therefore leading to severe result inaccuracies (Brinkgreve 2005).

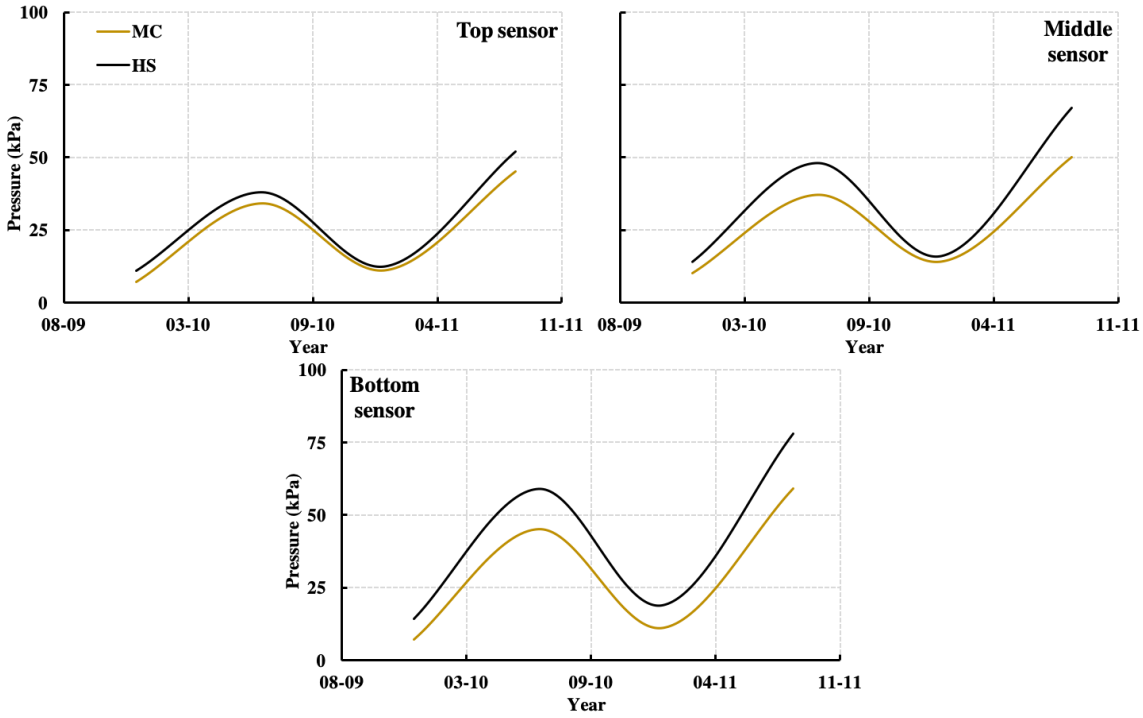

Figure 4.14 Comparison of lateral earth pressures at three PC sensor elevations obtained by using the MC and HS soil models

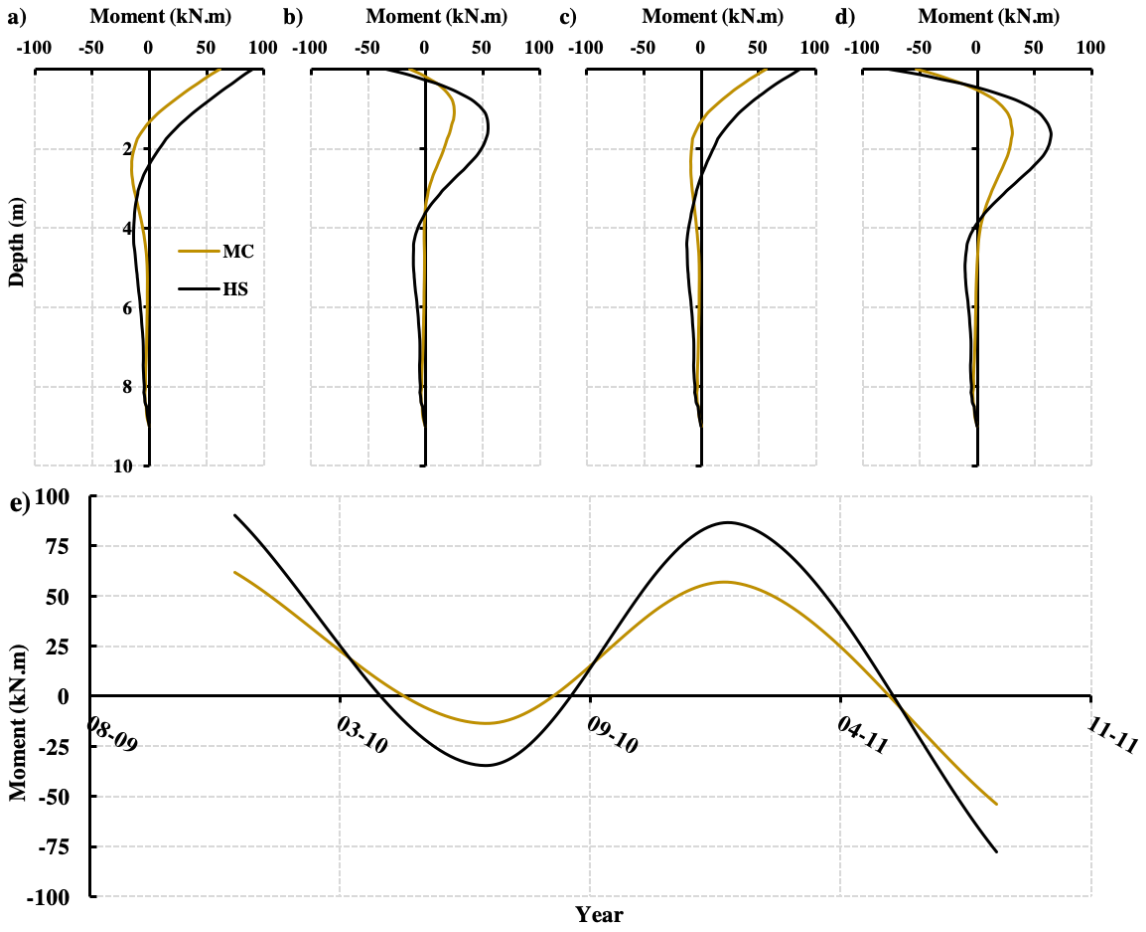

Figure 4.15 Comparison of pile bending moment profiles obtained by using the MC and HS soil models, at maximum and minimum temperatures, for: **(a)** 12/19/09, **(b)** 07/07/10, **(c)** 01/23/11, **(d)** 08/20/11, and **(e)** variations in pile head bending moments with time

4.5 Summary and Conclusions

This paper first reported the findings related to the thermal response of the Middlesex bridge in Vermont, USA, following a full-scale monitoring program over a two-year period. A detailed description concerning the development and calibration of a three-dimensional FE model was presented, where the corresponding model findings were verified against field measured lateral earth pressures and pile bending moments. This was

followed by conducting parametric studies to investigate the effect of varying the backfill stiffness, pile size and orientation, abutment stiffness, and constitutive soil model on the thermal response of IABs. Based on the findings of this paper and the corresponding parametric studies, the following conclusions can be drawn:

1. The developed 3D FE system accurately simulated the thermal response of the Middlesex bridge, since obtained FE lateral earth stresses and pile bending moments closely adhered to field measured results.
2. The stiffness of the backfill was found to significantly influence the corresponding earth pressure distributions and pile bending moments during expansion cycles. However, minor variations were also found during contraction cycles. As shown in Figure (4.6), utilizing a stiffer backfill caused extreme increases in passive pressures behind the pile-cap back wall. However, as indicated in Figure (4.7), pile bending moments were found to decrease as the stiffness of the backfill increased.
3. Varying the size and orientation of the pile significantly impacted the force equilibrium between the backfill and the supporting piles. Decreasing the section size and orienting for weak-axis bending increased the flexibility of the piles, therefore forcing a greater portion of the applied thermal load to be borne on the backfill soil. As shown in Figures (4.8) and (4.9), utilizing smaller HP sections yielded to greater earth pressures and lower pile bending moments, respectively. Similarly, as shown in Figures (4.8) and (4.10) and Figures (4.9) and (4.11), for a given HP section, orientation for weak-axis bending corresponded to larger earth pressures and lower pile bending moments, respectively, in contrast with strong-axis bending.

4. Variations in abutment stiffness had no influence on the resultant earth pressure distributions and pile bending moments. As shown in Figures (4.12) and (4.13), obtained earth pressures and pile bending moments for Class A, B, and C were identical, respectively.
5. The selection of a constitutive model to simulate soil behavior under induced thermal loadings significantly impacted the reliability and accuracy of the FE results. The HS model was shown to accurately mimic the nonlinear nature of soil during contraction and expansion cycles, in contrast to the MC model. As indicated in Figure (4.14), utilizing the MC model yielded to lower active and passive pressures, particularly at the bottom sensor location. As shown in Figure (4.15), varying the constitutive behavior of the soil had no influence on the moment pattern, however, using the MC model significantly underestimated the corresponding pile bending moments during periods of contraction and expansion.

References

Abdel-Fattah, M.T., Abdel-Fattah, T.T., Hemada, A.A., (2018). Nonlinear Finite-Element Analysis of Integral Abutment Bridges due to Cyclic Thermal Changes. *Journal of Bridge Engineering*, 23(2). https://doi.org/10.1061/(ASCE)BE.1943-5592.0001183

Arockiasamy, M., Butrieng, N., Sivakumar, M., (2004). State-of-the-Art of Integral Abutment Bridges: Design and Practice. *Journal of Bridge Engineering*, 9(5), 497-506. https://doi.org/10.1061/(ASCE)1084-0702(2004)9:5(497)

Arsoy, S., Barker, R. M., and Duncan, J. M., (1999). The behavior of integral abutment bridges. *Rep. No. FHWA/VTRC 00-CR3*, Virginia Transportation Research Council, Charlottesville, Va.

Baptiste, K.T., Kim, W.S., Laman, J.A., (2011). Parametric Study and Length Limitations for Prestressed Concrete Girder Integral Abutment Bridges. *Structural Engineering International*, 21(2), 151-156. https://doi.org/10.2749/101686611X12994961034219

Brinkgreve, R.B.J. (2005). Selection of soil models and parameters for geotechnical engineering application. In J. A. Yamamuro, & V. N. Kaliakin (Eds.), *Soil Constitutive Models* (pp. 69-98). American Society of Civil Engineers (ASCE).

Burke, M. P., Jr. (1993). Integral bridges: Attributes and limitations. *Transportation Research Record.1393*, National Research Council, Washington, D.C., 1–8.

Caristo, A., Barnes, J., Mitoulis, S.A., (2018). Numerical modelling of integral abutment bridges under seasonal thermal cycles. *Proceedings of the Institution of Civil Engineers – Bridge Engineering*, 171(3), 179-190. https://doi.org/10.1680/jbren.17.00025

Civjan, S.A., Bonczar, C., Breña, S.F., DeJong, J., Crovo, D., (2007). Integral Abutment Bridge Behavior: Parametric Analysis of a Massachusetts Bridge. *Journal of Bridge Engineering*, 12(1), 64-71. https://doi.org/10.1061/(ASCE)1084-0702(2007)12:1(64)

Civjan, S.A., Kalayci, E., Quinn, B.H., Breña, S.F., Allen, C.A., (2013). Observed integral abutment bridge substructure response. *Engineering Structures*, 56, 1177-1191. https://doi.org/10.1016/j.engstruct.2013.06.029

Coduto, D.P., (2001). Foundation Design: Principles and Practices. 2nd ed. Prentice Hall, Inc., Upper Saddle River, New Jersey.

Dhadse, G.D., Ramtekkar, G.D., Bhatt, G., (2021). Finite Element Modelling of Soil Strucutre Interaction System with Interface: A Review. *Archives of Computational Methods in Engineering*, 28, 3415-3432. https://doi.org/10.1007/s11831-020-09505-2

El Naggar, H., Mahgoub, A., Duguay, F., and Valsankgar, A. (2016). Impact of the Employed Soil Model on the Predicted Behaviour of Integral Abutment Bridges. *Proceedings of the 69th Canadian Geotechnical Conference*, Vancouver, Canada

Fennema, J.L., Laman, J.A., Linzell, D.G., (2005). Predicted and Measured Response of an Integral Abutment Bridge. *Journal of Bridge Engineering*, 10(6), 666-677. https://doi.org/10.1061/(ASCE)1084-0702(2005)10:6(666)

Greimann, L.F., Yang, P.S., Wolde-Tinsae, A.M., (1986). Nonlinear Analysis of Integral Abutment Bridges. *Journal of Structural Engineering*, 112(10), 2263-2280. https://doi.org/10.1061/(ASCE)0733-9445(1986)112:10(2263)

Hibbeler, R. C., (2014). Mechanics of Materials. 9th ed. Upper Saddle River: Pearson Prentice Hall.

Hoppe, E. J., and Gomez, J. P., (1997). Field study of an integral backwall bridge. *Research Rep. No. VTRC-R7*, Virginia Transportation Research Council, Charlottesville, Va.

Husain, I. and Bagnariol, D., (2000). Design and Performance of Jointless Bridges in Ontario: New Technical and Material Concepts. *Transportation Research Record*, 1696(1), 109-121. https://doi.org/10.3141%2F1696-14

Kalayci, E. (2012). *Performance monitoring and analysis of Integral Abutment Bridges* (Publication No. 3545945) [Doctoral dissertation, University of Massachusetts Amherst]. ProQuest Dissertations Publishing.

Khodair, Y.A., (2009). Lateral earth pressure behind an integral abutment. *Structure and Infrastructure Engineering*, 5(2), 123-136. https://doi.org/10.1080/15732470600924706

Kim, W.K. and Laman, J.A., (2010). Integral abutment bridge response under thermal loading. *Engineering Structures*, 32, 1495-1508. https://doi.org/10.1016/j.engstruct.2010.01.004

Kim, W.K. and Laman, J.A., (2012). Seven-Year Field Monitoring of Four Integral Abutment Bridges. *Journal of Performance of Constructed Facilities*, 26(1), 54-64. https://doi.org/10.1061/(ASCE)CF.1943-5509.0000250

Kong, B., Cai, C.S., Zhang, Y., (2016). Parametric study of an integral abutment bridge supported by prestressed precast concrete piles. *Engineering Structures*, 120, 37-48. https://doi.org/10.1016/j.engstruct.2016.04.034

Mahgoub, A. and El Naggar, H., (2020). Innovative Application of Tire-Derived Aggregate around Corrugated Steel Plate Culverts. *Journal of Pipeline Systems Engineering and Practice*, 11(3). https://doi.org/10.1061/(ASCE)PS.1949-1204.0000466

Ooi, P.S.K., Lin, X., Hamada, H.S., (2010). Field Behavior of an Integral Abutment Bridge Supported on Drilled Shafts. *Journal of Bridge Engineering*, 15(1), 4-18. https://doi.org/10.1061/(ASCE)BE.1943-5592.0000036

Ooi, P.S.K., Lin, X., Hamada, H.S., (2010). Numerical Study of an Integral Abutment Bridge Supported on Drilled Shafts. *Journal of Bridge Engineering*, 15(1), 19-31. https://doi.org/10.1061/(ASCE)BE.1943-5592.0000037

PLAXIS 3D manuals (2018).

Quinn, B.H. and Civjan, S.A., (2017). Parametric Study on Effects of Pile Orientation in Integral Abutment Bridges. *Journal of Bridge Engineering*, 22(4). https://doi.org/10.1061/(ASCE)BE.1943-5592.0000952

Schanz, T., P. A. Vermeer, and P. G. Bonnier. 1999. The hardening soil model: Formulation and verification. *In Beyond 2000 in computational geotechnics: 10 years of Plaxis*, 281–296. Rotterdam, Netherlands: A.A. Balkema.

Sluis, J., Besseling, F., Stuurwold, P., Lengkeek, A., (2014). *Validation and Application of the Embedded Pile Row Feature in PLAXIS 2D*. Witteveen+Bos, The Netherlands.

Yang, P.S., Wolde-Tinsae, A.M., Greimann, L.F., (1985). Effects of Predrilling and Layered Soils on Piles. *Journal of Geotechnical Engineering*, 111(1), 18-31. https://doi.org/10.1061/(ASCE)0733-9410(1985)111:1(18)

Zakhem, A.M. and El Naggar, H., (2019) Effect of the constitutive material model employed on predictions of the behaviour of earth balance (EFB) shield-driven tunnels. *Transportation Geotechnics*, 21. https://doi.org/10.1016/j.trgeo.2019.100264

CHAPTER 5 CONCLUSIONS AND RECOMMENDATIONS

5.1 Summary

Integral abutment bridges (IABs) are continuous single or multi-spanned structures, deprived from expansion and bearing joints. Hence, the deck and girder sections are monolithically connected to the abutment, forming a rigid body. This resulted in favorable attributes such as enhanced economical and structural performances. However, due to the elimination of expansion and bearing joints, IABs accommodate induced cyclic thermal movements through the global expansion and contraction of the superstructure. Superstructure expansions and contractions induce axial loads upon the abutment, causing them to translate and rotate towards and away from the backfill soil, respectively. This mode of deformation induces significant stresses within the superstructure, backfill soil, and supporting piles. However, due to the relatively recent introduction of IABs, their intricate soil-structure interactions (SSIs) under the influence of seasonal variations are not yet fully understood. In reaction to this challenge, several researchers conducted full-scale monitoring programs to evaluate the performances of IABs under cyclic thermal fluctuations. In addition, numerical parametric studies have been conducted to investigate the changes in the thermal performances of IABs in response to various conditions. However, most previous research modelled the SSIs of IABs via the *p-y* approach. Therefore, utilizing finite-element (FE) two- and three-dimensional models, this research aims to further contribute to the understanding of IABs by simulating the thermal performance of a case study IAB within a continuous soil medium characterized using advanced nonlinear constitutive soil models, with the corresponding interface elements.

Chapter 2 presented a comprehensive overview related to IABs and their corresponding attributes and limitations. Furthermore, details about the various primary and secondary loads acting on these structures were discussed, along with load determination methods extracted from the American Association of State Highway and Transportation Officials (AASHTO) bridge manual and various Transportation Research Records found in the literature. Moreover, current state of the art IAB design practices and guidelines utilized by departments of transportations (DOTs) found in North America, Europe, Asia, and Australia/New Zealand were also compared.

Chapter 3 presented a numerical investigation on the Middlesex bridge in Vermont, USA, to study the thermal performance of the structure under temperature induced movements. Following the full-scale monitoring of the structure, an FE model using the software PLAXIS 2D was developed and verified against field measured earth pressure distributions and pile bending moments. Following the verification of the proposed 2D FE system, parametric studies were conducted to investigate the effect of varying the constitutive soil model, backfill stiffness, abutment stiffness, pile size and orientation, and span length on the resultant earth pressure distributions at the abutment-backfill interface and pile bending moments. This chapter also provides details related to the utilization of theoretical techniques to approximate abutment expansions and contraction, where the corresponding findings were compared to deformations acquired in the field.

Chapter 4 presented the findings related to a numerical investigation on the Middlesex bridge using the software PLAXIS 3D. The purpose of this study was to develop an FE model using three-dimensional techniques to further explore the thermal performance of IABs. Prior to the numerical research, the proposed 3D FE system was verified against

available field measured deformations. Subsequently, as part of the numerical research, key parameters such as backfill stiffness, pile size and orientation, abutment stiffness, and constitutive soil model were varied to investigate their impact on the corresponding lateral earth pressure distributions at the backfill-abutment interface and pile bending moments.

5.2 Conclusions

Based on the conducted research presented in this thesis, the following conclusions can be drawn:

1. The calibrated two- and three-dimensional FE models were sufficiently able to simulate the thermal response of the Middlesex bridge over the two-year monitoring period. This was shown as the obtained lateral earth pressure distributions and pile bending moments closely adhered to those acquired during the monitoring period.
2. In the absence of field measured data, the lateral expansion and contraction of straight and symmetrical integral abutment bridges can be approximated as $\frac{1}{2}\alpha\Delta T\frac{L}{2}$, where α is the coefficient of thermal expansion, ΔT is the change in temperature, and L is the total length of the bridge. While this equation is formulated based on linear and isotropic assumptions, predicted abutment displacements closely adhered field deformations measured using inclinometers over the two-year monitoring period, except during the second expansion cycle. The variation in the predicted and field measured displacement during the second expansion cycle could be related to the equation's inability to capture the time-dependent effects experienced by the Middlesex bridge.

3. The employed constitutive soil model was found to significantly influence the simulated thermal performance of the Middlesex bridge. Based on the reported findings, the HS model was effectively able to capture and simulate the nonlinearity of soils under various stress levels and paths. However, due to the linear formulation of the MC model, severe result inaccuracies were found to arise. While utilizing the MC model to define the constitutive behavior of the backfill soil had minor impacts on the active pressures, significantly lower passive earth stresses, however, were seen in comparison to the HS model. Similarly, during expansion and contraction cycles, employing the MC model to define the constitutive behavior of the soil resulted in lower pile bending moments compared to results obtained when utilizing the HS model.
4. The thermal response of the Middlesex bridge was found to be strongly influenced by the stiffness of the backfill behind the abutment. Increasing the stiffness of the backfill from loose sand to gravel caused the resultant passive stresses to increase significantly during expansion cycles. However, employing stiffer backfill soils had negligible impacts on the active stresses during contraction cycles. Moreover, utilizing stiffer backfill soils were seen to reduce the resultant pile bending moments during expansion and contraction cycles.
5. Relative to the stiffness of the surrounding soil, the stiffness of the reinforced concrete abutment is approximately four hundred times larger. Hence, based on the findings of the parametric study, it was found that variations in abutment stiffness had no impact on the resultant earth pressure distributions and pile bending moments, since the load transferring mechanism of abutment was practically unaffected.

6. The flexibility of the supporting piles was found to be strongly dependent on the size and orientation of the steel HP sections. As the size of the steel HP pile decreased, coupled with orientation for weak-axis bending, the corresponding axial and bending rigidities decreased significantly. Based on the reported findings, it was seen that for a given orientation, increasing the size of the HP section caused the corresponding earth pressure distributions and pile bending moments to decrease and increase, respectively. Furthermore, for a given HP section, piles oriented for weak-axis bending yielded to larger earth pressure distributions and lower pile bending moments compared to those obtained when piles were oriented for strong-axis bending.
7. As part of the parametric study, the effect of varying span length on the resultant earth pressure distributions and pile bending moments were investigated. The number of spans directly impacts the magnitude of the transferred dead load from the superstructure to the abutments. Hence, employing fewer number of spans resulted in significantly larger dead loads acting on the abutment. Based on Rankine's theory, the magnitude of the passive and active earth pressures are given by $\sigma_h = \sigma_v K_{a/p}$, where σ_h is the horizontal stresses, σ_v is the vertical stress, and $K_{a/p}$ is the active or passive earth pressure coefficient. Furthermore, the supporting piles develop internal moments due to the lateral expansion/contraction of the abutment and applied vertical dead load. The expansion and contraction of the abutments under temperature fluctuations induces an eccentricity (Δ) from the at rest position. This deviation therefore introduces p-Δ effects on to the supporting piles. Thus, given that the induced abutment displacements are constant, increasing the vertical load on the abutment caused the corresponding earth pressure distributions and pile bending moments to increase accordingly.

5.2 Recommendations

1. Conducting further numerical research to investigate the impacts of abutment skew on the thermal performance of IABs.

2. By conducting dynamic analyses, the impacts of various truck loads and paths on the resultant earth pressure distributions and pile bending moments should be investigated.

3. In addition to varying the stiffness of the backfill, parametric studies should be conducted to investigate the variations in lateral earth stresses and pile bending moments in response to different pile soil restraints.

4. Using established climate prediction models, further research should be conducted to evaluate the thermal performance of IABs in response to increases in ambient temperatures due to global warming.

REFERENCES

AASHTO (2020). *LRFD Bridge Design Specifications*, 9th ed. American Association of State Highway and Transportation Officials, Washington, D.C.

Abdel-Fattah, M.T., Abdel-Fattah, T.T., Hemada, A.A., (2018). Nonlinear Finite-Element Analysis of Integral Abutment Bridges due to Cyclic Thermal Changes. *Journal of Bridge Engineering*, 23(2). https://doi.org/10.1061/(ASCE)BE.1943-5592.0001183

Abdel-Fattah, M.T. and Abdel-Fattah, T.T., (2019). Behavior of Integral Frame Abutment Bridges Due to Cyclic Thermal Loading: Nonlinear Finite-Element Analysis. *Journal of Bridge Engineering*, 24(5). https://doi.org/10.1061/(ASCE)BE.1943-5592.0001394

Abendroth, R.E., Greimann, L.F., Ebner, P.B., (1989). Abutment Pile Design for Jointless Bridges. *Journal of Structural Engineering*, 115(11), 2914-2929. https://doi.org/10.1061/(ASCE)0733-9445(1989)115:11(2914)

Abendroth, R.E. and Greimann, L.F., (1989). Rational Design Approach for Integral Abutment Bridge Piles. *Transportation Record 1223*.

Alaska Department of Transportation (2017). *Alaska Bridges and Structures Manual*, Highway Division, Alaska Department of Transportation: Juneau, AK, USA.

Arockiasamy, M., Butrieng, N., Sivakumar, M., (2004). State-of-the-Art of Integral Abutment Bridges Design and Practice. *Journal of Bridge Engineering*, 9(5), 497-506. https://doi.org/10.1061/(ASCE)1084-0702(2004)9:5(497)

Arsoy, S., Barker, R. M., and Duncan, J. M., (1999). The behavior of integral abutment bridges. *Rep. No. FHWA/VTRC 00-CR3*, Virginia Transportation Research Council, Charlottesville, Va.

Baptiste, K.T., Kim, W.S., Laman, J.A., (2011). Parametric Study and Length Limitations for Prestressed Concrete Girder Integral Abutment Bridges. *Structural Engineering International*, 21(2), 151-156. https://doi.org/10.2749/101686611X12994961034219

Barker, R.M., Duncan, J.M., Rojiani, K.B., Ooi, P.S.K., Tan, C.K., Kim, S.G., (1991). Manuals for the design of bridge foundations, National Cooperative Highway Research Program (NCHRP) Report 343, TRB, National Research Council, Washington, D.C.

Bonczar, C., Civjan, S., Breña, S., DeJong, J., (2005). Behavior of Integral Abutment Bridges: Field Data and Computer Modeling, Amherst: Federal Highway Administration.

Bozozuk, M. (1978). Bridge foundation move. *Transportation Research Record 678*, Transportation Research Board, Washington, D.C.

Breña, S.F., Bonczar, C.H., Civjan, S.A., DeJong, J.T., Crovo, D.S., (2007). Evaluation of Seasonal and Yearly Behavior of an Integral Abutment Bridge. *Journal of Bridge Engineering*, 12(3), 296-305. https://doi.org/10.1061/(ASCE)1084-0702(2007)12:3(296)

Brinkgreve, R.B.J. (2005). Selection of soil models and parameters for geotechnical engineering application. In J. A. Yamamuro, & V. N. Kaliakin (Eds.), *Soil Constitutive Models* (pp. 69-98). American Society of Civil Engineers (ASCE).

Burke, M. P., Jr. (1993). Integral bridges: Attributes and limitations. *Transportation Research Record.1393*, National Research Council, Washington, D.C., 1–8.

Burke, M.P. Jr. (2009). *Integral and semi-integral bridges*, Wiley-Blackell, Hoboken, NJ.

Caristo, A., Barnes, J., Mitoulis, S.A., (2018). Numerical modelling of integral abutment bridges under seasonal thermal cycles. *Proceedings of the Institution of Civil Engineers – Bridge Engineering*, 171(3), 179-190. https://doi.org/10.1680/jbren.17.00025

Chang L.M. and Lee, Y.J., (2002). Evaluation of Performance of Bridge Deck Expansion Joints. *Journal of Performance of Constructed Facilities*, 16(1), 3-9. https://doi.org/10.1061/(ASCE)0887-3828(2002)16:1(3)

Chovichien, V. (2004). *The Behavior and Design of Piles for Integral Abutment Bridges* (Publication No. 3154604) [Doctoral dissertation, Purdue University]. ProQuest Dissertations Publishing.

Civjan, S.A., Bonczar, C., Breña, S.F., DeJong, J., Crovo, D., (2007). Integral Abutment Bridge Behavior: Parametric Analysis of a Massachusetts Bridge. *Journal of Bridge Engineering*, 12(1), 64-71. https://doi.org/10.1061/(ASCE)1084-0702(2007)12:1(64)

Civjan, S. A., Kalayci, E., Quinn, B. H., Breña, S. F., & Allen, C. A. (2013). Observed integral abutment bridge substructure response. *Engineering Structures,* 56, 1177-1191. ISSN 0141-0296, https://doi.org/10.1016/j.engstruct.2013.06.029.

Coduto, D.P., (2001). Foundation Design: Principles and Practices. 2nd ed. Prentice Hall, Inc., Upper Saddle River, New Jersey.

Colorado Department of Transportation (2021). *Bridge Design Manual*, Highway Division, Colorado Department of Transportation: Denver, CO, USA.

CSA. (2014). Canadian Highway Bridge Design Code. CSA standard CAN/CSA-S6-14. Canadian Standards Association, Rexdale, Ontario, Canada.

Delaware Department of Transportation (2021). *Bridge Design Manual*, Highway Division, Delaware Department of Transportation: Harrington, DE, USA.

Dhadse, G.D., Ramtekkar, G.D., Bhatt, G., (2021). Finite Element Modeling of Soil Structure Interaction System with Interface: A Review. *Archives of Computational Methods in Engineering*, 28, 3415-3432. https://doi.org/10.1007/s11831-020-09505-2

District of Columbia Department of Transportation (2019). *Design and Engineering Manual*, Highway Division, District of Columbia Department of Transportation: Washington, D.C, USA.

Duncan, J.M., Chang, C.Y., (1970). Nonlinear Analysis of Stress and Strain in Soils. *Journal of the Soil Mechanics and Foundations Division*, 96(5), https://doi.org/10.1061/JSFEAQ.0001458

Dutta, S.C. and Roy, R., (2002). A critical review on idealization and modeling for interaction among soil-foundation-structure system. *Computers and Structures*, 80(20-21), 1579-1594. https://doi.org/10.1016/S0045-7949(02)00115-3

El Naggar, H., Mahgoub, A., Duguay, F., and Valsankgar, A. (2016). Impact of the Employed Soil Model on the Predicted Behaviour of Integral Abutment Bridges. *Proceedings of the 69th Canadian Geotechnical Conference*, Vancouver, Canada

England, G.L., David, B.I., Tsang, N.C.M., (2000). Integral Bridges: A Fundamental Approach to the Time-Temperature Loading Problem. Thomas Telford: London.

Faraji, S., Ting, J.M., Crovo, D.S., Ernst, H., (2001). Nonlinear Analysis of Integral Bridges: Finite-Element Model. *Journal of Geotechnical and Geoenvironmental Engineering*, 127(5), 454-461. https://doi.org/10.1061/(ASCE)1090-0241(2001)127:5(454)

Fennema, J.L., Laman, J.A., Linzell, D.G., (2005). Predicted and Measured Response of an Integral Abutment Bridge. *Journal of Bridge Engineering*, 10(6), 666-677. https://doi.org/10.1061/(ASCE)1084-0702(2005)10:6(666)

Florida Department of Transportation (2022). *Structures Design Guidelines*, Highway Division, Florida Department of Transportation: Tallahassee, FL, USA.

Freyermuth, C.L. (1969). Design of continuous highway bridges with precast, prestressed concrete girders. *Precast/Prestressed Concrete Institute Journal*, 14(2), 14-39. https://doi.org/10.15554/pcij.04011969.14.39

Frosch, R. J. & Lovell, D. M., (2011). *Long-Term Behaviour of Integral Abutment Bridges*, West Lafayette: Federal Highway Administration.

Frosch, R.J., Kreger, M.E., Talbott, A.M., (2009*). Earthquake Resistance of Integral Abutment Bridges*, West Lafayette: Purdue University.

Greimann, L.F., Yang, P.S., Wolde-Tinsae, A.M., (1986). Nonlinear analysis of Integral Abutment Bridges. *Journal of Structural Engineering*, 112(10), 2263-2280. https://doi.org/10.1061/(ASCE)0733-9445(1986)112:10(2263)

Grover, R.A. (1978). Movements of Bridge Abutments and Settlements of Approach Pavements in Ohio. *Transportation Research Record 679*.

Hannigan, P.J., Rausche, F., Likins, G.E., Robinson, B.R., Becker, M.L., (2016). *Design and Construction of Driven Pile Foundations – Volume I* (No. FHWA-NHI-16-009). United States. Federal Highway Administration. Office of Technology Applications.

Hassiotis, S., Khodair, Y., Roman, E., Dehne, Y., (2006). Evaluation of Integral Abutments (No. FHWA-NJ-2005-025).

Hibbeler, R. C., (2014). Mechanics of Materials. 9th ed. Upper Saddle River: Pearson Prentice Hall.

Hoppe, E.J. and Gomez, J.P. (1996). *Field study of an integral backwall bridge*, Virginia Transportation Research Council, VTRC 97-R7, October 1996, 47 p.

Hovarth, J.S. (2005). Integral-Abutment Bridges: Geotechnical Problems and Solutions Using Geosynthetics and Ground Improvement. *Proceedings of the 2005 FWHA Conference on Integral Abutment and Jointless Bridges*, Maryland, USA.

Huang, J., Shield, C.K., French, C.E.W., (2008). Parametric Study of Concrete Integral Abutment Bridges. *Journal of Bridge Engineering*, 13(5), 511-526. https://doi.org/10.1061/(ASCE)1084-0702(2008)13:5(511)

Huang, J., Shield, C., French, C., (2011). Behavior of an Integral Abutment Bridge in Minnesota, US. *Structural Engineering International*, 21(3), 320-331, https://doi.org/10.2749/101686611X12994961034336

Huntley, S.A. and Valsangkar, A.J., (2013). Field monitoring of earth pressures on integral bridge abutments. *Canadian Geotechnical Journal*, 50(8), 841-857. https://doi.org/10.1139/cgj-2012-0440

Huntley, S.A. and Valsangkar, A.J., (2014). Behavior of H-piles supporting an integral abutment bridge. *Canadian Geotechnical Journal*, 51(7), 713-734. https://doi.org/10.1139/cgj-2013-0254

Husain, I. and Bagnariol, D., (2000). Design and Performance of Jointless Bridges in Ontario: New Technical and Material Concepts. *Transportation Research Record*, 1696(1), 109-121. https://doi.org/10.3141%2F1696-14

Illinois Department of Transportation (2012). *Bridge Manual*, Highway Division, Illinois Department of Transportation: Springfield, IL, USA.

Kalayci, E. (2012). *Performance monitoring and analysis of Integral Abutment Bridges* (Publication No. 3545945) [Doctoral dissertation, University of Massachusetts Amherst]. ProQuest Dissertations Publishing.

Kalayci, E., Civjan, S.A., Breña, S.F., (2012). Parametric study on the thermal response of curved integral abutment bridges. *Engineering Structures*, 43, 129-138. https://doi.org/10.1016/j.engstruct.2012.05.007

Kansas Department of Transportation (2007). *Design Manual Volume III-Bridge Section*, Highway Division, Kansas Department of Transportation: Topeka, KS, USA.

Kaufmann, W. and Alvarez, M. (2011). Swiss Federal Roads Office Guidelines for Integral Bridges. *Structural Engineering International*, 21(2), 189-194. https://doi.org/10.2749/101686611X12994961034057

Khodair, Y.A. (2009). Lateral earth pressure behind an integral abutment. *Structure and Infrastructure Engineering*, 5(2), 123-136. https://doi.org/10.1080/15732470600924706

Kim, W., & Laman, J.A., (2010). Integral abutment bridge response under thermal loading. *Engineering Structures*, 32(6), 1495-1508. https://doi.org/10.1016/j.engstruct.2010.01.004.

Kim, W.S., Laman, J.A., (2012). Seven-Year Field Monitoring of Four Integral Abutment Bridges. *Journal of Performance of Constructed Facilities*, 26(1), 54-64. https://doi.org/10.1061/(ASCE)CF.1943-5509.0000250

Kong, B., Cai, C.S., Kong, X., (2015). Field monitoring study of an integral abutment bridge supported by precast concrete piles on soft soils. *Engineering Structures*, 104, 18-31. https://doi.org/10.1016/j.engstruct.2015.09.004

Kong, B., Cai, C.S., Zhang, Y., (2016). Parametric study of an integral abutment bridge supported by prestressed precast concrete piles. *Engineering Structures*, 120, 37-48. https://doi.org/10.1016/j.engstruct.2016.04.034

Kunin, J. and Alampalli, S. (2000). Integral Abutment Bridges: Current Practice in United States and Canada. *Journal of Performance of Constructed Facilities*, 14(3), 104-111. https://doi.org/10.1061/(ASCE)0887-3828(2000)14:3(104)

LaFave, J.M., Riddle, J.K., Jarrett, M.W., Wright, B.A., Svatora, J.S., An, H., Fahnestock, L.A., (2016). Numerical Simulations of Steel Integral Abutment Bridges under Thermal Loading. *Journal of Bridge Engineering*, 21(10). https://doi.org/10.1061/(ASCE)BE.1943-5592.0000919

LaFave, J.M., Brambila, G., Kode, U., Liu, G., Fahnestock, L.A., (2021). Field Behavior of Integral Abutment Bridges under Thermal Loading. *Journal of Bridge Engineering*, 26(4). https://doi.org/10.1061/(ASCE)BE.1943-5592.0001677

Lawver, A., French, C., Shield, C.K., (2000). Field Performance of Integral Abutment Bridge. *Transportation Research Record*, 1740(1), 108-117. https://doi.org/10.3141%2F1740-14

Lee, D. J. (1994). *Bridge bearing and expansion joints*. 2nd Ed., E & FN Spon, London.

Li, B. (2020). *Geo-structural Analysis of Integral Abutment Bridges*. Electronic Thesis and Dissertation Repository. 7540. https://ir.lib.uwo.ca/etd/7540/

Mahgoub, A. and El Naggar, H., (2020). Innovative Application of Tire-Derived Aggregate around Corrugated Steel Plate Culverts. *Journal of Pipeline Systems Engineering and Practic*, 11(3). https://doi.org/10.1061/(ASCE)PS.1949-1204.0000466

Massachusetts Department of Transportation (2020). *LRFD Bridge Manual – Part I*, Highway Division, Massachusetts Department of Transportation: Boston, MA, USA.

Minnesota Department of Transportation (2016). *Design Manual*, Highway Division, Minnesota Department of Transportation: St. Paul, MN, USA.

Mourad, S. and Tabsh, S.W., (1999). Deck slab stresses in Integral Abutment Bridges. *Journal of Bridge Engineering*, 4(2), 125-130. https://doi.org/10.1061/(ASCE)1084-0702(1999)4:2(125)

Munuswamy, S. (2004). Creep and Shrinkage effects on Integral Abutment Bridges (Publication No.3119993) [Doctoral dissertation, Florida Atlantic University]. ProQuest Dissertations Publishing.

Nebraska Department of Roads (2016). *Bridge Office Policies and Procedures*, Nebraska Department of Roads Bridge Division: Lincoln, NE, USA.

New Hampshire Department of Transportation (2015). *Bridge Design Manual*, Highway Division, New Hampshire Department of Transportation: Concord, NH, USA.

New Mexico Department of Transportation (2018). *Bridge Procedures and Design Guide*, Highway Division, New Mexico Department of Transportation: Santa Fe, NM, USA.

New Zealand Transport Agency (2013). *Bridge Manual*, 3rd ed, SP/M/022. New Zealand Transport Agency: Wellington, New Zealand.

Ooi, P.S.K., Lin, X., Hamada, H.S., (2010). Field Behavior of an Integral Abutment Bridge Supported on Drilled Shafts. *Journal of Bridge Engineering*, 15(1), 4-18. https://doi.org/10.1061/(ASCE)BE.1943-5592.0000036

Ooi, P.S.K., Lin, X., Hamada, H.S., (2010). Numerical Study of an Integral Abutment Bridge Supported on Drilled Shafts. *Journal of Bridge Engineering*, 15(1), 19-31. https://doi.org/10.1061/(ASCE)BE.1943-5592.0000037

Oregon Department of Transportation (2020). *Bridge Design Manual*, Highway Division, Oregon Department of Transportation: Salem, OR, USA.

Pennsylvania Department of Transportation (2019). *Design Manual*, Highway Division, Pennsylvania Department of Transportation: Harrisburg, PA, USA.

PLAXIS 2D manuals (2018).

PLAXIS 3D manuals (2018).

Potts, D. M., and Zdravkovic, L., (2001). *Finite element analysis in geotechnical engineering. Application*, Thomas Telford, London.

Quinn, B.H. and Civjan, S.A., (2017). Parametric Study on Effects of Pile Orientation in Integral Abutment Bridges. *Journal of Bridge Engineering*, 22(4). https://doi.org/10.1061/(ASCE)BE.1943-5592.0000952

Roads and Traffic Authority (2007). *Policy Circular BPC 2007/05*, Design of Integral Bridges: Sydney, Australia.

Rodriguez, L.E., Barr, P.J., Halling, M.W., (2014). Temperature Effects on a Box-Girder Integral-Abutment Bridge. *Journal of Performance of Constructed Facilities*, 28(3), 583-591. https://doi.org/10.1061/(ASCE)CF.1943-5509.0000437

Schanz, T., P. A. Vermeer, and P. G. Bonnier. 1999. The hardening soil model: Formulation and verification. *In Beyond 2000 in computational geotechnics: 10 years of Plaxis*, 281–296. Rotterdam, Netherlands: A.A. Balkema.

Sluis, J., Besseling, F., Stuurwold, P., Lengkeek, A., (2014). *Validation and Application of the Embedded Pile Row Feature in PLAXIS 2D*. Witteveen+Bos, The Netherlands

South Carolina Department of Transportation (2006). *Bridge Design Manual*, Highway Division, South Carolina Department of Transportation: Columbia, CS, USA.

Sigdel, L.D., Al-Qarawi, A., Leo, C.J., Liyanapathirana, S., Hu, P., (2021). Geotechnical Design Practices and Soil–Structure Interaction Effects of an Integral Bridge System: A Review. *Applied Sciences*, 11(15), 7131. https://doi.org/10.3390/app11157131

Soltani, A.A. and Kukreti, A.R., (1992). Performance evaluation of integral abutment bridges. *Transportation Research Record 1371*.

State of North Carolina Department of Transportation (2007). *Design Manual*, Highway Division, State of North Carolina Department of Transportation: Raleigh, NC, USA.

Tabatabai, H., Magbool, H., Bahumdain, A., Fu, C., (2017). Criteria and Practices of Various States for the Design of Jointless and Integral Abutment Bridges. *Proceedings of the 3rd international workshop on Jointless Bridges Conference.* Seattle, USA.

Tabrizi, A., Clarke-Sather, A., Schumacher, T., Healy, R., (2016). Bridge Retrofit or Replacement Decisions: Tools to Assess Sustainability and Aid Decision-Making. (No. CAIT-UTC-NC5), University of Delaware. Newark, Delaware.

Texas Department of Transportation (2020). *Bridge Design Manual-LRFD*, Highway Division, Texas Department of Transportation: Austin, TX, USA.

Vermont Department of Transportation (2019). *VTrans Structures Design Manual*, 5th ed, Highway Division, Vermont Department of Transportation: Montpelier, VT, USA.

Wahls, H.E. (1990). Design and Construction of Bridge Approaches. *National Cooperative Highway Research Program Synthesis of Highway Practice 159*, Transportation Research Board, National Research Council, Washington, D.C.

Walkinshaw, J.L. (1978). Survey of Bridge Movements in the Western United States. *Transportation Research Record 678*, Transportation Research Board, Washington, D.C.

West Virginia Department of Transportation (2004). *Bridge Design Manual*, Highway Division, West Virginia Department of Transportation: Charleston, WV, USA.

Weyers, R.E., Cady, P.D., Hunter, J.M., (1988). Cost-Effective Bridge Maintenance and Rehabilitation Procedures. *Transportation Research Record 1184*, Transportation Research Board, Washington, D.C.

White II, H., Pétursson, H., Collin, P., (2010). Integral Abutment Bridges: The European Way. *Practice Periodical on Structural Design and Construction*, 15(3), 201-208. https://doi.org/10.1061/(ASCE)SC.1943-5576.0000053

Wisconsin Department of Transportation (2021). *Bridge Manual*, Highway Division, Wisconsin Department of Transportation: Madison, WI, USA.

Wyoming Department of Transportation (2013). *Bridge Design Manual*, Highway Division, Wyoming Department of Transportation: Cheyenne, WY, USA.

Yang, P.S., Wolde-Tinsae, A.M., Greimann, L.F., (1985). Effects of Predrilling and Layered Soils on Piles. *Journal of Geotechnical Engineering*, 111(1), 18-31. https://doi.org/10.1061/(ASCE)0733-9410(1985)111:1(18)

Yokel, F.Y. (1990). Proposed Design Criteria for Shallow Bridge Foundations. National Institute of Standards and Technology Report No. NISTIR 90-4248, 50pp.

Zakhem, A.M. and El Naggar, H., (2019) Effect of the constitutive material model employed on predictions of the behaviour of earth balance (EFB) shield-driven tunnels. *Transportation Geotechnics*, 21. https://doi.org/10.1016/j.trgeo.2019.100264

Zhao, J.J. and Tonias, D.E., (2014). Bridge Engineering: Design, Rehabilitation and Maintenance of Modern Highway Bridges. 2nd ed. Lulu Press, Inc., Morrisville, NC.